The Pennsylvania State University
The Graduate School
College of Engineering

FIELD-ASSISTED SINTERING OF NICKEL-BASED SUPERALLOY POWDER FOR HIGH TEMPERATURE HYBRID TURBINE DISK APPLICATIONS

A Thesis in
Aerospace Engineering
by
Charis I. Lin

Submitted in Partial Fulfillment
of the Requirements
for the Degree of

Master of Science

December 2018

The thesis of Charis I. Lin was reviewed and approved* by the following:

Namiko Yamamoto
Professor of Aerospace Engineering
Thesis Co-Advisor

Jogender Singh
Professor of Materials Science and Engineering
Thesis Co-Advisor

Anil Kulkarni
Professor of Mechanical Engineering

Amy R. Pritchett
Professor of Aerospace Engineering
Department Head of Aerospace Engineering

*Signatures are on file in the Graduate School.

Abstract

Turbine disks of aerospace engines are made of nickel-based superalloys, the only materials that can withstand the extreme operating conditions with their high strength and creep resistance at high temperatures. To optimize performance and robustness, advanced turbine disks consist of hybrid or dual-microstructures: the outer section of the disk, including the blades, is typically single-crystalline to withstand high temperatures up to 1400°C while the inner section of the disk is typically polycrystalline to withstand high shear loadings from the ~10,000 rpm rotation. However, one-step fabrication of such disks with enough of a microstructure gradient is difficult to achieve. Joining two (or more) parts with different microstructures has been attempted using mechanical fir-tree connectors or using friction welding but results in a heavy joint weight or weak bonding due to localized melting from welding. Here, this thesis studies the effectiveness and evaluates the potential of field assisted sintering technology (FAST) as a novel, weight-saving method to join turbine disk components with different microstructures and to provide strong bonding interfaces, without altering the performance of original parts.

First, the capability of FAST was experimentally studied and confirmed for sintering of pre-alloyed Ni-based superalloy CM247LC powder into disks of scalable size (up to 200 mm). An increase in sintering temperature led to porosity migration away from the core of the sintered disks. After processing parameter optimization, the sintered material resulted in high relative density (>99%) and mechanical properties. To potentially improve melting temperature and mechanical properties of the sintered product, sintering of CM247LC powder with HfC additives, rarely studied in the past, was also conducted. HfC additives were expected to improve the performance of CM247LC disks due to grain growth inhibition and the higher melting temperature of HfC, but room-temperature performance improvement was found to be marginal, mostly due to poor diffusion of HfC into CM247LC grains. Because of the lack of performance improvement, HfC additions were not included during the manufacturing of hybrid disks using FAST.

Second, FAST joining of hybrid disks, consisting of a powder-sintered CM247LC rim and a solid Inconel 718 core, was demonstrated, achieving an interface strength comparable with the solid core component without the formation of a heat affected zone. A new FAST die set-up was designed to provide uniform stress distribution when powders for the rim section are sintered (and thus compacted) and joined to the core section simultaneously. Characterization of the hybrid disk interface and the parent materials was performed via optical microscopy, scanning electron microscopy, ultrasonic sound velocity measurements, and room-temperature tensile testing. The CM247LC powder-sintered rim, without HfC additives, exhibited mechanical properties that are comparable with parent material (monolithic CM247LC disks). Meanwhile, the FAST-processed Inconel 718 core disks exhibited lower mechanical strengths than those of as-received reference Inconel 718 disks. The core-rim interfaces were observed to be oxidized, but homogeneous and free of defects and porosity, unlike the interfaces heat-affected by friction welding in past studies. Despite the high interface strength, a combination of interface effects and the effect of the weaker Inconel 718 material led to tensile fracture near the material interface, so further optimization of processing parameters is needed to improve interface bonding.

This work may be a starting point for the joining of dissimilar nickel-based superalloys in turbine disk and blade assemblies using FAST. Future research can modify FAST sintering parameters to minimize weakening of solid cores and improve the rim-core interfaces. Current studies are limited to joining of two polycrystalline parts, but by joining polycrystalline and single-crystalline parts, interface formation is expected to be more complex due to the set crystalline orientation. In addition to improvement of hybrid disk components and interfaces, characterization of fabricated hybrid disks at high operating temperatures is needed.

Table of Contents

List of Figures **viii**

List of Tables **xiii**

List of Symbols **xiv**

Acknowledgments **xvi**

Chapter 1
Introduction **1**

Chapter 2
Background **5**
2.1 Current Single-Microstructure Turbine Disk Fabrication 5
2.2 Previous Work on Forming Dual Microstructure Turbine Disks . . . 6
2.2.1 Fir-tree Joining 7
2.2.2 Dual Microstructure By Heat Treatment 7
2.2.3 Friction Welding 9
2.2.4 Field Assisted Sintering Technology 10
2.2.5 Previous Work on Joining Using FAST 11
2.2.6 Previous Work on Sintering Nickel-Based Superalloys Using FAST 12
2.3 Grain Growth Inhibitors in Tungsten Alloys 13
2.3.1 Previous Studies 13
2.3.2 Mechanism of Grain Growth Inhibition 14
2.4 Previous Work on Hafnium Additions to Nickel-Based Superalloys . 15

Chapter 3
Objectives and Approach **16**
3.1 Objectives 16

3.2 Approach 17

Chapter 4

Materials and Methods 19

4.1 Materials 19

4.2 Methods 21

  4.2.1 FAST Sintering Process 21

  4.2.2 Sintering of 40- and 80-mm-diameter CM247LC disks 24

  4.2.3 Addition of Hafnium Carbide Particles 24

  4.2.4 Manufacturing Hybrid Disks 26

4.3 Analysis Methods 27

  4.3.1 Microstructural Inspection 27

  4.3.2 Mechanical and Thermal Characterization 28

Chapter 5

Sintered CM247LC Disks 30

5.1 Sintering CM247LC Powder to High Density 30

  5.1.1 Temperature and Pressure for High Density 30

  5.1.2 Scalability Study 30

5.2 Microstructural Inspection 33

  5.2.1 Optical Microscopy 33

  5.2.2 Phase Formation 34

5.3 Mechanical Characterization 36

  5.3.1 Elastic Modulus 36

  5.3.2 Hardness 37

Chapter 6

CM247LC Powder Sintered with Hafnium Carbide Additives 40

6.1 Microstructural Inspection 40

  6.1.1 Effect of HfC additions on Porosity 40

  6.1.2 Interface between HfC and CM247LC 41

6.2 Mechanical Characterization and Thermal Properties 41

  6.2.1 Elastic Modulus and Hardness 41

  6.2.2 Tensile Testing 43

  6.2.3 Melting Temperature 45

Chapter 7

Hybrid Turbine Disks Using FAST 48

7.1 Porosity and Defects 48

7.2 Elastic Modulus and Hardness 50

7.3 Tensile Testing 52
7.4 Scaled-up Manufacturing of Hybrid Disks 57

Chapter 8
Summary and Future Work **61**
8.1 Summary and Conclusions 61
8.2 Future Work 63

Appendix A
Elastic Modulus and Hardness **65**
A.1 Introduction 65
A.2 Study of Relationship using Vicker's Indentation 65

Appendix B
Silicon Carbide Nanoparticle Additions to Inconel 625 **67**
B.1 Introduction 67
B.2 Materials and Sintering Process 67
B.3 Resulting Microstructure 70
B.4 Resulting Mechanical Properties 71
B.5 Summary and Discussion 73

Bibliography **76**

List of Figures

1.1 Targeted properties of a hybrid turbine disk with hafnium or hafnium carbide additions in the rim. 3

2.1 Fir-tree joining of turbine blade and disk, based on [1] and [2]. . . . 7

2.2 FAST sintering mechanism. 11

4.1 SEM micrographs of CM247LC powder (left) and hafnium carbide powder (right). 20

4.2 X-ray diffraction spectrums of (a) CM247LC powder and (b) HfC powder. 21

4.3 FAST units at Penn State. (a) Fast unit with maximum 25 metric ton pressing force, (b) FAST unit with maximum 250 ton pressing force, and (c) FAST unit with maximum 325 ton pressing force. . . 22

4.4 Plot of sintering parameters for an 80 mm diameter CM247LC disk. This disk was sintered first at 45 MPa and 1260°C for 5 minutes, then at 25 MPa and 1300°C for 5 minutes before cooling. 23

4.5 Assembly of graphite or CFRC die, machined inner disk, and powder rim for manufacturing of hybrid disk, before sintering and after sintering. 27

4.6 Subscale tensile specimen dimensions for tensile testing. 29

5.1 Optical micrographs of sintered CM247LC before etching. Cross-sections taken near the edges of the sintered disks with various sintering parameters and disk sizes. Samples sintered at 1225°C. Relatives densities are (a) 98.8%, (b) 99.6%, (c) 97.8%, and (d) 98.3% 31

5.2 Possible variation of axial force with radius. Hypothesized migration of pores and defects with increasing sintering temperature is shown. 32

5.3 Optical micrographs of the edge of sintered CM247LC samples, sintered at 45 MPa for 15 minutes at various temperatures. The samples were sintered at (a) 1225°C, (b) 1240°C, (c) 1250°C, and (d) 1260°C. 33

5.4 Comparison of amount of flashing seen in sintered CM247LC disks. (a) CM247LC powder sintered at 45 MPa and 1260°C for 15 minutes. (b) CM247LC powder sintered first at 45 MPa and 1260°C for 10 minutes followed by 25 MPa and 1275°C for 5 minutes. 34

5.5 Optical micrographs of the edge of sintered CM247LC samples, sintered at 45 MPa for 15 minutes at various temperatures and pressures. The samples were sintered at (a) 1225°C for 15 minutes at 45 MPa, (b) 1260°C for 10 minutes at 45 MPa followed by 1275°C for 5 minutes at 25 MPa, (c) 1260°C for 5 minutes at 45 MPa followed by 1300°C for 5 minutes at 25 MPa, and (d) 1260°C for 5 minutes at 45 MPa followed by 1300°C for 5 minutes at 35 MPa. . . 35

5.6 Optical micrographs of sintered CM247LC samples, sintered at 45 MPa for 15 minutes at various temperatures. Waterless Kalling's Etch. The samples were sintered at (a) 1225°C, (b) 1240°C, (c) 1250°C, and (d) 1260°C. 36

5.7 Optical micrographs of sintered CM247LC samples, sintered at 45 MPa for 15 minutes at various temperatures and pressures. Waterless Kalling's Etch. The samples were sintered at (a) 1225°C for 15 minutes at 45 MPa, (b) 1260°C for 10 minutes at 45 MPa followed by 1275°C for 5 minutes at 25 MPa, (c) 1260°C for 5 minutes at 45 MPa followed by 1300°C for 5 minutes at 25 MPa, and (d) 1260°C for 5 minutes at 45 MPa followed by 1300°C for 5 minutes at 35 MPa. 37

5.8 XRD spectrum of both sintered and unsintered CM247LC powder. The sintered CM247LC sample had diameter 80 mm and thickness 3 mm, sintered at 35 MPa and 1225°C for 15 minutes. 38

5.9 Elastic modulus of sintered 80 mm CM247LC disks at different sintering parameters. Samples with a single hold step were sintered for 15 minutes. 39

5.10 Vicker's hardness of sintered CM247LC samples vs. sintering parameters. Samples with a single hold step were sintered for 15 minutes. Measurements were taken near the edge of the sintered samples. . . 39

6.1 Optical and SEM micrographs of sintered CM247LC powder with 5 vol.% HfC additions, sintered at 45 MPa and 1225°C for 15 minutes. 41

6.2 Left: scanning transmission electron micrograph of embedded HfC particles in a sintered sample. The sample composition was CM247LC + 3 vol.% HfC, sintered at 45 MPa and 1225°C for 15 minutes. Right: energy-dispersive X-ray spectroscopy image showing the composition at the interface between the HfC particle and Ni-superalloy matrix. 42

6.3 EDS Line Scan across interface between HfC particle and CM247LC matrix. Location of the line scan is seen in Figure 6.2. 42

6.4 Mechanical properties of sintered CM247LC disk with HfC additions. Samples were sintered at 45 MPa for 15 minutes. (a) Elastic modulus vs. composition. (b) Vicker's hardness vs. composition. 43

6.5 Tensile specimens of CM247LC with 0 and 3 vol.% HfC after tensile testing. 44

6.6 Optical micrographs of broken tensile samples, cut from samples sintered at 1250°C and 45 MPa for 15 minutes. Materials are (a) CM247LC and (b) CM247LC with 3 vol.% HfC. 45

6.7 SEM micrographs of tensile fracture surfaces. Tensile specimens were cut from sintered CM247LC powder with and without HfC additions, sintered at 1250°C and 45 MPa for 15 minutes. 46

6.8 Melting temperature of sintered CM247LC with various amounts of HfC. 47

7.1 Joined subscale hybrid disks of two different joining angles, ground down on both sides after joining using FAST. 49

7.2 X-ray topography image of subscale hybrid disks. Left: hybrid disk with a 0 dgree joining angle. Right: hybrid disk with a 45 degree joining angle. 49

7.3 Optical micrographs of joined subscale hybrid disks. (a) Disk with 0° interface, joined at 45 MPa and 1225°C for 20 minutes. (b) Disk with 45° interface, joined at 45 MPa and 1225°C for 15 minutes. . . 50

7.4 Elastic modulus of subscale hybrid disks sintered at 45 MPa and 1225°C. 51

7.5 Vicker's hardness values of hybrid disks. Left: hardness values of hybrid disk with 0 degree interface. Disk joined at 45 MPa and 1225°C for 20 minutes. Right: hardness values of hybrid disk with 45 degree interface. Disk joined at 45 MPa and 1225°C for 15 minutes. 52

7.6 Tensile specimens after tensile testing. 54

7.7 Optical micrographs of broken tensile samples, cut from Inconel 718 plate. Materials are (a) as-received and (b) FAST-heat-treated at 1225°C and 45 MPa for 15 minutes. 55

7.8 SEM images of fracture surfaces of forged Inconel 718 material (as-received and FAST-heat-treated) and hybrid disks (0° and 45° interface). 58

7.9 Optical micrographs of broken tensile samples, cut from a hybrid disk with a 45° interface. Three separate tensile samples were polished to illustrate three different cross-sections. 59

7.10 Optical micrographs of a broken tensile specimen, cut from a hybrid disk with a 0° interface. 60

7.11 Hybrid disk of 200 mm, joined at 1275°C for 30 minutes. 60

A.1 Elastic Modulus vs. Vicker's Hardness of various materials sintered using FAST, as measured at Penn State Applied Research Laboratory. 66

B.1 SEM micrographs of Inconel 625 powder (left) and silicon carbide powder (right). 68

B.2 SEM micrographs of Inconel 625 silicon carbide powder mixtures before sintering. 69

B.3 Temperature and ram movement during the sintering of pure SiC powder. 69

B.4 Powder-sintered Inconel 625 plates with SiC additions. 70

B.5 Optical micrographs of sintered Inconel 625 plates with SiC additions showing grain size. 71

B.6 Optical micrographs of sintered Inconel 625 plates with SiC additions. 72

B.7 X-ray diffraction spectrums of forged, powder, and sintered Inconel 625. 73

B.8 Scanning transmission electron micograph of grain boundary of sintered Inconel 625 with 5 vol.% SiC additions. 74

B.9 Vicker's hardness of Inconel 625 with various amounts of SiC additions. 74

B.10 Elastic modulus of Inconel 625 with various amounts of SiC additions. 75

List of Tables

1.1 Strength and Service Temperature of Various Materials 2

4.1 Nominal Composition of CM247LC [3] 20

4.2 40 mm Diameter Disks: Sintered CM247LC Powder 24

4.3 80 mm Diameter Disks: Sintered CM247LC Powder 25

4.4 40 and 80 mm Diameter Disks: Sintered CM247LC with HfC Additions 25

4.5 70 mm Diameter Disks: Hybrid Disks with Solid Inconel 718 Core and Powder-Sintered CM247LC Rim 26

6.1 Tensile Properties of CM247LC With And Without HfC 44

7.1 Tensile Properties of Hybrid Disks and Parent Materials 53

B.1 Composition of Inconel 625 68

List of Symbols

CFRC	Carbon fiber reinforced carbon
d	Diameter
E	Elastic Modulus
EDS	Electron dispersive spectroscopy
FAST	Field assisted sintering technology
FCC	Face centered cubic
FIB	Focused ion beam
γ	Continuous matrix
γ'	Primary strengthening phase
h_1	Initial powder height
h_2	Final sintered powder height
HIP	Hot isostatic pressing
HV	Vicker's hardness value
LSHR	Low solvus high refractory
ν	Poisson's ratio
P	Pressure
ρ	Density

rpm	Rotations per minute
SPS	Spark plasma sintering
t	Sintering time
T	Temperature
τ	Time of ultrasonic pulse
$th.$	Sample thickness
θ	Angle of incidence
UTS	Ultimate Tensile Strength
V	Sound velocity
V_L	Longitudinal velocity
V_T	Transverse velocity
vol.%	Volume percent
wt.%	Weight percent
XRD	X-ray diffraction
YS	Yield strength

Acknowledgments

This research was partially funded by the Government under Agreement No. W911W6-17-2-0003. The U.S. Government is authorized to reproduce and distribute reprints for Government purposes notwithstanding any copyright notation thereon.

The views and conclusions contained in this document are those of the authors and should not be interpreted as representing the official policies, either expressed or implied, of the Aviation Development Directorate or the U.S Government.

This research was also partially funded by the Penn State Applied Research Laboratory.

I would like to thank the technicians and engineers at ARL who have helped me tremendously throughout this project. I would also like to thank my fellow research students and their support, with special thanks to Sebastian Niuman for his help with imaging and polishing work.

Finally, I would like to thank Dr. Jogender Singh and Dr. Namiko Yamamoto for their ongoing support and encouragement. Thank you for this opportunity to complete my Master's studies and for energetically guiding me through my research. Thank you for investing time into me and my work and for always being willing to answer questions. You are both amazing mentors and professors, and I am honored to be able to continue working with you.

Chapter 1
Introduction

Effective hybridization of the turbine disk in gas turbine engines improves lifecycle costs by allowing for enhanced thrust-to-weight ratios and thermal stabilities in the extreme high temperature environment. Currently, a heavy mechanical joint connects single crystal turbine blades to a polycrystalline disk. Hybridization, or joining components directly without a mechanical joint, would result in a significant weight reduction. Weight-savings in the turbine disk would significantly affect the overall efficiency of the engine, as turbine disks account for about 20% of the total weight of a typical civil turbofan and about 5% for military applications [4]. Because solid-state joining may join components with dissimilar material properties without the weight penalty of a heavy mechanical joint, recent studies have explored solid-state joining of turbine disk and blade materials. In this thesis, field assisted sintering technique (FAST) is used to manufacture hybrid turbine disks via solid-state joining because of FAST's versatility, fast sintering times, and joining capabilities.

Optimizing material properties in turbine blade and disk assemblies is crucial because the components undergo high thermal and mechanical stresses. The outer rim of turbine disks for gas turbine engines can approach a temperature of 760°C or even 815°C for military applications while the turbine blades contact a gas stream with temperatures above 1400°C. The portion of the disk around the shaft, the core, reaches temperatures lower than the rim or the blades, typically less than 600°C. The core also experiences high stresses from the shaft, as blades and disks rotate at over 10,000 revolutions per minute [4, 5]. Therefore, turbine blade and disk assembly components require dissimilar properties because of the different strength and temperature requirements; turbine blades and the outer rim of turbine disks require higher thermal stability and higher creep resistance while turbine

Table 1.1. Strength and Service Temperature of Various Materials

Material	Strength [MPa]	Max. Service Temperature [°C]
Al alloys	30-400	120-200
Carbon Fiber Reinforced Plastics	400-900	140-210
Carbon Steels	400-1000	170-300
Ti alloys	300-1000	300-700
Stainless Steels	200-900	260-820
Ni alloys	70-1000	240-1100
Ceramics	20-1000	90-1900

disks, especially near the core, require higher toughness and fatigue resistance.

To achieve high thermal and mechanical properties, turbine blades and disks currently are formed from nickel (Ni)-based superalloys. These materials display high strength and creep resistance at high temperatures, with temperature capabilities up to 1100°C, as shown in Table 1.1 [6]. Ni-based superalloys are one of the only materials able to withstand the high temperature turbine environment; although ceramics have high strength and thermal properties, their brittleness make them unfit for use in the turbine blade and disk assembly. Currently, turbine disks consist of polycrystalline alloys while the turbine blades consist of single crystal components. Polycrystalline alloys allow for higher strength and toughness while single crystal alloys eliminate grain boundaries and allow for excellent creep resistant properties. Therefore, by optimizing microstructure within the assembly, strength and thermal stability can be modulated.

The current difficulty in optimizing microstructure is joining dissimilar Ni-based superalloys without a weak interface while maximizing weight savings. A successful joining method is needed to produce a hybrid disk, where the rim and the core of the disk have different mechanical properties which can be tailored to meet the different lifecycle requirements for the different portions of the disk, as seen in Figure 1.1. The current state-of-the-art technology to join Ni-based superalloy disks is friction welding, but the friction weld leads to plastic deformation at the interface and localized melting, resulting in high residual stresses and a loss of hardness. FAST, also known as spark plasma sintering (SPS), is a powerful sintering method that has the potential to manufacture hybrid disks because of its versatility and joining potential. FAST can sinter a wide variety of materials, including metals, refractory metals, intermetallics, and ultra-high-temperature ceramics [7], though there have

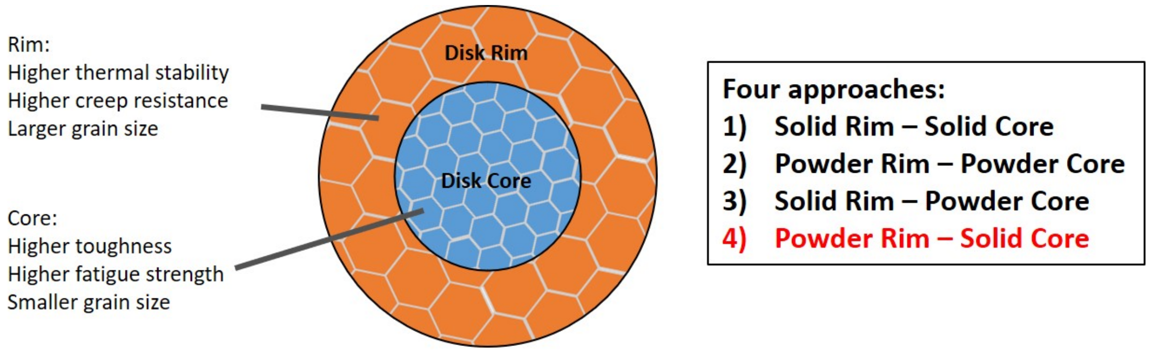

Figure 1.1. Targeted properties of a hybrid turbine disk with hafnium or hafnium carbide additions in the rim.

been few studies regarding the sintering of Ni-based superalloys via FAST. In previous studies, FAST has joined dissimilar materials through functional grading or solid state joining, resulting in interfaces free of localized melting. The idea of using FAST to join turbine blade and disk materials is not new; a patent by Seth et al. described the repairing of turbine engine components using FAST/SPS [8]. By applying contact pressure between two surfaces, optionally placing fine particles between the surfaces for better bonding, then applying an electrical field, FAST could potentially rapidly repair and manufacture turbine engine components. However, the joining process has not been successfully demonstrated. Before taking advantage of FAST for hybrid disk applications, more research is needed to understand the processing-structure-property relationships during the joining of dissimilar Ni-based superalloys using FAST. FAST can perform solid state joining between solid components that were previously sintered or cast and wrought, powders, or a combination of the two. As a result, hybrid disks formed using FAST may be formed from solid components, powder components, or a mixture of the two. Thus, four approaches exist to join dissimilar Ni-based superalloys in a hybrid disk: joining a machined solid core to a solid rim, a solid core to a rim sintered from powder, a powder core to a solid rim, and simultaneously sintering a powder core and a powder rim. This thesis focuses on developing a process for joining a solid fored core to a powder rim using FAST.

The goal of this thesis is to gain knowledge about the hybridization of the turbine disk using FAST, which has cost-saving potential because of its short sintering times and its potential to replace the hot isostatic pressing or extrusion seen in conventional powder metallurgy. This work examines the effect of FAST parameters on the microstructure and mechanical properties of sintered CM247LC powder, then studies the resulting characteristics of hybrid disks joined using FAST. Microscopy, microindentation, and tensile testing are the main analysis tools. Background information and previous studies related to this thesis will be presented in Chapter 2, and the objectives and approach of this thesis will be discussed in Chapter 3. Chapter 4 then presents the materials used in the studies as well as the methods of sintering and joining the materials. Chapters 5, 6, and 7 discuss the results of FAST-sintering CM247LC powder, FAST-sintering CM247LC with hafnium carbide additions, and joining hybrid turbine disks, respectively. The discussion of results is followed by summary and future work in Chapter 8.

Chapter 2 Background

In this chapter, current turbine disk manufacturing and efforts to produce hybrid disks will first be discussed. Second, an overview of FAST sintering will be given, followed by a discussion of grain growth inhibitors in tungsten alloys sintered using FAST. Finally, the effect of hafnium (Hf) additions on the mechanical and thermal properties of Ni-based superalloys will be discussed.

2.1 Current Single-Microstructure Turbine Disk Fabrication

Turbine disks for gas turbine engines were initially formed using the cast-and-wrought method, an efficient and well-developed process with low cost processing [9]. In the conventional cast-and-wrought method, ingots are first produced by vacuum induction melting, electro-slag refining and vacuum arc remelting. The material is then annealed for homogeneity, thermal-mechanically worked, and finally forged [4]. This method cannot be applied to many modern Ni-based superalloys with the γ' phase and high volume fractions of refractory elements, as the cast-and-wrought materials would show macroscopic solidification defects [5,9]; segregation of alloying elements during melt processing and by the flow stress at the process temperatures would cause cracking during the thermal-mechanical working process [4].

Today, powder metallurgy is the leading method for producing single-microstructure high-temperature turbine engine components due to the improved temperature capabilities [5]. During the production of Ni-based superalloys via powder metallurgy, vacuum induction melting forms highly alloyed ingots, which are then atomized to produce a pre-alloyed powder. After the powder is sieved to remove large non-metallic agglomerates, hot isostatic pressing (HIP) or hot extrusion consolidates the powder without further melting [10,11]. After powder consolidation, isothermal forging shapes the consolidated material into the desired form. The consolidated powder is then heat-treated, with material properties controlled by the various heat processing parameters [10].

Although powder metallurgy allows for an increase in turbine component temperature capabilities, the current powder consolidation method leads to a variety of defects, as seen in a study of the Ni-based superalloy Rene 95 by Chang et al. [12]. Contamination from the melting crucible, pouring tundish or atomizing nozzle during the powder formation process results in defects in the form of ceramic inclusions, whichs can appear as both discrete particles and particle agglomerates [4]. Powder particle defects also arise due to contamination during the HIP process, where fine oxide or carbide particles agglomerate at the powder surfaces; these defects occur less frequently than ceramic inclusions. A third form of defects, voids, may also appear in HIP superalloys due to trapped argon from argon atomization for powder production. Voids may cause premature failure in the superalloy material [12].

Current powder metallurgy and the outmoded cast-and-wrought method also limit composition and microstructure. Both methods use a single stoichiometric composition throughout the disk, so the composition of different disk areas cannot be tailored to meet the required mechanical and thermal properties. Also, heat treatments are performed on the entire disk as a whole, leading to generally continuous properties throughout the disk. These limitations can be overcome through dual microstructure or hybrid turbine disks, where heat treatments lead to a bimodal microstructure or different materials are joined in the disk, as discussed in the following section.

2.2 Previous Work on Forming Dual Microstructure Turbine Disks

Dual microstructure or hybrid turbine disks can satisfy mechanical and thermal requirements more effectively than single microstructure disks. During service, the rim of the turbine disk reaches higher temperatures and faster speeds than the core

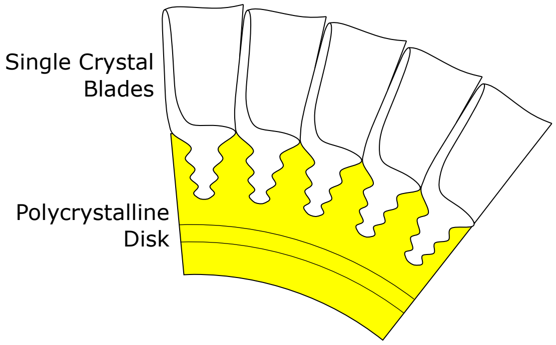

Figure 2.1. Fir-tree joining of turbine blade and disk, based on [1] and [2].

while the core undergoes greater shear stresses than the rim. A dual microstructure turbine disk would therefore allow for dedicated materials with suitable properties to maximize effectiveness [4]. However, modern Ni-based superalloys are difficult to join and are unweldable by conventional fusion processes because of their highly alloyed composition; during conventional welding, impurity and alloying elements segregate from the main material and coalesce, which leads to weld solidification cracking, metal liquation cracking, and a heat affected zone at the welding surfaces [13, 14]. In this section, previous studies on manufacturing dual microstructure disks are discussed.

2.2.1 Fir-tree Joining

In current gas turbine engines, a mechanical fir-tree slot joins turbine disks, as seen in Figure 2.1. After precise machining of the mechanical joint to distribute the centrifugal loads evenly, the single-crystal blades can be joined to the polycrystalline disks with excellent load transmission [1]. However, replacing the fir-tree joint with a direct joining method would lead to weight savings of approximately 30% [2]. Consequently, joining different materials within the blade-disk assembly via a mechanical joint would be heavier than joining the materials directly, so a method of forming hybrid disks is desired.

2.2.2 Dual Microstructure By Heat Treatment

Hybrid turbine disks require a greater creep resistance at the rim and greater strength and fatigue resistance at the core, which reflects a larger grain size at the rim and a smaller grain size at the core. Dual microstructure disks with varied grain sizes was achieved in cast-and-wrought turbine disks using inhomogenous heat treatments [15–21]. The dual microstructure was formed by heating the rim of the disk over the γ' solvus temperature while keeping the core under the solvus temperature.

Three methods have been used to perform a dual microstructure heat treatment on turbine disks. The first method of heat treatment uses induction heating to heat the rim of the disk more quickly than the core [15]. A second approach uses steel heat sinks to conduct heat away from the top and bottom of the disk core during the heating process [16,19,22]. A third approach was studied by GE Aircraft Engines, in which a cooling air fixture controls the temperature gradient, resulting in a gradient grain size varying from 5 µm at the core to 40 µm at the rim [18]. Ning et al. used a similar process to produce a gradient variation in grain size, using water to cool the core of the disk rather than air; the resulting grain sizes were similar to that of the air cooling method, with a variation of 4 µm at the core to 40 µm at the rim [20]. Tensile testing, creep testing and burst testing showed that dual microstructure disks resulted in creep resistant rims as well as high strength, fatigue resistant cores [16].

The limitation of dual structured turbine disks formed using these methods is the constant stoichiometric composition throughout the disk. Heat treatments must be carefully chosen to bring out the desired microstructures in the different parts of the disk, and researchers have been successful in forming a gradient of grain sizes and γ', but the capabilities of the base material limit the changes in microstructure. Thus, in order to form higher-performance turbine disks, a method to join alloys with microstructures tailored to satisfy the requirements of each section is preferred. Two early attempts at joining dissimilar Ni-based superalloys to form hybrid turbine disks are diffusion bonding [23] and a metallurgical butt type joint [24]. During solid state diffusion bonding, hot isostatic pressing bonds turbine blades to the disk, but the result of the bond is inconsistent. A metallurgical butt type joint mainly uses a mechanical joint to form a stress resistant hybrid turbine assembly.

2.2.3 Friction Welding

The current state-of-the-art technology for joining of turbine disks is friction welding, a solid-state joining method. During friction welding, one component is moved relative to another adjacent component in a linear or rotated manner, and the resulting heat from localized friction leads to a plasticized interface and localized melting. After the relative movement stops, the weld is consolidated by a forging force [25, 25].

A series of studies by Senkov et al. showed that friction welding Ni-based superalloy Mar-M247 and low solvus high refractory (LSHR) superalloy to form hybrid turbine disks resulted in inconsistencies near the weld interface, including a 4-5 mm heat affected zone and grain refinement near the weld [26–29]. Changes in microstructure occurred within the 4-5 mm heat affected zone, mostly at the weld interface. This result suggests a temperature gradient within the heat affected zone, which is often associated with localized melting. Near the weld interface, the grain size of the Mar-M247 alloy decreased to approximately 0.5 µm; before welding, the elongated Mar-M247 grains were 0.5 to 1.0 mm in width and 1 to 5 mm in length. The large decrease in grain size suggests large plastic deformation and dynamic recrystallization due to the friction welding process, which also suggests high residual stresses at the interface. The friction welding produced abrupt boundaries between the coarse grains and fine grain layer in the Mar-M247 alloy and between the Mar-M247 alloy and the LSHR alloy. A continuing study found that the smaller grain size near the interface was accompanied by a dissolution of the γ' phase near the interface [27]. Close to the interface, the size and volume fraction of the γ' particles decreased, and their morphology transitioned from a cuboidal shape to a more rounded shape. Improvements to the joining surface can be made through the changing of process variables; a higher welding temperature promoted deformation at the interface, and preheating one of the two materials before joining improved the weldability of the preheated material [28, 29].

In a similar study, Huang et al. characterized the joining of Ni-based superalloys 720Li and Inconel 718 using inertia friction welding [30]. The weld interface was free of micropores and microcracks, but large changes in grain structure and precipitation phase morphology were found near the interface. The decrease in hardness in the heat affected zone was shown to recover after a post weld heat treatment at 760°C, with hardness values near the weld 10 to 15% higher than the parent materials. However, immediately beside the weld line, hardness values decreased due to recrystallization of γ' grains. Also, the base material of Inconel 718 far from the weld showed hardness losses due to the post weld heat treatment.

Although microstructure optimization is possible through the application of friction welding to hybrid turbine disks parts, deformations and inconsistencies at the weld interface remain an issue due to the fundamental process of friction welding. Friction welding leads to localized melting at the interface, and deformations will occur because of the kinetic energy being transformed to frictional heat. A way to eliminate the heat affected zone has not been found, nor has there been found a way to eliminate the decrease in hardness near the friction welded area. Thus, a method to join dissimilar Ni-based superalloys without such deformations is desired.

2.2.4 Field Assisted Sintering Technology

Our proposed method of manufacturing hybrid turbine disks is to perform solid-state joining of dissimilar Ni-based superalloys using FAST with possible Hf or hafnium carbide (HfC) additions to improve material properties.

FAST is a sintering and synthesis technique which combines direct-current-driven temperature with pressure, leading to a high diffusion rate [7]. The FAST/SPS setup is made of a mechanical loading system along with an electrical circuit. As shown in Figure 2.2, the powder material is contained in a graphite die, and uniaxial pressure is applied via an upper and lower punch to assist densification [31]. Low voltages produce high currents ($\tilde{1}$-10 kA) through the die, punches, and powder material. The high current through the powder results in efficient volumetric Joule heating, while the current flowing through the die results in radiant heating [7, 31]. With heating rates as high as 1000°C/min and with the contribution of pressure, total processing time can be shortened (on the order of minutes) compared to conventional sintering processes (on the order of hours and days) [7]. The short processing time may minimize grain growth and therefore improve mechanical properties such as hardness, as demonstrated with tungsten alloys [32, 33]. The addition of small carbide particles may further inhibit grain growth as desired in the core of the turbine disk, as discussed in section 2.4.

FAST is associated with a high particle diffusion rate and short sintering times.

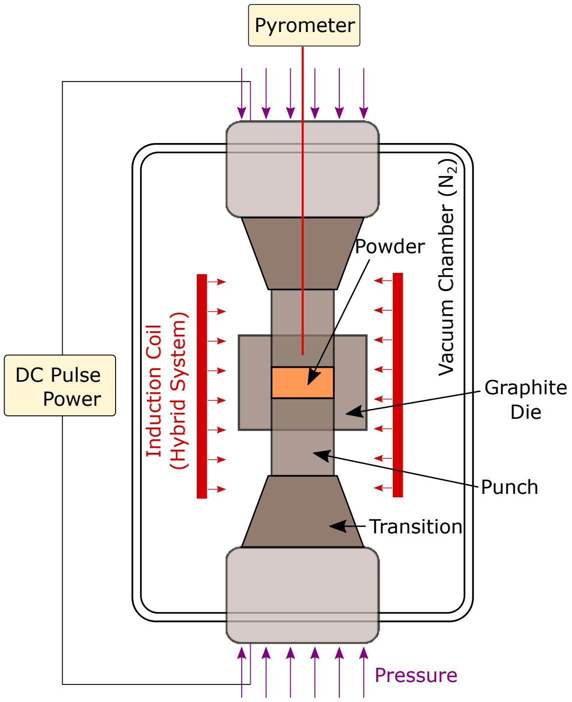

Figure 2.2. FAST sintering mechanism.

Lower sintering temperatures accompany the short sintering times because the FAST process promotes diffusion more easily than in conventional sintering processes; while FAST relies on current, the conventional hot press uses radiation heating and the application of uniaxial pressure to promote Joule heating and powder sintering [34]. The mechanism of FAST is not yet fully understood. However, it has been hypothesized that the pulse voltage used by FAST discharges between the powder particles, promoting diffusion between the particles, as the pulsed current leads to melting and rapid solidification at the particle interfaces [34, 35]. Because of the high current density at powder-contacting surfaces, the powder may quickly diffuse together with the addition of pressure during the FAST sintering process. With the rapid increase in surface contact area, temperature will decrease quickly, leading to rapid solidification and neck formation at the interface [35].

2.2.5 Previous Work on Joining Using FAST

FAST is able to join dissimilar materials, whether through functional grading or solid state joining. Materials joined via functional grading using FAST in previous studies include titanium nitride (TiN) and aluminum oxide (Al_2O_3), hydroxyapatite (HA) and yttria stabilized tetragonal zirconia, zirconium dioxide (ZrO_2) and stainless steel, nickel and copper, and zirconium diboride (ZrB_2) and zirconium dioxide (ZrO_2), among many others [7]. Unlike in hot pressing or hot isostatic pressing, FAST has the additional capability of producing functionally graded materials in one step by the use of asymmetric graphite dies and punches, as shown by Belmonte et al. in a study of SPS processes on Si_3N_4 [36]. The asymmetric die setup led to a decreasing temperature gradient from the top to the bottom of the material, and the resulting materials showed a gradation of grain size and α-phase content. Solid-state joining has also been shown to be possible using FAST, where solid and/or powder materials are placed together and go through the FAST process, resulting in a single joined part without melting of the materials. One example is the joining of tungsten to copper, materials with large melting point mismatch and immiscibility which prevents solid state diffusion [37]. Nickel powder, used as an intermediary layer, was first fused to tungsten, and the copper was then fused to the nickel at a lower temperature.

2.2.6 Previous Work on Sintering Nickel-Based Superalloys Using FAST

Few previous studies explored the sintering of Ni-based superalloys via FAST, but one study described the strengthening of a Ni-20Cr compound with Y_2O_3 and Al_2O_3 particles during FAST sintering for dispersion and composite strengthening, respectively. When the powder was sintered at 1100°C for five minutes, a 99% relative density was reached, with a higher sintering temperature resulting in a higher hardness and density [38]. In this study, all grain growth was inhibited through oxide additions during FAST sintering. Also, higher sintering temperature resulted in higher hardness and density in the Ni-20Cr compound, along with a higher volume fraction of twins.

In a preliminary study, as described in Appendix B, the Ni-based superalloy Inconel 625 was sintered using FAST, resulting in a high density (98.7%). The study showed FAST's ability to sinter a nickel-based superalloy to high density, though the resulting mechanical properties were lower than that of a reference forged Inconel 625 plate.

2.3 Grain Growth Inhibitors in Tungsten Alloys

This thesis investigates the addition of micro-HfC particles during the FAST sintering of the Ni-based superalloy CM247LC. Previous research has shown how carbides can act as grain growth inhibitors for tungsten alloys and as a result improve mechanical properties. Grain growth inhibitors are commonly used to manufacture fine-grained WC-Co alloys [39]. Common grain growth inhibitors include chromium carbide (Cr_3C_2), vanadium carbide (VC), niobium carbide (NbC), and tantalum carbide (TaC), with VC being the most effective. Studies on these additions to various WC-Co alloys show that with an optimum amount of carbide additions, the additions effectively reduce grain size [40–44].

2.3.1 Previous Studies

Studies have shown grain growth inhibitors to also be effective in conventional liquid phase sintering. Huang et al. showed that up to 0.9 wt.% of NbC limits WC grain growth in WC-Co hardmetals, resuting in improved hardness, toughness, and bend strength [40]. Similarly, a study by Wittmann, Schubert and Lux studied the effect of VC, Cr_3C_2, TaC, TiC, and ZrC on the grain growth of WC sintered with nickel and iron binders [44]. The study showed that VC is the most effective inhibitor in WC-Ni hardmetals, with 1 wt.% VC being the most effective amount.

Grain growth inhibitors are also effective in FAST sintering. In a study of NbC additions to WC-Co hardmetals sintered using FAST, up to 5 wt.% of NbC was effective in reducing grain size [40]. Similarly, Sun et al. showed that various amounts of VC and Cr_3C_2 additions to WC-Co cemented carbides sintered using FAST influenced grain size and mechanical properties [42]; the optimum amount of VC without Cr_3C_2 additions was less than 0.7 wt.%, and the optimum amount of Cr_3C_2 without VC additions was 0.6 wt.%. Above the optimum amount, grain growth inhibitors do not further inhibit grain growth because there is a limit to the solubility of the inhibitors in the Co binder as well as a limit to the reduction of WC particle surface energy via the dispersion of inhibitors. Increasing Cr_3C_2 additions also resulted in greater porosity [41]. The increased porosity may be because the carbide content saturated the liquid cobolt, and excess carbide precipitated at the grain boundaries, which affected the material densification. Poetsche et. al.

showed that VC and Cr_3C_2 are also effective in inhibiting grain growth in binderless tungsten carbide [43], sintered by both gas pressurized sintering and FAST sintering. Cr_3C_2 had the additional effect of suppressing abnormal grain growth.

Parameters other than grain growth inhibitors may also strongly influence grain growth. The study by Wittmann, Schubert and Lux showed that the gross carbon content strongly affected the grain growth in WC-Fe alloys, with a higher carbon content promoting grain growth [44]. Poetsche et. al. showed that the grain growth in FAST sintering also depended highly on the powder pre-treatment; for example, wet milled powder resulted in more abnormal grains as well as a higher porosity [43].

2.3.2 Mechanism of Grain Growth Inhibition

During liquid phase sintering of tungsten alloys, grain growth may occur by Ostwald ripening, where small grains dissolve into the larger grains. Another grain growth mechanism may be atomic diffusion between solid particles [45]. The grain growth inhibitors have low solubility in the WC, so carbide additions may inhibit grain growth by segregating to the WC grain interfaces, changing the surface free energy of the WC particles [42, 44]. In addition, if a binder is used during the sintering, carbide additions dispersed in the binder may reduce the solubility of tungsten and carbon atoms in the binder, reducing WC grain growth [42]. As described above in Section 2.3, carbide additions successfully inhibited grain growth in binderless WC as well [43]. However, few studies have explored the addition of grain growth inhibitors to Ni-based superalloys, though Hf additions have been used to improve ductility and thermal capabilities.

In the preliminary study summarized in Appendix B, silicon carbide (SiC) nanoparticles were added to Inconel 625 powder as a grain growth inhibitor, and the powder mixture was then sintered using FAST. The addition of SiC improved the relative density of the FAST-sintered materials (from 98.7% to 100%), and the FAST process minimized grain growth. The addition of SiC resulted in multiple phase formation at the grain boundaries, which led to an increase in hardness as well as elastic modulus.

2.4 Previous Work on Hafnium Additions to Nickel-Based Superalloys

Because Inconel 625 is not a superalloy used for turbine applications, the current study focuses on the the Ni-based superalloy CM247LC, a material produced for directionally-solidified turbine blades. In the current study, HfC was chosen as the carbide addition because Hf has previously been included in Ni-based superalloys to successfully improve ductility and creep resistance at high temperatures. Both Hf and HfC have a high thermal stability, with melting points of 2200 and 3900°C, respectively.

Hf can partition to both the γ and γ' phases, with the preference affected by the amount of chromium present in the alloy, as shown in an atom-probe tomographic and first-principles study by Amouyal, Mao and Seidman [46]. Because some Hf goes into solution in the nickel matrix, some of the Hf in contact with the air forms hafnium oxide and therefore improves oxidation resistant properties [4].

Carbides precipitate during the heat treatment of Ni-based superalloys, and Hf additions improve ductility in Ni-base superalloys by changing the carbide morphology. In a study by Kotval, Venables and Calder, the continuous network of script carbide allowed for brittle crack propogation in Alloy 718-LC, which does not contain Hf [47]. In comparison, the MM-004 alloy with 1 wt.% Hf exhibited a more ductile fracture, as the MC carbides were instead distributed throughout the matrix as discrete particles. Hf additions also improve ductility and creep resistance in columnar-grained Ni-based superalloys. In a study by Duhl and Sullivan, adding 2 wt.% Hf improved transverse creep ductilities and lifetimes in the directionally solidified Ni-based superalloy Mar-M200 while retaining the longitudinal properties of the columnar-grained material [48].

Because Hf has been shown to improve mechanical properties of various Ni-based superalloys, in this study, it is hypothesized that the addition of a small volume fraction of Hf or HfC particles may contribute towards higher thermal stability and improved mechanical properties of a Ni-based superalloy sintered using FAST.

Chapter 3
Objectives and Approach

3.1 Objectives

The objective of this thesis is to evaluate the effect of FAST processing parameters on the sintering and joining of Ni-based superalloys. The effect of sintering pressure, temperature, and time on the mechanical properties of hybrid Ni-superalloy disks manufactured using FAST will be discussed, and the effect of HfC additions to the powder-sintered rim material is also explored. As reviewed in Chapter 2, current joining methods for dissimilar Ni-based superalloys result in localized melting and a heat affected zone, leading to a weak interface. This thesis studies FAST as a potential joining alternative. FAST sinters a wide variety of materials and can join dissimilar materials via solid state joining or functional grading. Solid state joining can occur between solid and/or powder materials when their contact surfaces diffuse together as a result of the FAST process, while functional grading can occur when FAST sinters layers of powder with a gradient of composition. Because of FAST's known joining capabilities, it is hypothesized that FAST can join two dissimilar Ni-based superalloys to form a hybrid disk without a heat affected zone and with a strong interface between core and rim materials. Specifically, this thesis aims to:

- Study the correlation between sintering pressure, temperature, and time on sintered samples' porosity, phase morphology, and mechanical properties including hardness and elastic modulus.
- Study the effect of hafnium carbide additions on the hardness, elastic modulus, ductility, and strength of sintered samples.

- Study the bond strength between two dissimilar Ni-based superalloys joined using FAST.
- Study the correlation between microstructure and material strength.

These studies will lead to greater understanding of the FAST sintering mechanism and the effect of FAST process parameters on the room-temperature mechanical properties of Ni-based superalloys. The knowledge gained may pave the way for future efforts in manufacturing hybrid turbine disks.

3.2 Approach

Single-material disks were sintered from Ni-based superalloy powder using FAST, and hybrid disks were also formed using Ni-based superalloy powder as the rim material. A commercial Ni-based superalloy plate of contrasting mechanical properties was chosen as the core material for the hybrid disks. Various amounts of hafnium carbide powder (0-5 vol.%) were added to form the sintered single-material disks. The effect of the carbide additions on mechanical properties and microstructure was determined. Microscopy, sound velocity measurements, Vicker's hardness testing, and room-temperature tensile testing were the main analysis tools to characterize the sintered and joined materials. Chapter 4 describes detailed sintering and testing methology.

FAST sintering of Ni-based superalloy powder in a single-material disk was first studied. The superalloy powder was placed in a die mold lined with graphite foil, and the powder was compacted and sintered using FAST, forming disks of 40 and 80 mm diameter and 3-4 mm thickness. Axial pressure and direct current were applied through both the mold and the Ni-superalloy material during the sintering process, as described in Chapter 4. The effect of sintering parameters on microstructure and mechanical properties was explored using microstructural inspection and mechanical testing.

After determining sintering parameters to achieve high density, the effect of hafnium carbide particle additions to the Ni-based superalloy powder was explored. The hafnium carbide particles were mixed with the Ni-superalloy powder, and the powder mixture was sintered using FAST, forming disks of 40 and 80 mm diameter and 3-4 mm thickness. The microstructure and mechanical properties of the resulting disks were compared to that of the disks without carbide additions.

Finally, FAST was used to manufacture hybrid disks, using the Ni-based superalloy powder as the rim material and the lower-strength Ni-based superalloy Inconel 718 as the core material. Room-temperature tensile testing was performed on the material interface and on the parent materials to determine the strength of the interface.

Chapter 4
Materials and Methods

This chapter discusses the methods used to sinter monolithic and hybrid Ni-based superalloy disks via FAST.

4.1 Materials

The Ni-based superalloy sintered in this study was CM247LC, a superalloy specifically designed for directionally solidified turbine blade applications [3]. CM247LC is derived from the superalloy Mar-M247 and exhibits an increased ductility and carbide stability compared to the parent material [49]. Table 4.1 lists the nominal elemental composition. The powder used in this work consists of spherical particles of diameter 1̃05 to 149 µm. Although the ASM Alloy Digest lists the density of CM247LC as 8.54 g/cc in [3], the measured density of sintered samples with zero porosity was 8.62 g/cc. Cross-sectional inspection verified the lack of porosity. The difference from the reference value possibly resulted from impurities in the powder or a slight deviation of the powder material from the nominal composition in Table 4.1.

Hafnium carbide (HfC) was chosen as the additive to improve the thermal and mechanical properties of the CM247LC material. The theoretical density of hafnium carbide is 12.20 g/cc, higher than the base CM247LC material. The HfC particle size is 0.4 to 4 µm, significantly smaller than the CM247LC powder particle size. The HfC particles have an irregular shape from the milling process used to reduce particle size, unlike the spherical CM247LC particles, as shown in Figure 4.1.

The core of the FAST-joined hybrid disks in this thesis was machined from an

Table 4.1. Nominal Composition of CM247LC [3]

Element	Percentage
Carbon	0.07
Chromium	8.1
Cobalt	9.2
Molybdenum	0.5
Tungsten	9.5
Titanium	0.7
Aluminum	5.6
Boron	0.015
Zirconium	0.010
Tantalum	3.2
Hafnium	1.4
Nickel	Balance

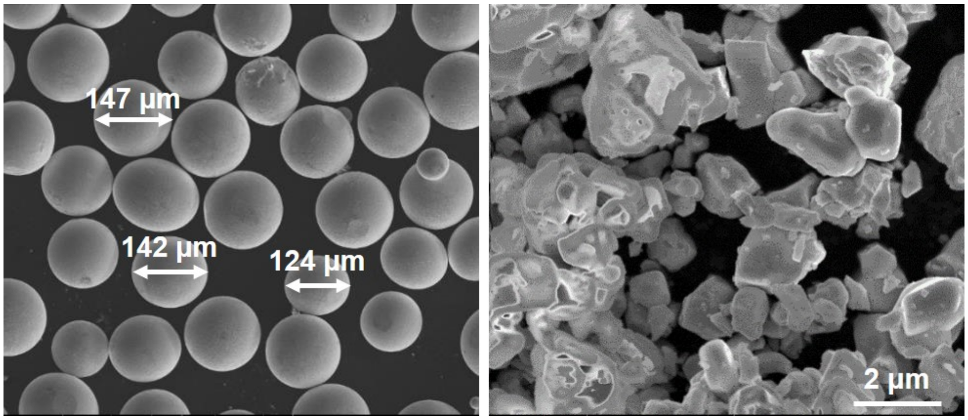

Figure 4.1. SEM micrographs of CM247LC powder (left) and hafnium carbide powder (right).

1/8-inch Inconel 718 plate obtained from Rolled Alloys Inc. The plate was vacuum induction melted, electro-slag refined, cold-rolled, and annealed. No further heat treatments were performed on the material before the FAST process.

The X-ray diffraction (XRD) spectrums of the powders were measured to determine the phases of each material. Diffraction spectrums were collected with a PANalytical Empryean X-ray Diffractometer, using K_α copper radiation with a wavelength of 1.54 Å. The XRD spectrum of each powder shows only one phase;

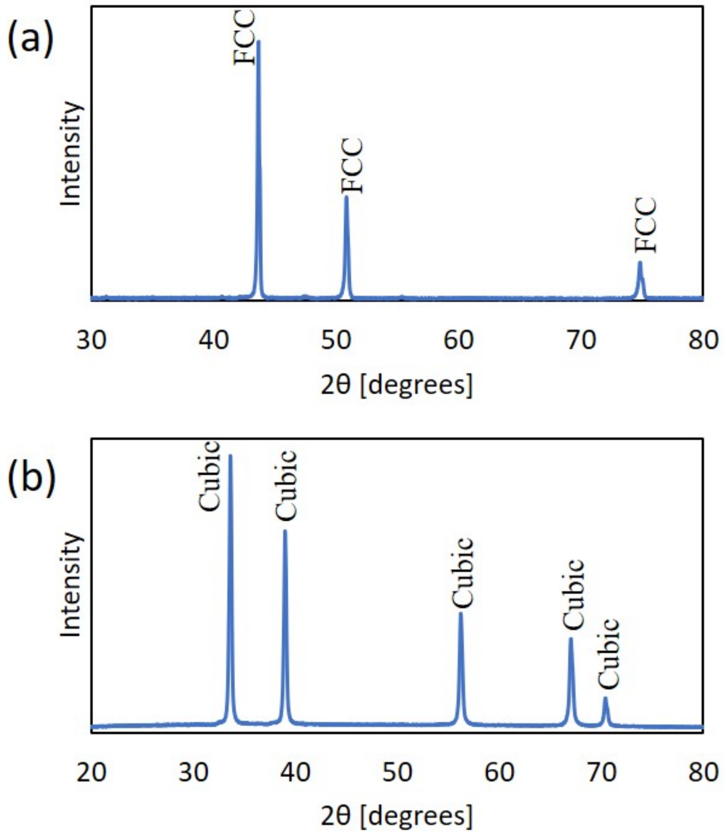

Figure 4.2. X-ray diffraction spectrums of (a) CM247LC powder and (b) HfC powder.

CM247LC exhibits a face-centered cubic (FCC) crystal structure with a lattice parameter of 3.587 Å while the HfC powder exhibits a cubic crystal structure with a lattice parameter of 4.63 Å. The single phase of the CM247LC powder shows that the pre-alloyed powder consists of a single γ phase with alloying elements in solid solution. The two XRD spectrums are shown in Figure 4.2.

4.2 Methods

4.2.1 FAST Sintering Process

Penn State Applied Research Laboratory owns three FAST units manufactured by FCT Systeme GmbH (25, 250, and 325 metric ton loading capability), as shown in Figure 4.3. In the current study, the 25-ton unit was used to sinter Ni-based

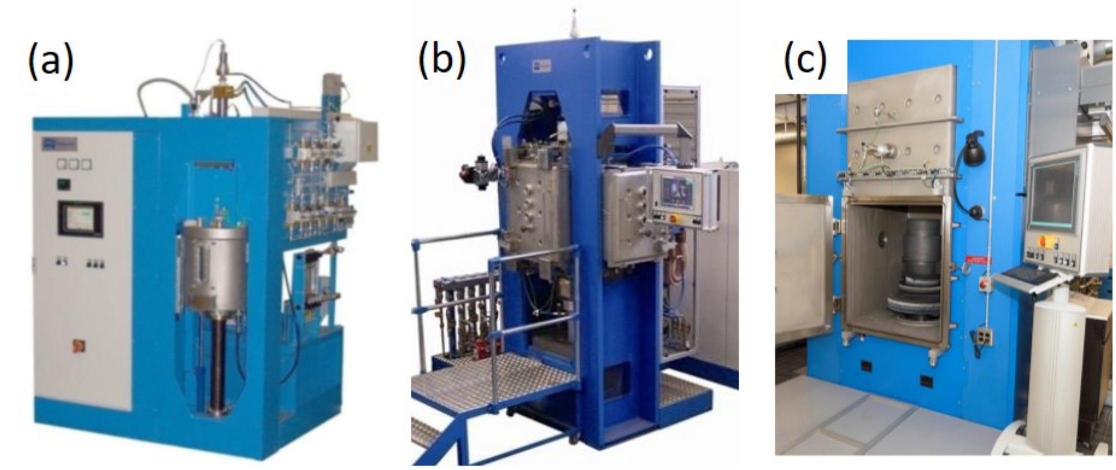

Figure 4.3. FAST units at Penn State. (a) Fast unit with maximum 25 metric ton pressing force, (b) FAST unit with maximum 250 ton pressing force, and (c) FAST unit with maximum 325 ton pressing force.

superalloy disks of 40 and 80 mm diameter and hybrid disks of 70 mm diameter. The 250-ton unit was used to sinter one hybrid disk of 200 mm diameter.

Two mold materials were explored while sintering Ni-superalloy disks. Traditionally, molds are made of graphite, which has high strength at high temperatures. Because the graphite molds cannot withstand pressures above 50 MPa, the higher-strength material carbon fiber reinforced carbon (CFRC) was explored as a second mold material to allow for higher pressures during the sintering process. Graphite molds produced monolithic disks of 40 and 80 mm diameter while molds with a combination of graphite and carbon fiber reinforced carbon (CFRC) parts produced the hybrid disks. The two mold materials behaved similarly, but ultimately, graphite was the better material for this project. CFRC did not distribute the current as evenly as the graphite material, creating hot spots that melted portions of the Ni-based superalloy material. As a result, some of the melted material seeped into the pores of the CFRC die parts.

During the sintering of powder materials to form disks, axial pressure and temperature were controlled throughout each sintering run. For both the 25-ton and 250-ton units, pressure was applied vertically, and a pyrometer measured the temperature of the material during sintering near the top of the sample. Samples were sintered under a vacuum environment, and temperature was controlled using a direct current. To minimize the thermal gradient between the center and the outer

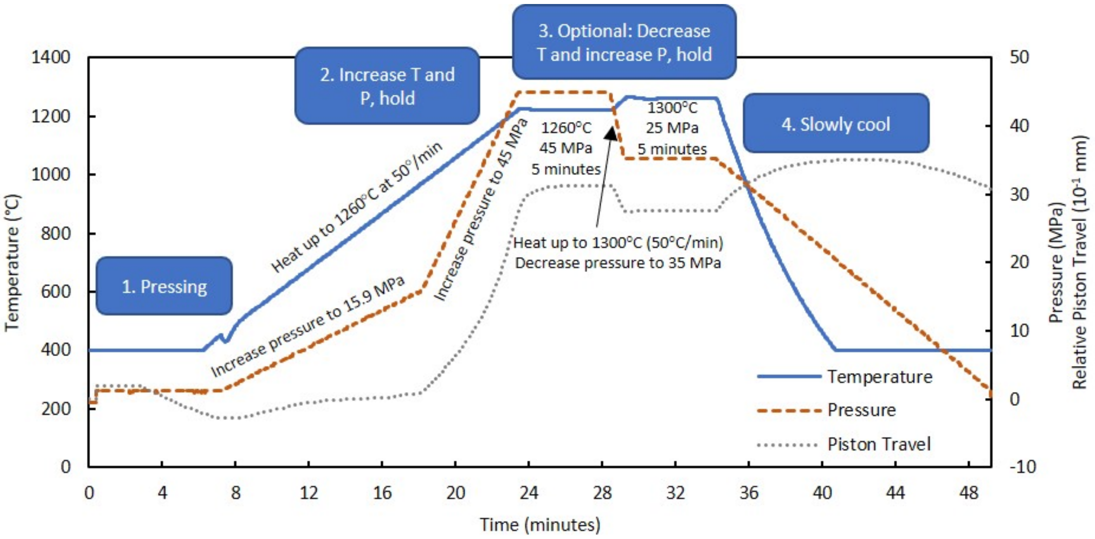

Figure 4.4. Plot of sintering parameters for an 80 mm diameter CM247LC disk. This disk was sintered first at 45 MPa and 1260°C for 5 minutes, then at 25 MPa and 1300°C for 5 minutes before cooling.

edges of the samples, carbon fabric was placed around the die assembly during sintering as an insulator.

Sintered disks underwent a predetermined sintering process, with sintering temperature, time and pressure as variables. Figure 4.4 shows a plot of the sintering process: first, the rams steadily applied 5 kN of force to initially compact the powder in the graphite die. Second, the material temperature increased to the specified temperature at a rate of 50°C per minute. The pressure simultaneously increased, first at a lower rate and then at a higher rate so the desired sintering pressure was reached at the same time as the desired temperature. The material was held at this pressure and temperature for a given time. An optional hold step with an increased temperature and decreased pressure immediately followed; by increasing temperature for the second hold step, the material reached a higher temperature and exhibited further grain growth. Decreasing pressure reduced flashing, where material at the edge of the samples moves into the gap between the die punch and die containment cylinder, resulting in a raised edge. After the hold step(s), the current was turned off and the water-cooled rams quickly cooled the die assembly while pressure was gradually released.

Table 4.2. 40 mm Diameter Disks: Sintered CM247LC Powder

Sample #	*d* (*mm*)	*th.* (*mm*)	*P* (*MPa*)	*T* (*°C*)	*t* (*min.*)	ρ (*g/cc*)	ρ_{rel} (*%*)
2803	40	3	35	1150	25	7.92	91.9
2804	40	3	35	1200	25	8.26	95.9
2809	40	3	35	1225	25	8.52	98.8
2814	40	3	35	1225	15	8.40	97.4
2815	40	3	45	1225	15	8.53	98.9
2906	40	3	45	1225	15	8.59	99.6

4.2.2 Sintering of 40- and 80-mm-diameter CM247LC disks

The sintered samples' size and sintering parameters were constrained by the FAST unit capabilities, die material strength, powder temperature capabilities, and dimensions needed for tensile testing. To ensure a sufficient thickness for tensile testing, the thickness CM247LC disks was approximately 3 mm. 40-mm-diameter disks were first sintered to establish FAST parameters for high density, and 80-mm-diameter disks were then sintered to demonstrate scalability and to produce samples large enough for tensile testing. The graphite die cannot withstand over 50 MPa of pressing force for an 80 mm disk, so the hold step pressure was varied between 35 and 45 MPa. The hold step temperature was varied between 1150 and 1260°C, and the hold step time was varied between 15 and 25 minutes. Tables 4.2 and 4.3 list sintered disks of 40 mm and 80 mm diameter, respectively, along with the relative densities of each sintered disk. Densities were measured using Archimedes' method. To determine relative densities, the reference density of CM247LC was taken to be 8.62 g/cc, the density measured for a sample with no porosity seen in the cross-section.

4.2.3 Addition of Hafnium Carbide Particles

The effect of HfC additions to CM247LC powder before sintering on thermal stability and mechanical properties were experimentally investigated. Before sintering, a Turbula® Shaker-Mixer was used to mix the base CM247LC powder with the HfC powder for fifteen minutes. 1, 3, and 5 vol.% of HfC were added. After the powders

Table 4.3. 80 mm Diameter Disks: Sintered CM247LC Powder

Sample #	d (mm)	$th.$ (mm)	P (MPa)	T $(^\circ C)$	t $(min.)$	ρ (g/cc)	ρ_{rel} $(\%)$
2818	80	3	35	1225	12	8.28	96.1
2824	80	3	35	1225	15	8.43	97.8
2825	80	3	45	1225	15	8.47	98.3
2841	80	4.5	45	1225	15	8.49	98.5
2862	80	4.5	45	1240	15	8.58	99.5
2873	80	4.5	45	1250	15	8.59	99.6
2884	80	4.5	45	1260	15	8.60	99.8
2969	80	4	45-25	1260-1275	10-5	8.61	99.8
2971	80	4	45-25	1260-1275	10-5	8.61	99.9
3011	80	4	45-25	1260-1300	5-5	8.62	100.0
3013	80	4	45-35	1260-1300	5-5	8.63	100.1

Table 4.4. 40 and 80 mm Diameter Disks: Sintered CM247LC with HfC Additions

Sample #	vol.(wt.)% HfC	d (mm)	$th.$ (mm)	P (MPa)	T $(^\circ C)$	t $(min.)$	ρ (g/cc)	ρ_{rel} $(\%)$
2926	1 (1.4)	40	3	45	1225	15	8.58	99.1
2927	3 (4.2)	40	3	45	1225	15	8.62	98.8
2929	5 (7.0)	40	3	45	1225	15	8.62	98.0
2932	1 (1.4)	40	3	45	1250	15	8.62	99.5
2931	3 (4.2)	40	3	45	1250	15	8.64	99.0
2930	5 (7.0)	40	3	45	1250	15	8.66	98.4
2991	3 (4.2)	80	4	45	1250	15	8.62	98.8

were mixed, the powder mixtures were sintered to form 40- and 80-mm-diameter disks. The hold step pressure and time remained at 45 MPa and 15 minutes, respectively, while the hold step temperature either 1225 or 1250°C. The hold step temperature was increased because the material sintered at 1225°C did not result in a fully-dense material. The list of sintered disks with hafnium carbide additions is given in Table 4.4. Although HfC additions reduced the porosity of the sintered material, the HfC did not improve room-temperature mechanical properties or thermal stability as described in Chapter 6, so HfC additions were not used in the rim material during the sintering of hybrid disks using FAST.

Table 4.5. 70 mm Diameter Disks: Hybrid Disks with Solid Inconel 718 Core and Powder-Sintered CM247LC Rim

Sample #	Joining Angle (°)	d (mm)	$th.$ (mm)	P (MPa)	T $(^{\circ}C)$	t $(min.)$	ρ (g/cc)	$rim\ \rho$ (g/cc)	ρ_{rel} $(\%)$
2895	45	70	3.0	45	1225	15	8.36	8.40	97.5
2896	45	70	3.0	45	1200	30	8.38	8.47	98.3
2898	45	70	3.0	45	1200	25	8.35	8.45	98.0
2909	45	70	2.5	45	1200	25	8.37	8.45	98.0
2910	45	70	2.5	45	1225	15	8.43	8.56	99.2
2911	45	70	2.5	45	1225	15	8.41	8.53	98.9
2912	0	70	3.2	45	1200	25	8.32	8.35	96.8
2914	0	70	3.2	45	1225	20	8.44	8.52	98.8
2917	0	70	3.2	45	1225	20	8.43	8.51	98.7
2918	0	70	3.2	45	1225	20	8.46	8.55	99.2
2920	45	70	3.2	45	1225	15	8.37	8.46	98.1
2923	45	70	2.5	45	1225	15	8.40	8.51	98.7
1228	0	200	6.4	45	1275	30	8.48	8.62	100.0

4.2.4 Manufacturing Hybrid Disks

Producing hybrid disks using FAST requires a more unconventional die assembly. A novel die mold formed hybrid disks by sintering CM247LC powder for the rim material and simultaneously bonding the powder to a solid Inconel 718 disk. The die assembly is shown in Figure 4.5. Disks were manufactured either with a 45° joining angle between the two materials, as seen in Figure 4.5, or with a joining surface parallel to the thickness of the disk (0°). Powder height was adjusted so the thickness of the rim powder equalled the powder height above the solid inner disk, allowing the pressure on the disk to be maintained while the powder is compacted and sintered. To ensure equal powder heights, the mass of the powder in the rim and above the solid inner disk was calculated based on the material theoretical density and the die mold geometry. The list of disks sintered is summarized in Table 4.5.

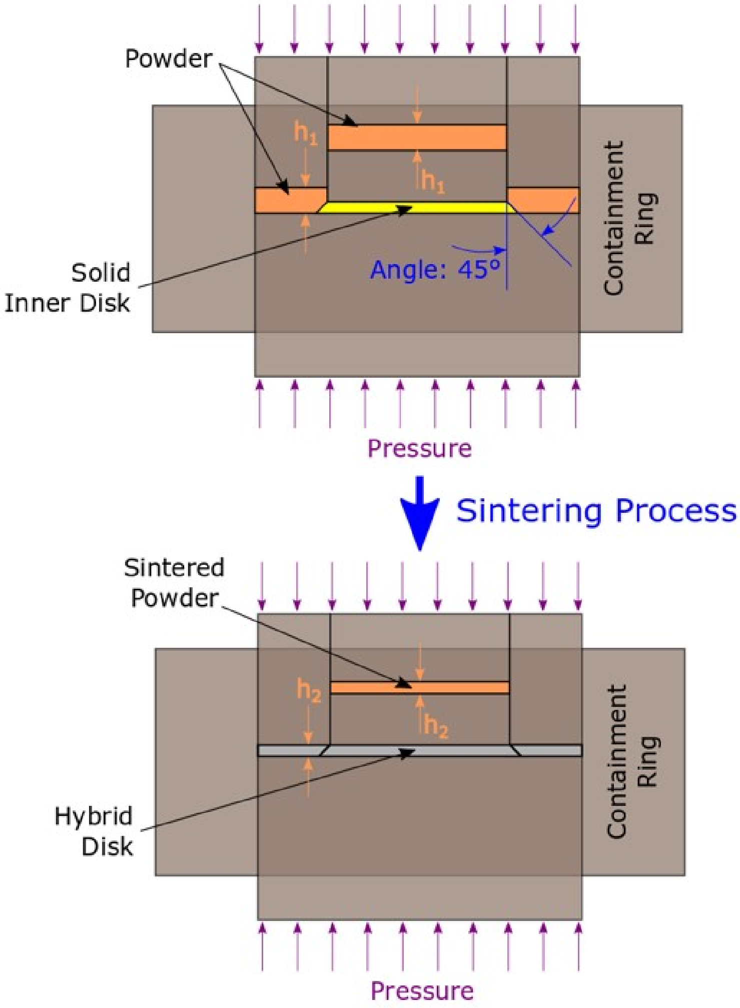

Figure 4.5. Assembly of graphite or CFRC die, machined inner disk, and powder rim for manufacturing of hybrid disk, before sintering and after sintering.

4.3 Analysis Methods

After sintering single-material and hybrid Ni-based superalloy disks using FAST, various methods were used to assess the microstructure and mechanical properties of the sintered materials.

4.3.1 Microstructural Inspection

Identifying microstructural characteristics is essential for understanding the FAST sintering mechanism and for identifying processing-structure-property relationships.

Cross-sectional inspection was performed using optical microscopy and scanning electron microscopy. Polished samples were etched using Waterless Kalling's reagent. The cross-section of a monolithic sample with 3 vol.% of hafnium carbide additions was inspected using an FEI Nova NanoSEM 630 scanning electron microscope (SEM) and a Talos F200X transmission electron microscope (TEM). In conjunction with microscopy, a combination of x-ray diffraction (XRD) and electron dispersive spectroscopy (EDS) was conducted for phase identification.

4.3.2 Mechanical and Thermal Characterization

Mechanical and thermal properties of the FAST-sintered Ni-based superalloy samples and hybrid disks were explored using various testing techniques.

The hardness of the sintered samples was measured using a standard Vicker's indenter with a 1 kg load. Hardness measurements were taken after sample cross-sections were polished to a 0.05 µm finish using a colloidal silica polishing suspension.

Elastic modulus was estimated via ultrasonic sound velocity. Determining the longitudinal and transverse sound velocity in a material allows one to approximate elastic modulus of thin, non-porous materials [50]. The quick, non-destructive method has seen promising results in previous FAST sintering studies [51–55] as well as in many other forms of material processing. The velocity was taken to be

$$V = \frac{th.}{\tau/2}, \tag{4.1}$$

where V is the sound velocity through the material, $th.$ is the sample thickness, and τ is the time for an ultrasonic pulse to travel through the material twice. Assuming an isotropic material, one can estimate Poisson's ratio ν to be

$$\nu = \frac{1 - 2(\frac{V_T}{V_L})^2}{2 - 2(\frac{V_T}{V_L})^2}, \tag{4.2}$$

where V_T is the transverse velocity and V_L is the longitudinal velocity. Young's Modulus E can then be calculated as

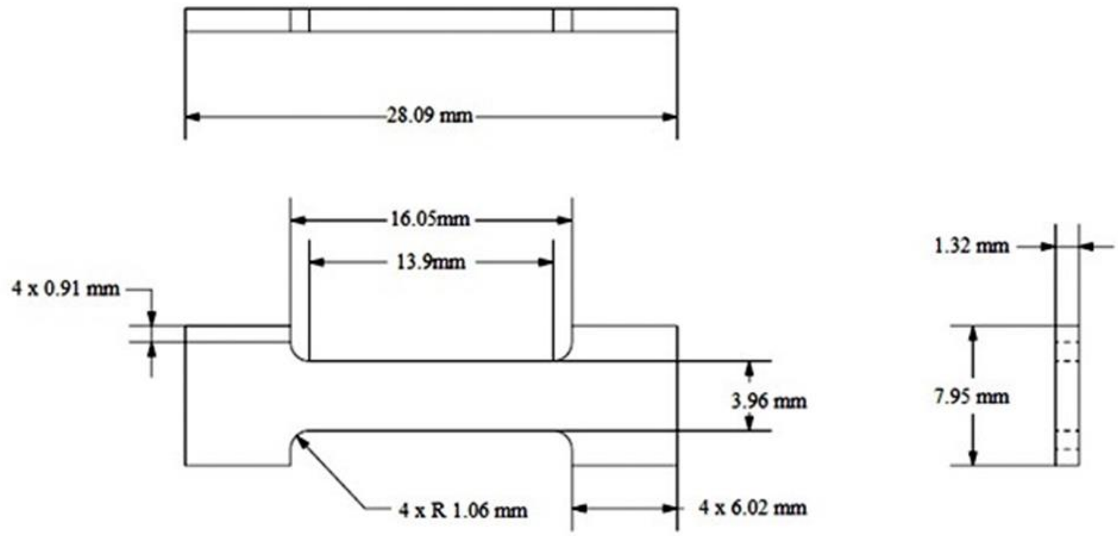

Figure 4.6. Subscale tensile specimen dimensions for tensile testing.

$$E = V_L^2 \frac{(1+\nu)(1-2\nu)}{1-\nu}. \tag{4.3}$$

Tensile tests were conducted to measure the materials' tensile strengths and elongation. Subsize tensile specimens were used, based on a scaled-down version of the ASTM standard. Figure 4.6 shows the tensile specimen dimensions: the length of the parallel section was 13.9 mm, the sample thickness was 1.32 mm, and the width of the parallel section was 3.96 mm. Tensile specimens were cut using wire electrical discharge machining (EDM) with a wire diameter of 0.010 inches. A strain rate of 0.05 mm/mm/min was applied. Because the tensile specimens were too small for an extensometer to measure strain, strain rate was calculated from the crosshead relative position. Measured strain is not accurate because of the large distance between the crossheads, so elastic modulus could not reliably be derived from the stress-strain curves. The elongation of the samples was measured manually after tensile fracture.

Finally, differential scanning calorimetry (DSC) determined the melting point of sintered samples. An increase in melting temperature with increased hafnium carbide additions would imply greater thermal stability due to the carbide additions.

Chapter 5
Sintered CM247LC Disks

This chapter discusses the microstructure and mechanical properties of CM247LC disks without HfC additions sintered from powder using FAST, with sintering parameters as described in Section 4.2.2.

5.1 Sintering CM247LC Powder to High Density

5.1.1 Temperature and Pressure for High Density

High sintering pressures (45 MPa) and temperatures (1225°C) were critical in sintering CM247LC powder to nominal density. To determine the sintering parameters of the CM247LC powder for high relative density, small samples of 40 mm diameter were initially sintered, with sintering parameters listed in Table 4.2. A sintering pressure of 45 MPa and a sintering temperature of 1225°C was required to reach nominal density (99.6%), as seen in Figure 5.1b.

5.1.2 Scalability Study

As the diameter of the sintered disks was increased from 40 mm to 80 mm, higher porosity was observed at the sample edges due to inhomogenous temperature and pressure during the sintering process. When 80-mm-diameter disks were sintered using the same pressure, sintering temperature, and hold time as the 40-mm-diameter disks that reached nominal density, porosity was seen, especially at the sample edges, as shown in Figure 5.1c and 5.1d. The porosity may be because the 80-mm-diameter disks were not heated as evenly throughout the sample as the 40-

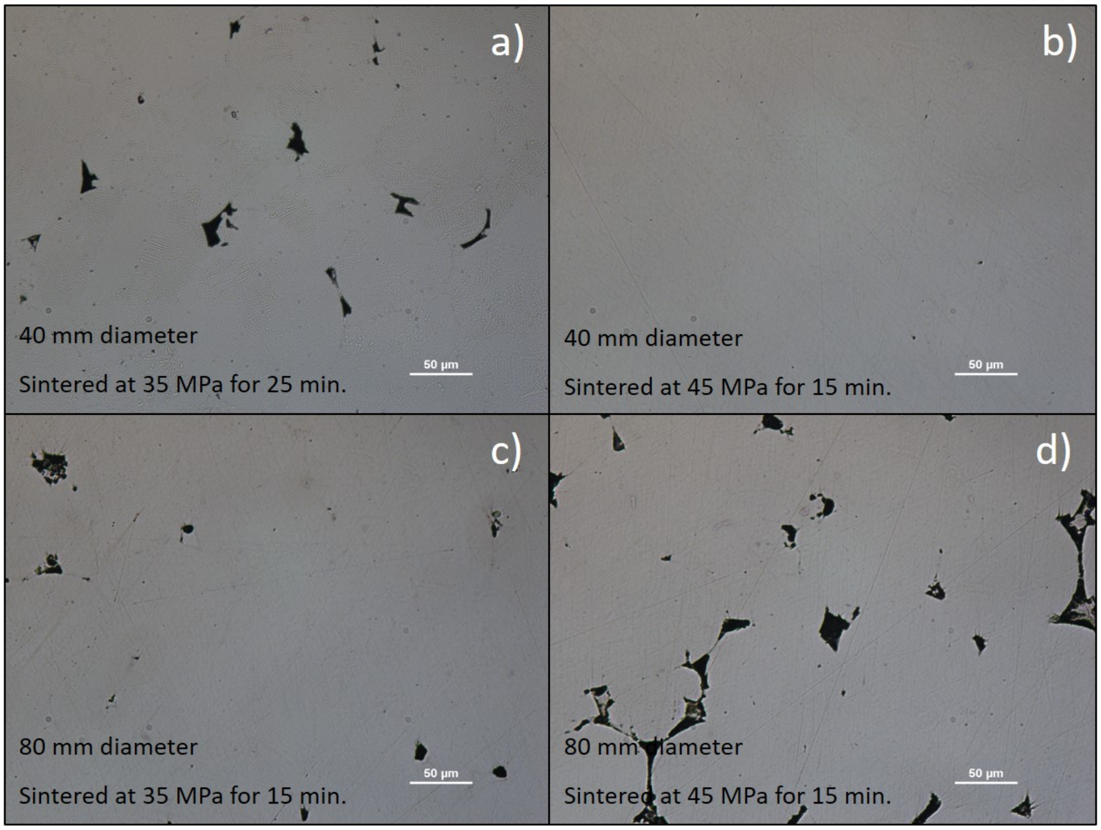

Figure 5.1. Optical micrographs of sintered CM247LC before etching. Cross-sections taken near the edges of the sintered disks with various sintering parameters and disk sizes. Samples sintered at 1225°C. Relatives densities are (a) 98.8%, (b) 99.6%, (c) 97.8%, and (d) 98.3%

.

mm-diameter disks, with the edges of the samples reaching the target temperature more slowly than the centers, allowing for faster diffusion between the CM247LC particles at the center of the samples. The porosity gradient may also be attributed to the difference in pressure throughout the sample; there may be a slightly lower pressure at the sample section in contact with the ductile graphite foil lining the inside edge of the die, causing the porosity to migrate from the center of the sample outwards, as shown in Figure 5.2.

Due to the strength of the graphite die, sintering pressure could not exceed 45 MPa, so diffusion and densification was improved through increased sintering temperature. The reduction of porosity with increased sintering temperature is seen in Figure 5.3, which shows the porosity at the edges of sintered 80 mm samples.

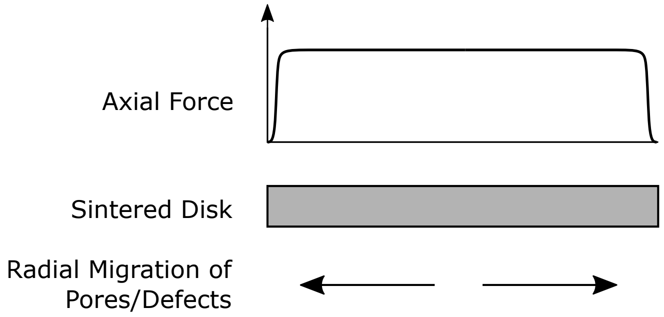

Figure 5.2. Possible variation of axial force with radius. Hypothesized migration of pores and defects with increasing sintering temperature is shown.

However, significant porosity remained at the edge of the samples, though the porosity near the center of the 80 mm sample sintered at 1260°C was negligible, suggesting 100% relative density near the center of the sample.

A two-step sintering process further reduced porosity and increased grain size. An increase in sintering temperature reduced porosity and increased grain sizes, but with an increase in sintering temperature, flashing also increased at the sides of the sintered disks, where the Ni-superalloymaterial rose up along the sides of the disks to form an elevated ring at the rim of the disks. The flashing results from increased ductility of the samples at high temperatures. To combat the flashing while still sintering the material at temperatures higher than 1260°C, pressure was reduced and temperature was simultaneously increased at the middle of the sintering step, thus splitting the sintering step into two different steps. The sintered material therefore reached a higher temperature while experiencing a lower pressure, which successfully reduced the flashing, as seen in Figure 5.4.

The material sintered at higher temperatures using the two-part hold step process also exhibited a smaller amount of porosity. Porosity was generally greater at the edge of the samples, with decreasing porosity as sintering temperature increases, as seen in Figure 5.5. The decreasing porosity demonstrates that volumetric sintering dominates at the center of the disk, and porosity and defects migrate to the edge of the disk during sintering. The samples sintered first at 1260°C for 5 minutes then at 1300°C for 5 minutes exhibited little to no porosity away from the edge, but some porosity was still seen at the very edge of these samples. Further optimization of sintering time, pressure, and temperature is required to achieve minimum porosity and defects at the edge of the disks.

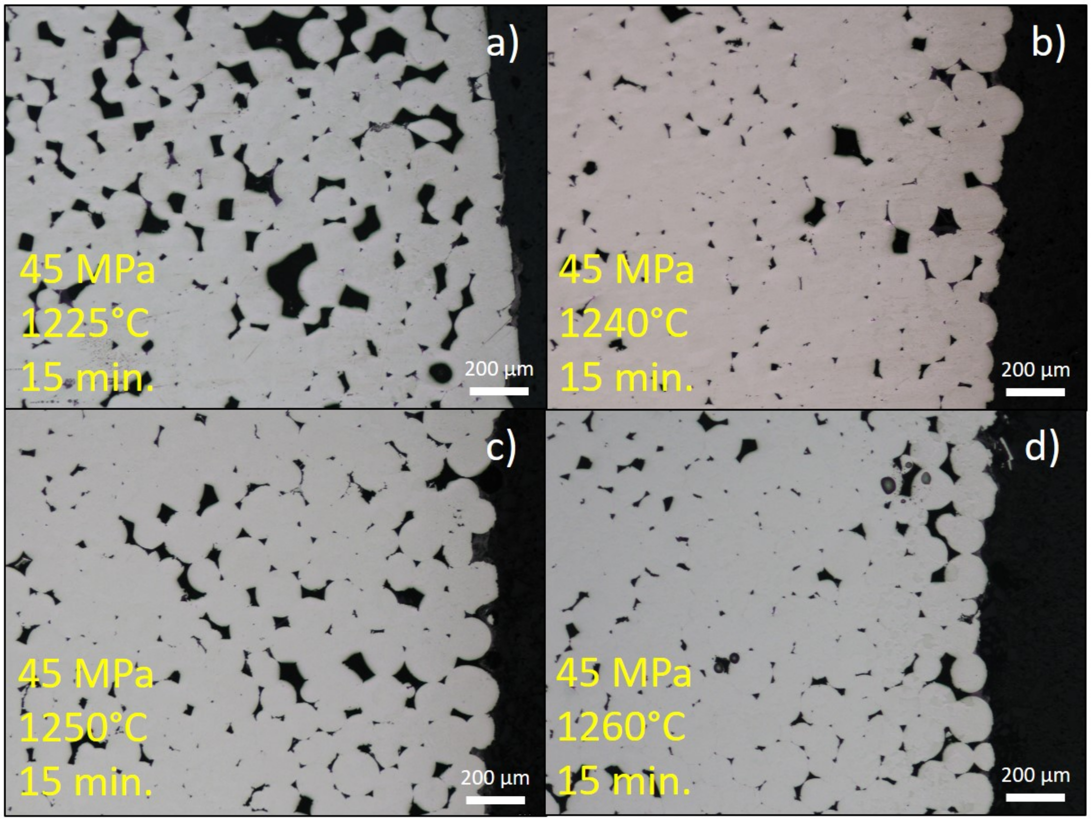

Figure 5.3. Optical micrographs of the edge of sintered CM247LC samples, sintered at 45 MPa for 15 minutes at various temperatures. The samples were sintered at (a) 1225°C, (b) 1240°C, (c) 1250°C, and (d) 1260°C.

5.2 Microstructural Inspection

5.2.1 Optical Microscopy

Microstructural inspection of the 80 mm samples was performed using optical microscopy. With an increase in sintering temperature was an increase in grain size, a reduction in porosity and a reduction in the number of retained spherical structures that remained from the spherical superalloy grains, as seen in Figure 5.6. The CM247LC powder sintered at 1225°C showed significant porosity, as seen in Figure 5.6a, as well some retained spherical structures that remained from the spherical superalloy powder. The grain size of the sintered powder was approximately 16 µm, smaller than the initial powder size. Because the CM247LC would be used as the rim material, a larger grain size is desired to improve creep

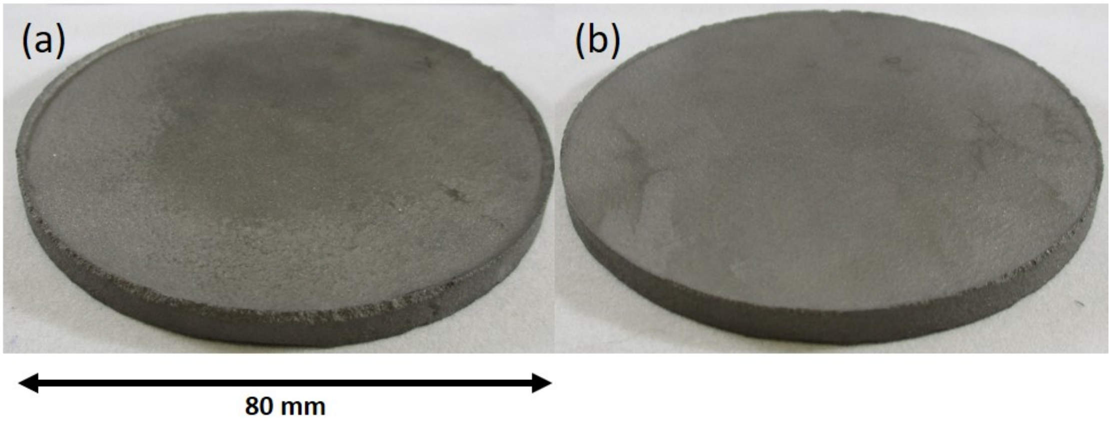

Figure 5.4. Comparison of amount of flashing seen in sintered CM247LC disks. (a) CM247LC powder sintered at 45 MPa and 1260°C for 15 minutes. (b) CM247LC powder sintered first at 45 MPa and 1260°C for 10 minutes followed by 25 MPa and 1275°C for 5 minutes.

resistance at high temperatures. Removing the retained spherical structures of the CM247LC particles is also desired. As the sintering temperature increased from 1225°C to 1260°C, the number of spherical structures decreased, with the sample sintered at 1260°C generally showing large, equiaxed grains with a 31 µm grain size. To further increase the grain size to increase creep resistance, the powder was sintered at higher temperatures using the two-step process described in Section 4.2.1.

The resulting microstructure of the samples sintered at temperatures higher than 1260°C is seen in Figure 5.7. The grain size increased to 40 µm at a maximum sintering temperature of 1300°C compared to the grain size of 16 µm for the 80 mm sample sintered at 1225°C.

5.2.2 Phase Formation

XRD and EDS were used to identify phases formed during the FAST sintering process of CM247LC powder. Figure 5.8 shows a comparison of the XRD spectrum of the CM247LC powder and a sintered CM247LC sample. Both samples exhibited a strong FCC crystal structure, and no significant difference was observed before and after the FAST process. The lack of difference shows that any new phases formed must either be a very small volume fraction in the sintered sample or have the same FCC crystal structure and a similar lattice parameter. The latter is supported by

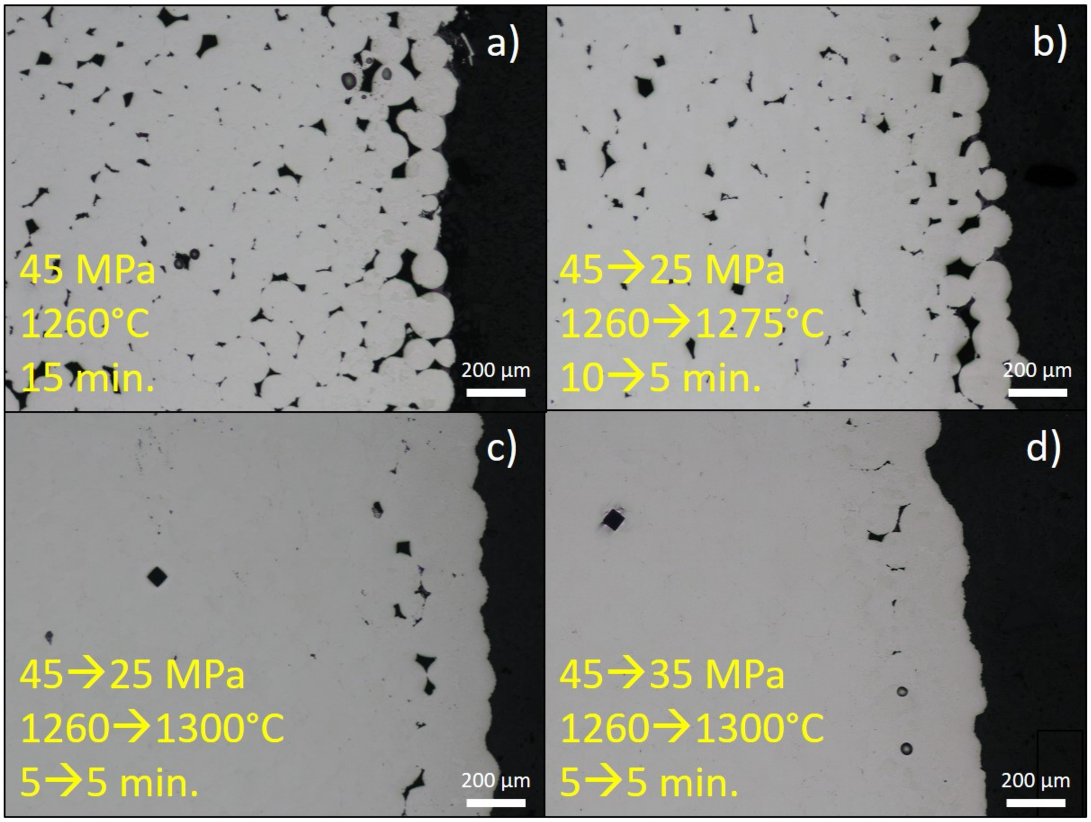

Figure 5.5. Optical micrographs of the edge of sintered CM247LC samples, sintered at 45 MPa for 15 minutes at various temperatures and pressures. The samples were sintered at (a) 1225°C for 15 minutes at 45 MPa, (b) 1260°C for 10 minutes at 45 MPa followed by 1275°C for 5 minutes at 25 MPa, (c) 1260°C for 5 minutes at 45 MPa followed by 1300°C for 5 minutes at 25 MPa, and (d) 1260°C for 5 minutes at 45 MPa followed by 1300°C for 5 minutes at 35 MPa.

the EDS results seen in Figure 6.2, which shows the elemental composition of the interface between a hafnium carbide particle and the Ni-superalloy matrix. It can be assumed the Ni-superalloy portion shown in the EDS image is similar to the sintered Ni-based superalloy without HfC additions, as the HfC did not dissolve into the Ni-superalloy matrix. The EDS results of the sintered CM247LC material showed clear γ' precipitates within a γ matrix, as expected of Ni-based superalloys. The γ' precipitates were nickel- and aluminum-rich while the γ phase was rich in Ni, Cr, Co, and W. γ' precipitates in Ni-based superalloys have the same FCC crystal structure as the Ni matrix and a very similar lattice parameter, allowing the precipitates to strain the matrix and therefore increase the matrial strength.

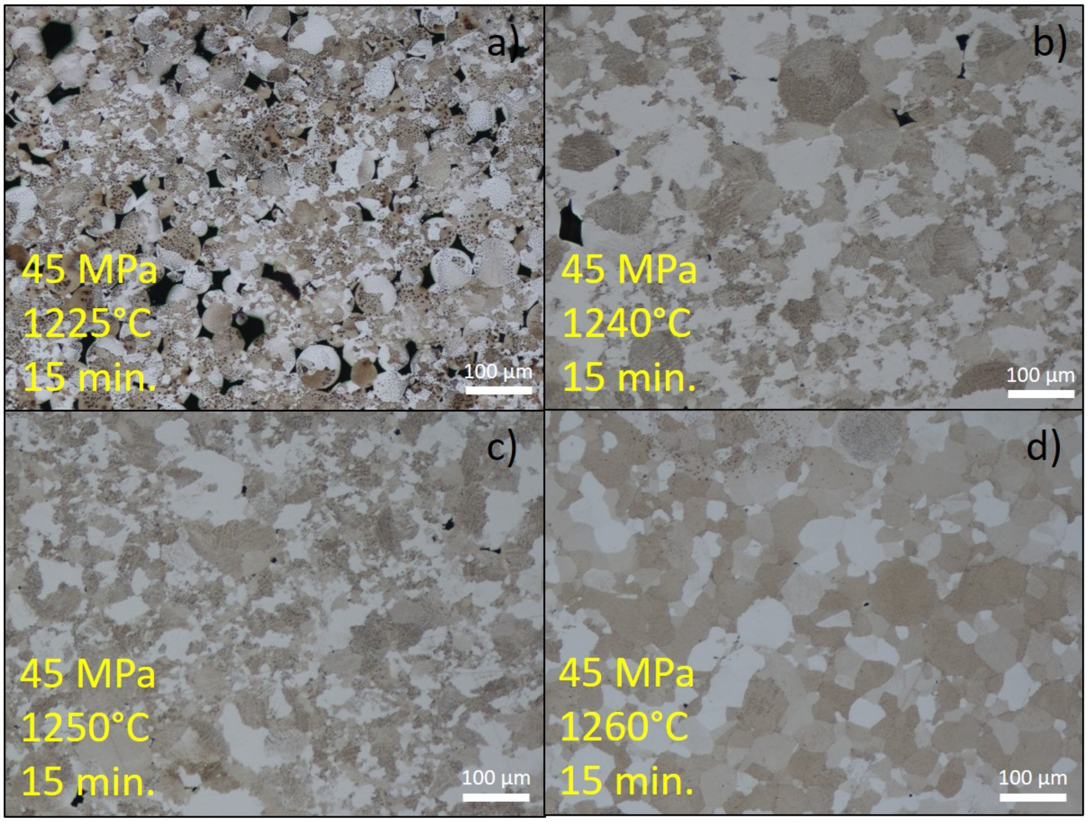

Figure 5.6. Optical micrographs of sintered CM247LC samples, sintered at 45 MPa for 15 minutes at various temperatures. Waterless Kalling's Etch. The samples were sintered at (a) 1225°C, (b) 1240°C, (c) 1250°C, and (d) 1260°C.

Because of the similar crystal structure, one would not be able to see the difference with an XRD spectrum alone.

5.3 Mechanical Characterization

5.3.1 Elastic Modulus

Elastic modulus was calculated by measuring ultrasonic sound velocity through the sintered samples, with results summarized in Figure 5.9. Sound velocity was measured at the center of the samples as well as 1/4" from the edge of the samples. The elastic moduli for all the samples are comparable, around 230-240 GPa. The disk sintered at 35 MPa exhibited a lower elastic modulus than the samples sintered at higher pressures, but porosity in the samples sintered at 35 MPa may have

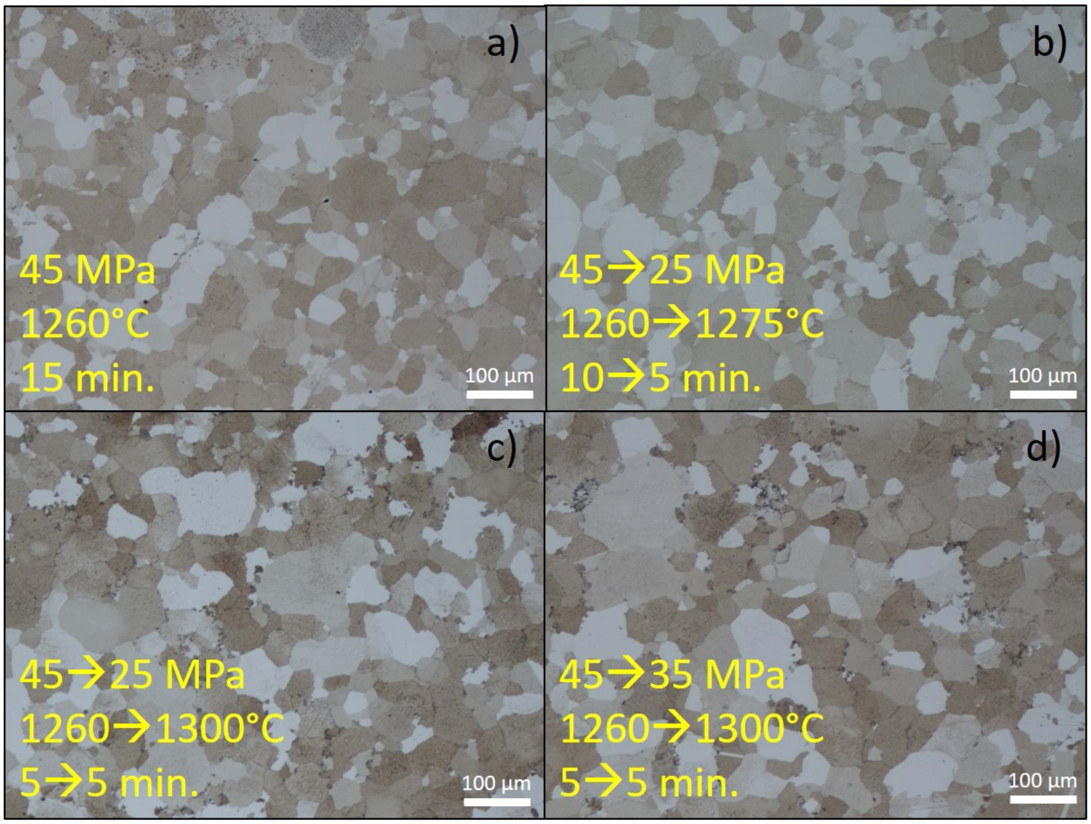

Figure 5.7. Optical micrographs of sintered CM247LC samples, sintered at 45 MPa for 15 minutes at various temperatures and pressures. Waterless Kalling's Etch. The samples were sintered at (a) 1225°C for 15 minutes at 45 MPa, (b) 1260°C for 10 minutes at 45 MPa followed by 1275°C for 5 minutes at 25 MPa, (c) 1260°C for 5 minutes at 45 MPa followed by 1300°C for 5 minutes at 25 MPa, and (d) 1260°C for 5 minutes at 45 MPa followed by 1300°C for 5 minutes at 35 MPa.

skewed the sound velocity measurements. The elastic moduli at the center of each sintered disk did not differ significantly from the measurements at the edge, showing that the material was generally homogenous throughout the sample.

5.3.2 Hardness

The hardness of the sintered samples was measured using a 1 kg load and a standard Vicker's indenter, with values shown in Figure 5.10. As with elastic modulus, the hardness values of the 80-mm-diameter disks did not differ significantly with the different sintering parameters. The samples sintered at temperatures higher than 1260°C exhibited a slightly higher hardness than those sintered at lower

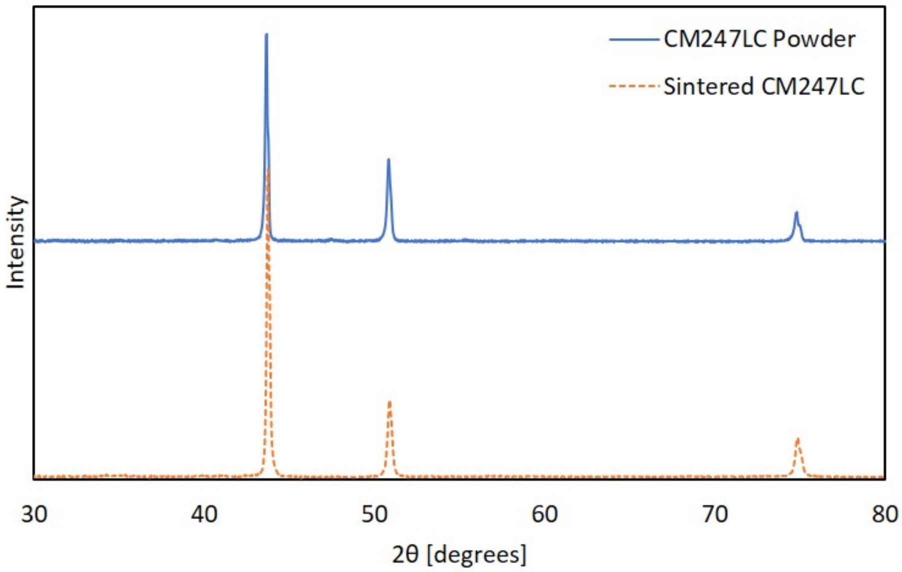

Figure 5.8. XRD spectrum of both sintered and unsintered CM247LC powder. The sintered CM247LC sample had diameter 80 mm and thickness 3 mm, sintered at 35 MPa and 1225°C for 15 minutes.

temperatures, possibly due to phase transformation during the sintering process.

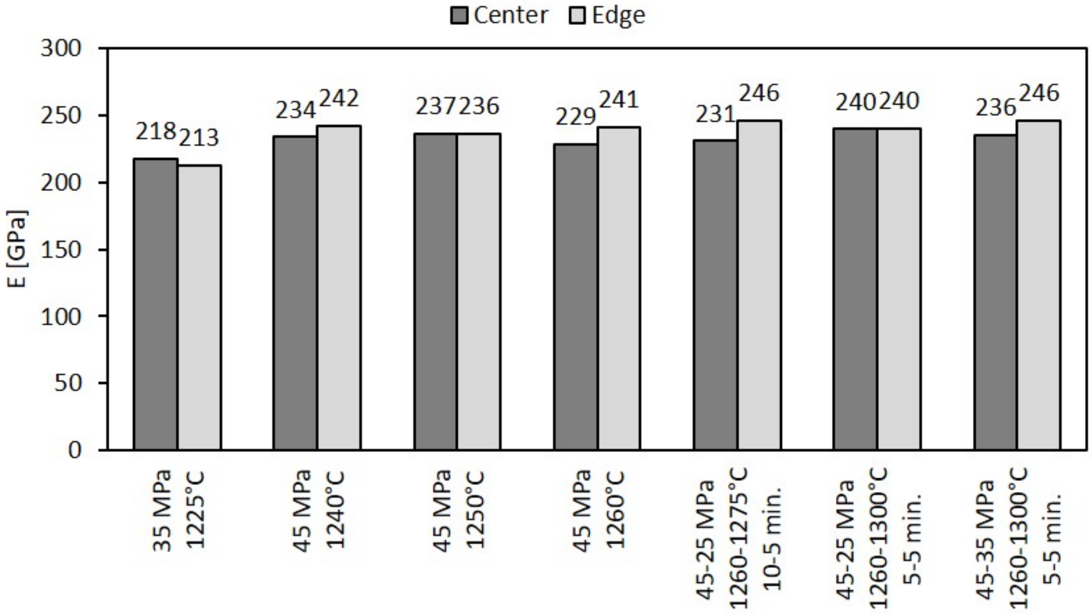

Figure 5.9. Elastic modulus of sintered 80 mm CM247LC disks at different sintering parameters. Samples with a single hold step were sintered for 15 minutes.

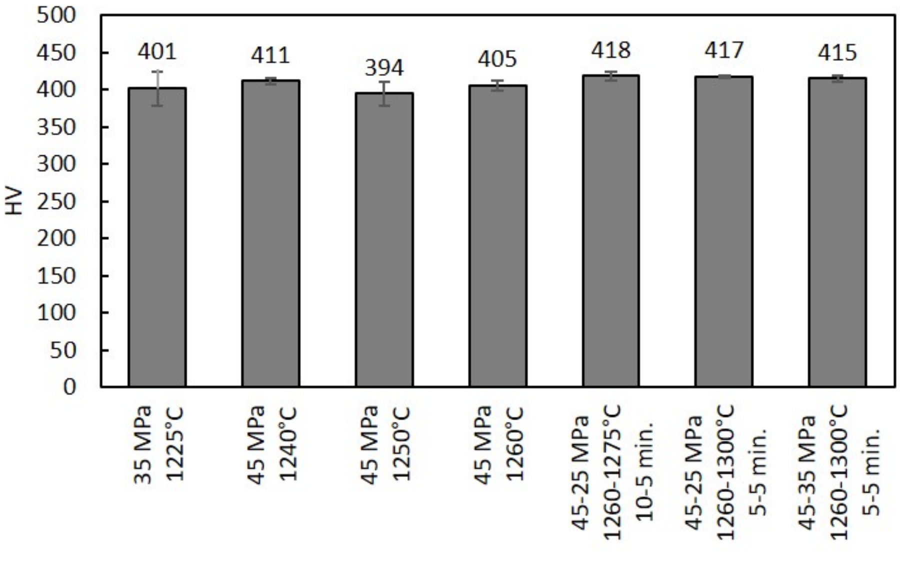

Figure 5.10. Vicker's hardness of sintered CM247LC samples vs. sintering parameters. Samples with a single hold step were sintered for 15 minutes. Measurements were taken near the edge of the sintered samples.

Chapter 6

CM247LC Powder Sintered with Hafnium Carbide Additives

In this chapter, the effect of hafnium carbide additions to CM247LC powder on FAST-sintered disks will be discussed.

6.1 Microstructural Inspection

6.1.1 Effect of HfC additions on Porosity

The addition of 1, 3, and 5 vol.% of HfC particles minimized the porosity of the sintered samples, even at the lower sintering temperature of 1225°C. The relative densities of the sintered samples are listed in Table 4.4. Even with the addition of 1 vol.% of HfC, the relative density increased from 97.8% to 99.1% at a sintering temperature of 1250°C by adding HfC particles. Subgrains are seen within the individual grains surrounded by HfC, as shown in Figure 6.1.

The increase in relative density may be a result of two different mechanisms: firstly, the reduction in porosity may be due to the greater surface area from the addition of the fine HfC particles. Because the HfC particles remained at the grain boundaries, as seen in Figure 6.1, the greater surface area may have promoted diffusion between the CM247LC particles. A second hypothesis is that the HfC instead slowed the diffusion of the CM247LC powder at the powder surfaces in a grain-growth-inhibition effect. The slower diffusion may allow porosity to migrate out of the sintered material so no large voids or pores are trapped within the material.

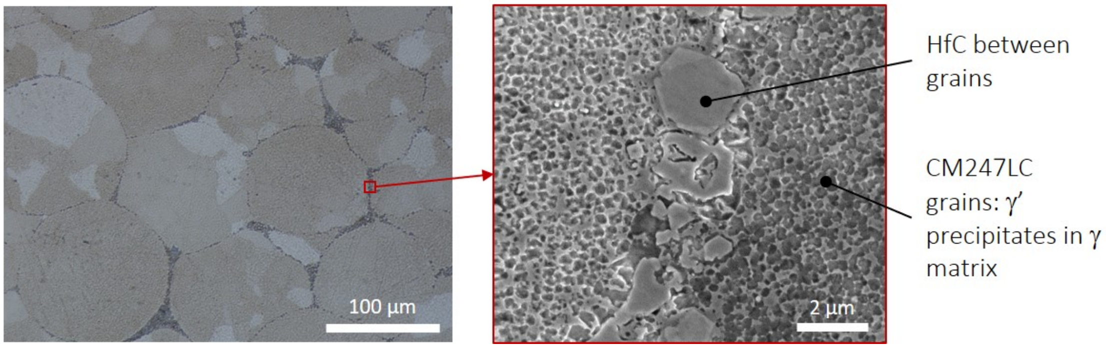

Figure 6.1. Optical and SEM micrographs of sintered CM247LC powder with 5 vol.% HfC additions, sintered at 45 MPa and 1225°C for 15 minutes.

6.1.2 Interface between HfC and CM247LC

The interface between the small HfC particles and the Ni-superalloy matrix is free of porosity and defects. Using a transmission electron microscope, one can see the sharp interface between the HfC particles and the Ni-superalloy matrix, as in Figure 6.2. Figure 6.3 shows the elemental composition across the interface between a HfC particle and the Ni-superalloy matrix. The composition changed smoothly from HfC to a phase rich in Ni, Cr, and Co (all major elements in the CM247LC composition). Based on the compositional plot, the interface seems to be less than 30 nm in width. The interface may be even sharper; some of the interface width may be due to the resolution of the EDS scan. No delamination, pores, or separate phase formation is found between the HfC particles and the Ni-superalloy matrix.

6.2 Mechanical Characterization and Thermal Properties

6.2.1 Elastic Modulus and Hardness

When measuring the elastic modulus via acoustic sound velocity, the elastic modulus did not vary significantly with the different amounts of HfC, as seen in Figure 6.4a. The measured elastic modulus approximately equalled that of the sintered CM247LC with no HfC additions, with values between 240 and 250 GPa. This was true regardless of whether the samples with HfC additions were sintered at 1225°C or at 1250°C.

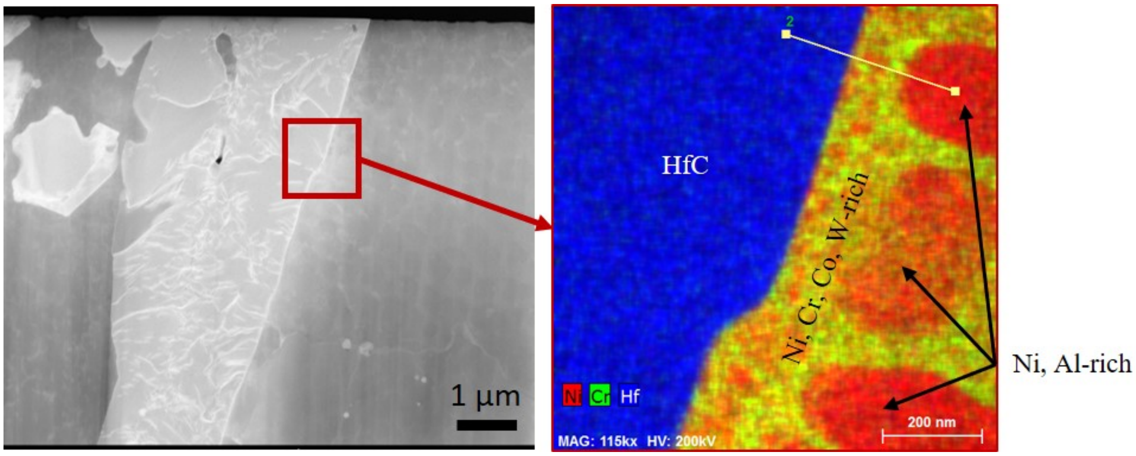

Figure 6.2. Left: scanning transmission electron micrograph of embedded HfC particles in a sintered sample. The sample composition was CM247LC + 3 vol.% HfC, sintered at 45 MPa and 1225°C for 15 minutes. Right: energy-dispersive X-ray spectroscopy image showing the composition at the interface between the HfC particle and Ni-superalloy matrix.

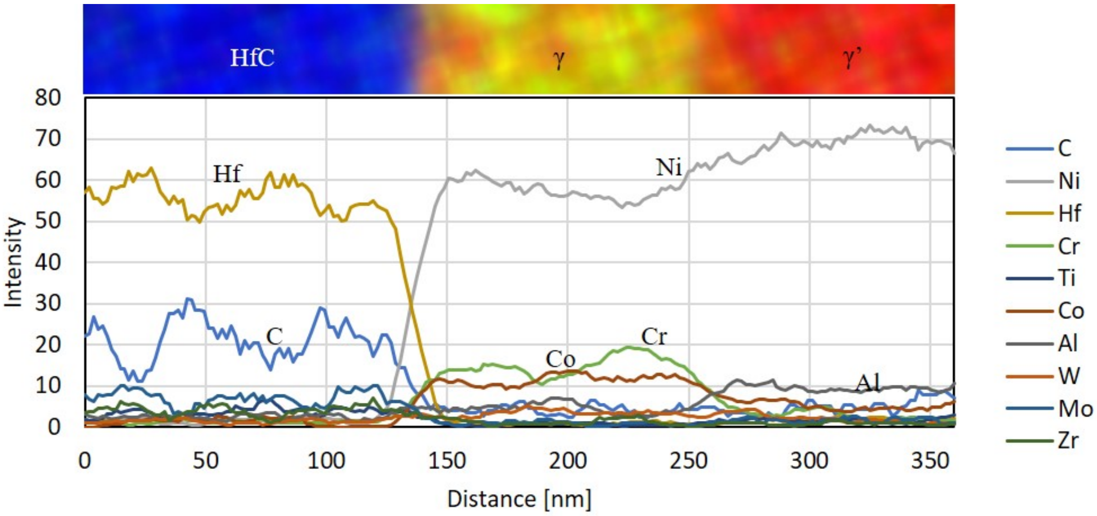

Figure 6.3. EDS Line Scan across interface between HfC particle and CM247LC matrix. Location of the line scan is seen in Figure 6.2.

Although the hardness of the samples increased slightly with increasing HfC additions (see Figure 6.4b), the hardness increase is lower than the expected values; HfC has a higher hardness value (2150 HV) than the pure CM247LC material (433 HV), so an increase in hardness due to the rule of mixtures is expected, but the measured increase in hardness is lower than the predicted values. The lower

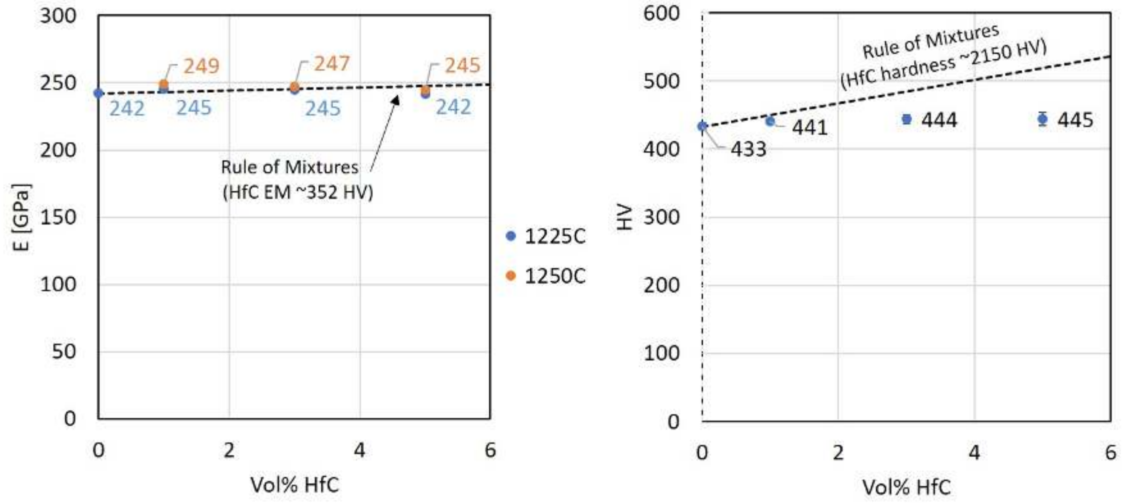

Figure 6.4. Mechanical properties of sintered CM247LC disk with HfC additions. Samples were sintered at 45 MPa for 15 minutes. (a) Elastic modulus vs. composition. (b) Vicker's hardness vs. composition.

hardness values may be due to the distribution of HfC within the sintered material. The HfC particles remained at the grain boundaries during the sintering process. Vicker's hardness data was taken at the center of CM247LC grains, where the HfC additions have less of an effect on material properties, so measured hardness values would be lower than the predicted values. The hardness data shows that far from the grain boundaries, the addition of HfC did not affect the hardness within the grains.

6.2.2 Tensile Testing

To determine the yield and ultimate strengths of the sintered CM247LC material, with and without HfC additions, tensile testing was performed on the sintered samples. The broken tensile specimens are shown in Figure 6.5 while the resulting mechanical properties are summarized in Table 6.1.

At room temperature, the addition of 3 vol.% HfC did not improve the yield strength significantly, with an average increase of 10 MPa. The ultimate tensile strength decreased by approximately 300 MPa , and the elongation was reduced from approximately 15% to 5% as a result of the HfC additions. The HfC additions therefore reduced elasticity and tensile strength at room temperature, although the

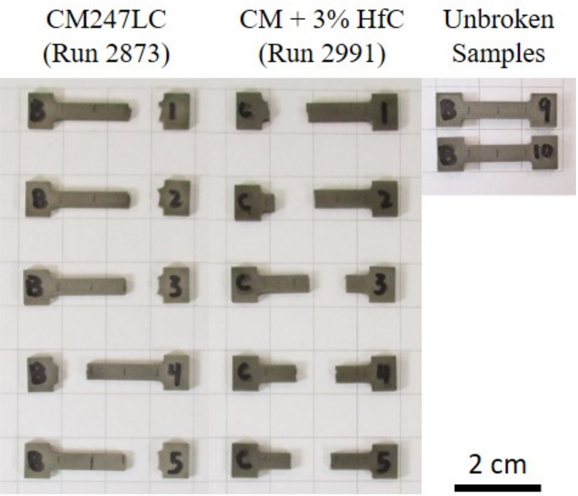

Figure 6.5. Tensile specimens of CM247LC with 0 and 3 vol.% HfC after tensile testing.

Table 6.1. Tensile Properties of CM247LC With And Without HfC

Material	Samples	YS (*MPa*)	UTS (*MPa*)	Stress at Fracture (*MPa*)	Elongation %
CM247LC	8	926 ± 5	1347 ± 35	1325 ± 55	14.8 ± 2.0
CM247LC + 3 vol.% HfC	10	936 ± 8	1036 ± 37	1032 ± 38	5.4 ± 1.4

yield strength was approximately the same as the base CM247LC material. Because grain-boundary sliding is the main deformation mechanism at high temperatures, HfC additions might instead improve mechanical properties at high temperatures, so high-temperature tensile testing is required to determine mechanical properties at service temperatures.

As a result of room-temperature tensile testing, brittle fracture occurred for both materials, with and without HfC additions. The surfaces of broken tensile samples were examined by optical microscopy after polishing, as seen in Figure 6.6. The micrographs show little necking and a jagged fracture surface, which can also be seen in Figure 6.7, which shows a top view of the fracture surfaces. For both materials, clear spherical grains can be seen. Without HfC additions, the fracture occured mainly transgranularly, with smooth cleavage planes showing the fracture of each grain. With HfC additions, fracture occured mainly at the grain boundaries where the HfC presided. This suggests that at room temperature, the HfC acted

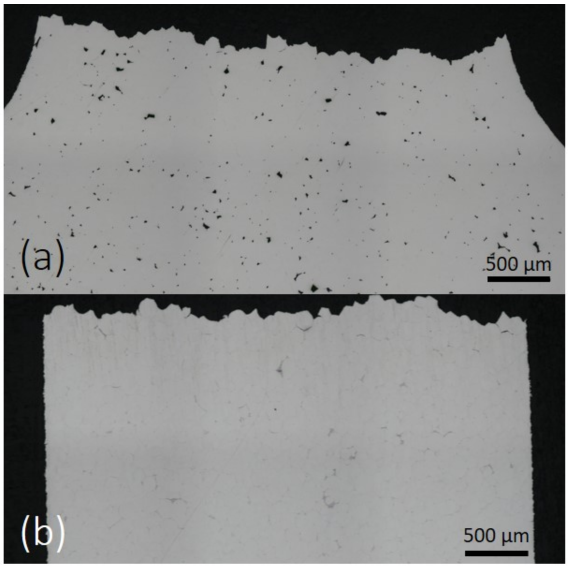

Figure 6.6. Optical micrographs of broken tensile samples, cut from samples sintered at 1250°C and 45 MPa for 15 minutes. Materials are (a) CM247LC and (b) CM247LC with 3 vol.% HfC.

to make the grain boundaries more brittle, causing fracture to travel through the grain broundaries.

6.2.3 Melting Temperature

At room temperature, HfC additions did not improve mechanical properties of the sintered CM247LC powder. To determine whether the HfC additions improved thermal properties, the melting temperature of the sintered materials with various amounts of HfC additions (0, 1, 3, and 5 vol.%) was measured using differential scanning calorimetry (DSC). An increase in melting temperature with HfC additions may suggest that the HfC additions increase the material's thermal stability at high temperatures. A higher thermal stability may allow the material to withstand higher temperature environments, which would potentially improve the efficiency of the turbine engine.

DSC measurements were performed at the Air Force Research Laboratory in Dayton. The resulting melting temperature measurements are shown in Figure 6.8. HfC additions between 0 and 3 vol.% resulted in similar melting temperatures close to 1350°C, with the highest melting temperature corresonding to a 1 vol.% HfC addition, a 13°C increase from the sintered CM247LC powder without HfC

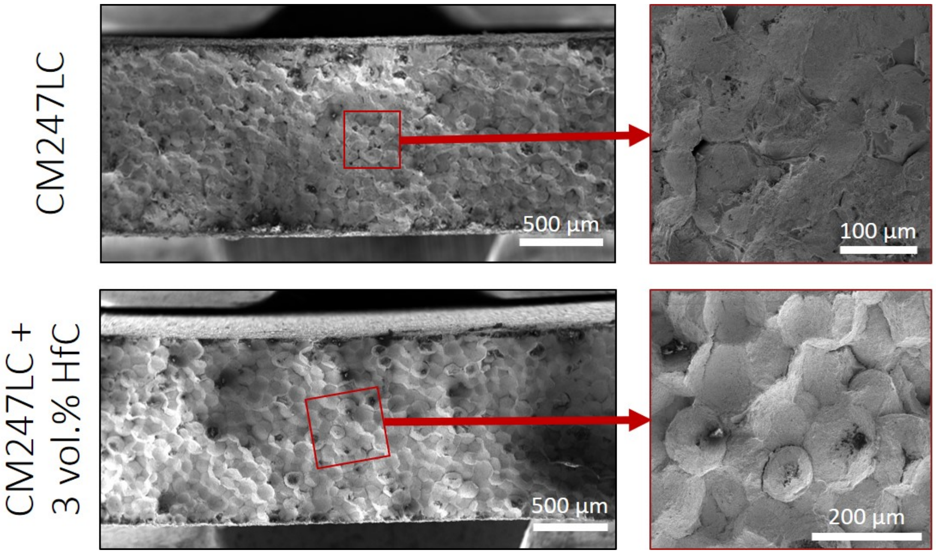

Figure 6.7. SEM micrographs of tensile fracture surfaces. Tensile specimens were cut from sintered CM247LC powder with and without HfC additions, sintered at 1250°C and 45 MPa for 15 minutes.

additions. The addition of 3 vol.% HfC decreased the melting temperature of the pure CM247LC material by 5°C. In contrast, the sample with 5 vol.% of CM247LC exhibited a melting temperature unexpectedly over 100°C lower than the other three samples. The DSC measurement was taken twice to verify the results. As discussed in Section 6.1.2, the interface between the HfC particles and the CM247LC matrix was sharp and free of defects, with no new phase formation. Because the HfC did not diffuse into the CM247LC material or form new phases, the material melting point should be close to the melting point of CM247LC, the lower-temperature material. The difference in melting point may be because of material contamination or measurement error, so new DSC measurements of sintered samples need to be taken to verify these melting temperature measurements. From these preliminary results, it can be surmised that the HfC additions did not improve the melting point of the sintered material.

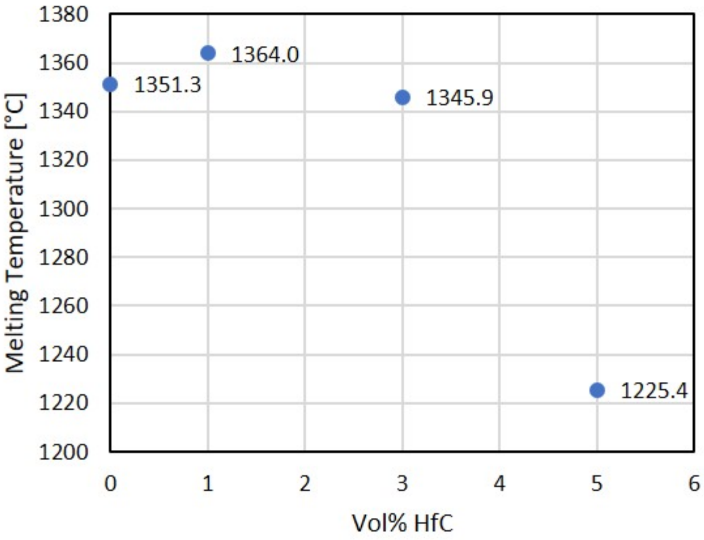

Figure 6.8. Melting temperature of sintered CM247LC with various amounts of HfC.

Chapter 7
Hybrid Turbine Disks Using FAST

Chapter 6 showed that although HfC additions improved the relative density of sintered CM247LC disks, the additions did not significantly improve the mechanical properties of the sintered CM247LC powder. Because the mechanical properties were not improved, pure CM247LC powder without HfC additions was chosen as the rim material of hybrid disks manufactured using FAST. This chapter discusses the mechanical properties and microstructure of hybrid Ni-based superalloy disks manufactured using FAST.

Hybrid disks were formed using an Inconel 718 plate as the core material and CM247LC powder as the rim material, as described in Section 4.2.4. Disks of 70 mm diameter were produced with joining angles of either 0° and 45°, and the bond strength between the sintered CM247LC rim and the solid Inconel 718 core was analyzed using room-temperature tensile testing.

7.1 Porosity and Defects

Two hybrid disks after grinding down both faces are seen in Figure 7.1. Some porosity still remained in the sintered rim of the hybrid disks, with an average rim relative density of 98.4%, measured using Archimedes' method.

X-ray topography was performed to detect any large defects at the joining surface of the disks. The hybrid disk with a 45° joining angle showed no detected joining defects. In contrast, at some cross-sections, the hybrid disk with a 0° joining angle showed lack of interface bonding at multiple locations. It is possible that

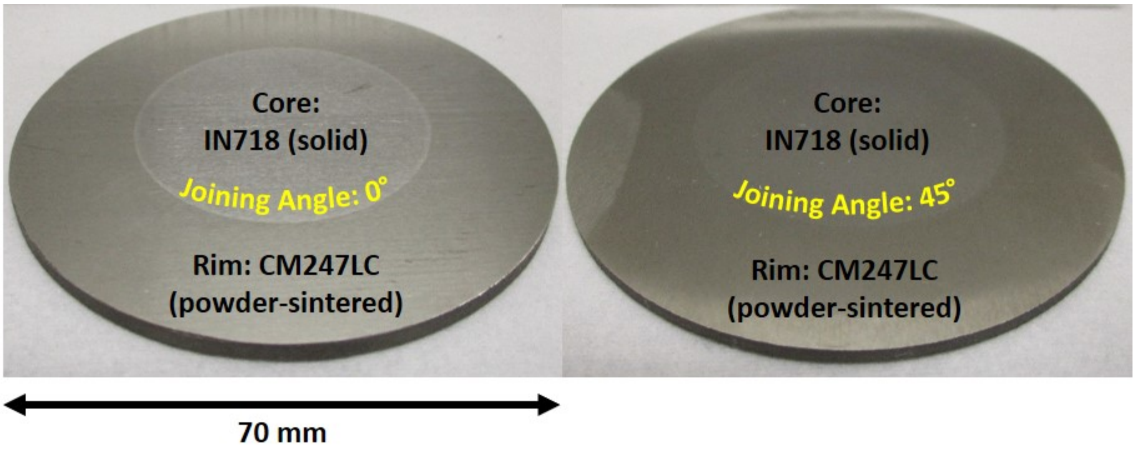

Figure 7.1. Joined subscale hybrid disks of two different joining angles, ground down on both sides after joining using FAST.

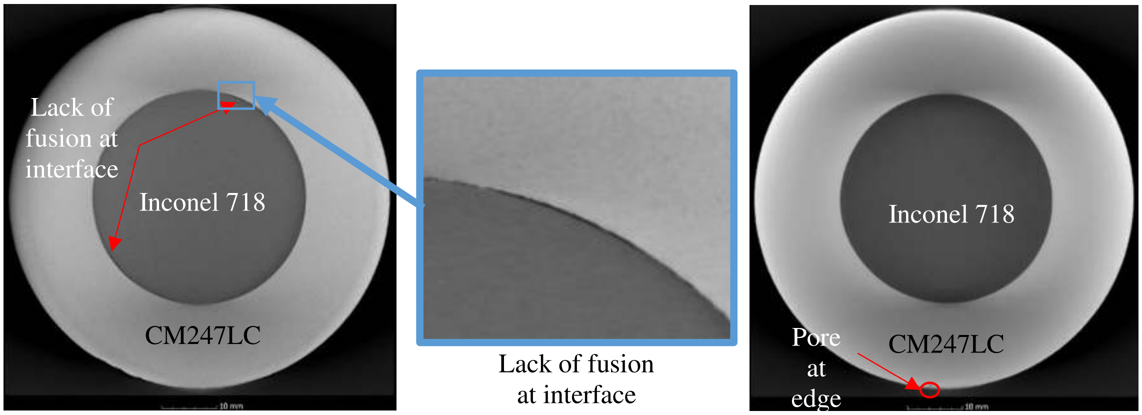

Figure 7.2. X-ray topography image of subscale hybrid disks. Left: hybrid disk with a 0 dgree joining angle. Right: hybrid disk with a 45 degree joining angle.

because pressure was applied perpendicular to the joining surface, the expansion of the powder dering joining did not provide enough pressure for good bonding.

Meanwhile, no porosity was observed at the interface of the two materials, as seen in Figure 7.3. At the cross-sections observed through optical microscopy, no gaps were seen between the two materials, showing that the materials deformed during the joining process, allowing the porosity to migrate away from the interface. Some oxide formation was seen at the interface that may be associated with an oxide layer at the surface of the powder particles. This oxide layer is difficult to remove, as the powder material comes in contact with air during the material and die preparation before joining using FAST.

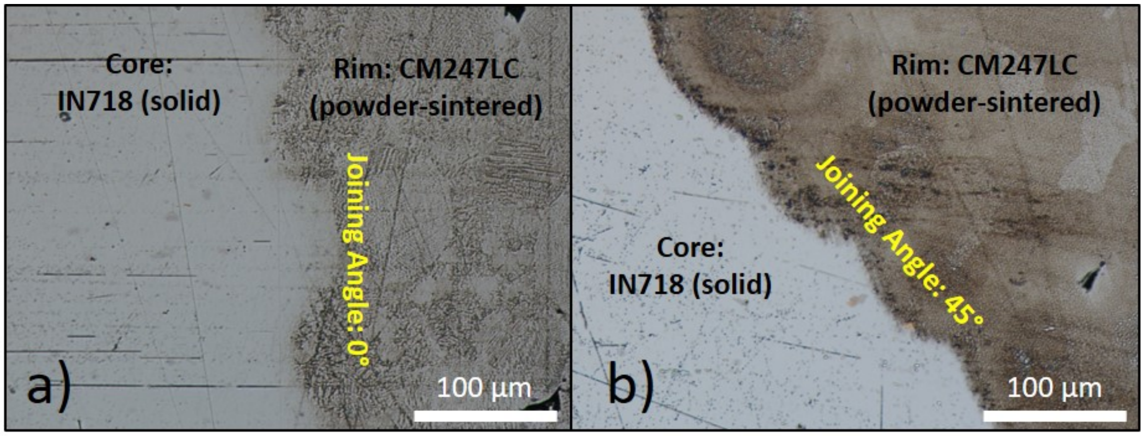

Figure 7.3. Optical micrographs of joined subscale hybrid disks. (a) Disk with 0° interface, joined at 45 MPa and 1225°C for 20 minutes. (b) Disk with 45° interface, joined at 45 MPa and 1225°C for 15 minutes.

7.2 Elastic Modulus and Hardness

The elastic modulus and hardness of the two hybrid disk components were measured and compared to that of the parent materials. The parent material corresponding to the hybrid disk rim is a single-material powder-sintered CM247LC disk with the diameter of 80 mm, and the parent material corresponding to the hybrid disk core is a solid forged Inconel 718 plate. To reproduce the process the hybrid disk core undergoes during the hybrid disk joining process, the Inconel 718 plate was heat-treated using the FAST process at 45 MPa and 1225°C for 15 minutes.

The elastic modulus of both the sintered rim and the Inconel 718 core as measured via the acoustic sound velocity method did not differ significantly between the two joining angles, but the values were higher than those of the parent materials. The measured elastic modulus of the as-received Inconel 718 plate was 193 GPa while the FAST-heat-treated (FHT) Inconel 718 plate resulted in a slightly higher elastic modulus of 210 GPa. The increase in elastic modulus values can be attributed to phase changes within the material due to the FAST process. The CM247LC disk sintered using the same properties resulted in a similar elastic modulus of 205 GPa. The measured elastic modulus values in one of the 0° hybrid disks were close to those of the parent materials, as seen in Figure 7.4, but the other three disks measured show higher elastic moduli than the parent materials. This may be because the hybrid disks were thinner than the parent materials, resulting in a higher heating rate

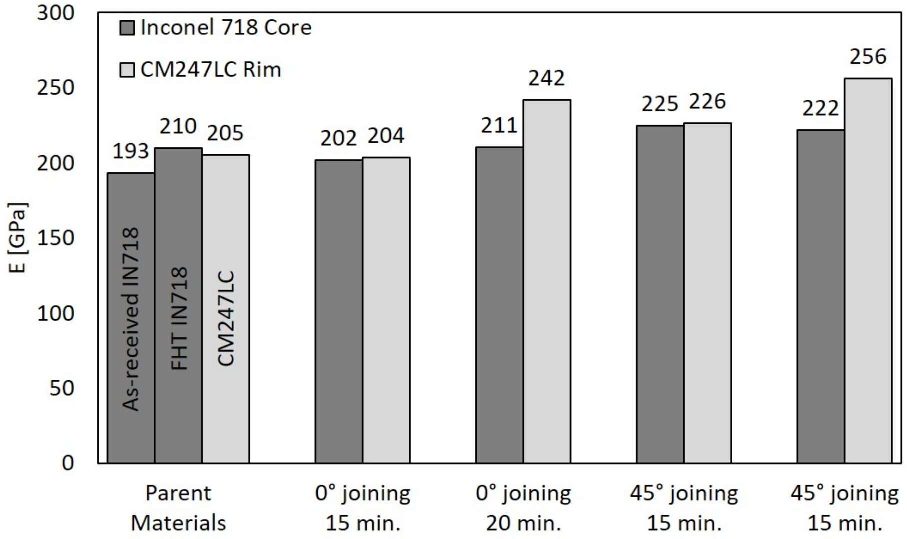

Figure 7.4. Elastic modulus of subscale hybrid disks sintered at 45 MPa and 1225°C.

during the sintering process that affected the decomposition of the γ" precipitates in the Inconel 718 core and the coarsening of the γ' precipitates in the CM247LC rim, therefore affecting the elastic modulus. γ", the main strengthening agent in Inconel 718, is known to decompose at temperatures above 650°C [56]. However, the difference from the parent materials may also result from inconsistencies in the elastic modulus measurement process. Optical micrographs showed that some of the hybrid disks exhibited some porosity in the rim material; the porosity as well as the thinner material may have skewed the sound velocity measurements. More studies are needed to further understand the difference in elastic moduli.

The Vicker's hardness of the hybrid disks across the interface in the hybrid disks as seen in Figure 7.5 shows a sharp transition between the two materials, and hardness values are comparable to that of the parent materials. Based on the measured Vicker's hardness of the parent materials, the FAST heat treatment reduces the Inconel 718 plate's Vicker's hardness from 225 HV to 173 HV. This softening may be attributed to grain growth and phase changes during the FAST process. The powder-sintered CM247LC disk resulted in a higher hardness of 427 HV. The measured hardness of the core and rim of the hybrid disks should correlate with that of the parent materials.

The hybrid disk with a 45° joining angle showed a slightly higher hardness (427 HV) than the hybrid disk with a 0° joining angle (417 HV) in the powder-sintered

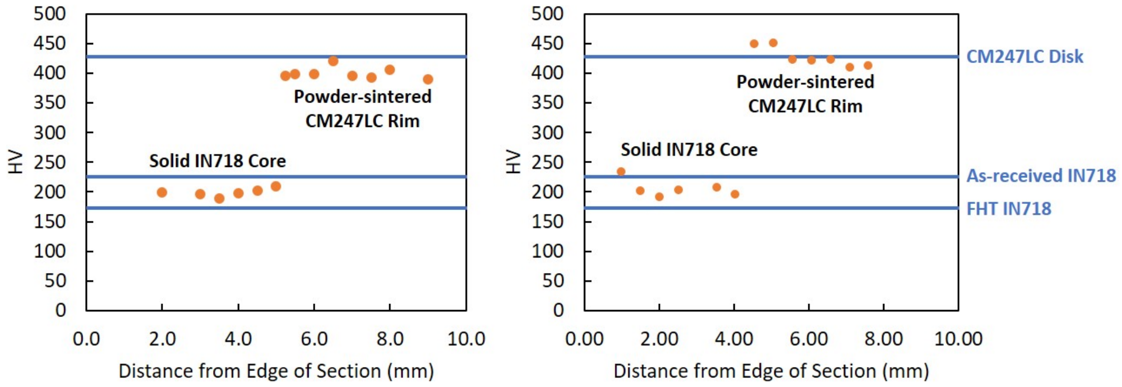

Figure 7.5. Vicker's hardness values of hybrid disks. Left: hardness values of hybrid disk with 0 degree interface. Disk joined at 45 MPa and 1225°C for 20 minutes. Right: hardness values of hybrid disk with 45 degree interface. Disk joined at 45 MPa and 1225°C for 15 minutes.

CM247LC rim. This may be because the hybrid disk with a 0° evaluated was heat treated for 20 minutes compared to the 15 minutes of the hybrid disk with a 45° joining angle, allowing for greater grain growth and coarsening of the γ' precipitates in the rim material, therefore softening the material. For both joining angles, the measured Inconel 718 core hardness was slightly higher (185 HV and 206 HV for the 0° and 45° interface, respectively) compared to the FHT Inconel 718 plate (173 HV). The difference in hardness values can be attributed to the same cause for the elastic modulus difference; the thickness of the hybrid disks was thinner than the FHT Inconel 718 plate, resulting in a higher heating rate that affected the decomposition rate of the γ" precipitates in the Inconel 718 core.

Generally, the elastic modulus and hardness values of the hybrid disk materials corresponded satisfactorily with the parent materials, and differences can be attributed to porosity in the sintered samples, differences in processing times, and slight differences in heating rate due to thickness variations.

7.3 Tensile Testing

To determine the strength of the material bond, room-temperature tensile testing was performed on the hybrid disks and the parent materials. Tensile testing data is summarized in Table 7.1.

The FAST heat treatment reduced the yield strength and ultimate tensile

Table 7.1. Tensile Properties of Hybrid Disks and Parent Materials

Material	Samples	YS (*MPa*)	UTS (*MPa*)	Stress at Fracture (*MPa*)	Elongation %
IN718 Plate (as-received)	6	467 ± 2	868 ± 4	741 ± 8	49.7 ± 1.9
IN718 Plate (FHT)	10	240 ± 4	554 ± 8	466 ± 21	57.1 ± 4.4
Hybrid Disk 45° join	5	348 ± 6	615 ± 41	439 ± 103	15.7 ± 4.2
Hybrid Disk 0° join	5	343 ± 6	557 ± 67	482 ± 145	13.4 ± 4.8

strength of the Inconel 718 plate while increasing the elongation at fracture. The FAST process therefore weakened the material, possibly through the decomposition of γ" precipitates, while increasing ductility.

The bond strength of the hybrid disks was similar to the weaker parent material; the hybrid disks' yield strengths and ultimate tensile strengths did not differ significantly from that of the FHT Inconel plate, which had a tensile strength of 554±8 MPa. On the other hand, the elongation of the hybrid disk tensile specimens was approximately equal to that of the more brittle CM247LC material, approximately a 15% elongation. The tensile properties of the parent powder-sintered CM247LC disk is listed in Table 6.1. Therefore, the weaker Inconel 718 material limited the strength of the hybrid disks while the less ductile CM247LC material limited the ductility of the hybrid disks.

In Figure 7.6, the difference in the fracture locations for the parent materials and the hybrid disks is shown. The as-received Inconel 718 plate and the FHT Inconel plate showed fracture at random locations within the parallel section of the tensile specimens. In contrast, the tensile specimens made from the hybrid disks fractured at or near the interface of the materials, near the center of the parallel section. This suggests that interface effects dominate during the fracture of the hybrid disk tensile specimens. Processing parameters need to be modified to improve the interface strength. However, because the tensile strengths of the hybrid disks and the FHT Inconel 718 plate are similar, a higher-strength core material may be needed in order to improve processing parameters.

A closer look at the fracture surfaces shows the effect of the interface on the fracture of the hybrid disks. First, fracture surfaces of the parent materials need to be inspected. The powder-sintered CM247LC disk fracture surfaces were discussed

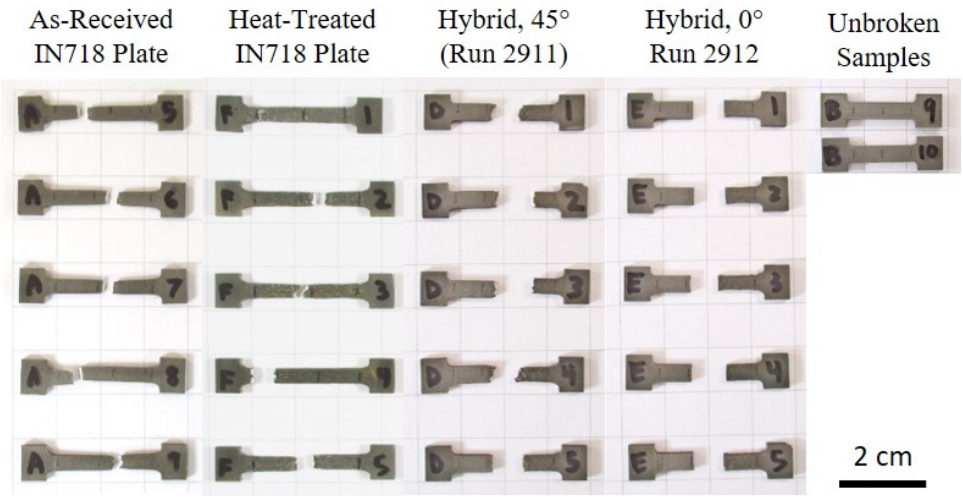

Figure 7.6. Tensile specimens after tensile testing.

in Chapter 6. The fracture of the CM247LC material is brittle, with smooth cleavage planes revealed at the fracture of each spherical grain, as seen in 6.7a. Looking at the surface of the tensile samples, perpendicular to the fracture as seen in Figure 7.7, the fracture of the Inconel 718 material is ductile, with significant necking near the fracture. The FAST heat treatment increased the amount of necking during tensile testing, and the fracture of the FHT Inconel 718 is more rough, caused by the extensive plastic deformation during fracture. As seen in the fractographs in Figure 7.8, both the as-received and FHT Inconel 718 mainly showed microvoid coelescence, a fracture mode associated with ductile transgranular fracture. The large voids in the as-received Inconel 718 material show the existance of intergranular fracture while the fracture was mainly transgranular. The FHT Inconel 718 fracture surface showed larger dimples and more transgranular fracture, confirming that the FAST heat treatment increased the ductility of the material. Because of the clear difference in fracture mode of the CM247LC material and the Inconel 718 material, the fracture surfaces of the hybrid disks can show the fracture locations with respect to the material interface.

Optical images of the 45° hybrid disk broken tensile specimens show that although the fracture occurred near the interface, the fracture occurred mostly in the weaker Inconel 718 material. Optical images and the surfaces' corresponding locations on the tensile samples are shown in Figure 7.9. On one side of the sample, as seen in Figure 7.9a, the fracture clearly appeared completely within the Inconel

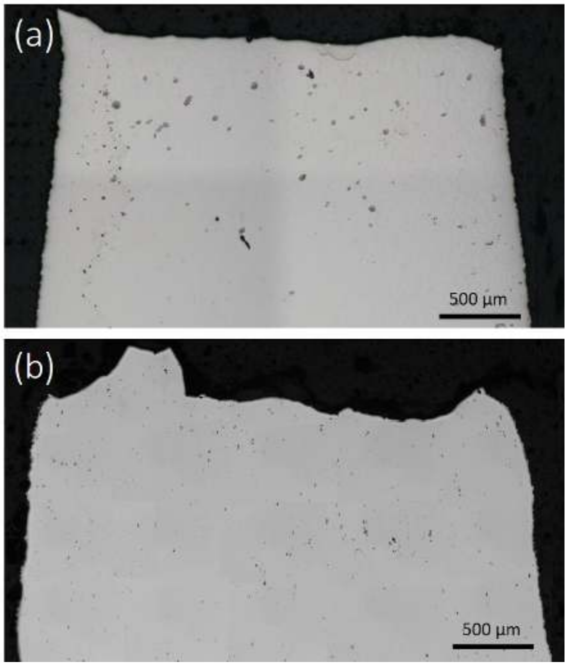

Figure 7.7. Optical micrographs of broken tensile samples, cut from Inconel 718 plate. Materials are (a) as-received and (b) FAST-heat-treated at 1225°C and 45 MPa for 15 minutes.

718 material, but Figure 7.9b and 7.9c show that the fracture line followed the 45° interface, with the fracture partly occurring at the interface between the two materials. The effects of the interface combined with the effects of the weaker Inconel 718 material led to fracture. The SEM images of the 45° hybrid disk fracture surface in Figure 7.8 also show how one side of the fracture surface is dominated by microvoid coelescence in the Inconel 718 material while the other side is dominated by brittle fracture at the material interface. At the top of fracture surface image, the surface begins to show smooth cleavage planes indicative of the CM247LC material fracture.

In contrast, the fracture surface of the 0° hybrid disk showed fracture along the interface of the two materials. As shown in Figure 7.10, the fracture cleanly divides the Inconel 718 material from the CM247LC material. Significant porosity is seen within the CM247LC material, perhaps contributing to the propogation of the fracture along the interface. Note that during the joining process, the Inconel 718 material deformed to accomodate the CM247LC particles at the interface while the spherical CM247LC particles did not deform significantly. This is a result of the materials' difference in ductility and strength.

The SEM images of the 0° hybrid disk fracture surface in Figure 7.8 show that the fracture occurred at the interface. The spherical CM247LC grains are clearly shown, suggesting a brittle fracture similar to that of the CM247LC material with 3 vol.% HfC additions (see Figure 6.7). The addition of HfC made the material more brittle at the grain boundaries, resulting in intergranular fracture. This trend was confirmed by a surface showing the spherical structure of the CM247LC powder. In comparison, the fracture surface of the parent CM247LC material without hafnium carbide as seen in Figure 6.7 showed more diffusion between the CM247LC particles at the surface as well as more transgranular fracture. Because the 0° hybrid disk rim material did not include HfC additions, if the fracture occurred within the CM247LC material, the fracture surface should also show diffusion between the CM247LC particles and transgranular fracture. However, the hybrid disk fracture surface showed intergranular fracture and spherical CM247LC grains, so the fracture did not occur within the CM247LC material but instead at the interface between the CM247LC material and the Inconel 718 material. Thus, the fracture was dominated by the material interface effects.

In summary, because the fracture of the hybrid disk tensile specimens occurred at or near the interface, interface effects (in combination with the effects of the weaker Inconel 718 material for the 45° hybrid disks) dominated the fracture during tensile testing. The angle of the interface did not significantly affect the numerical tensile properties, although the fracture mode was affected. Looking at the tensile properties listed in Table 7.1, the strength of the interface is approximately equal to the strength of the weaker material. This may be the reason behind the different fracture mode for the two joining angles; a slight difference between the two hybrid disks may be the difference between interface fracture and fracture within the Inconel 718 material. The porosity in the 0° hybrid disk tensile specimens may have contributed to a weaker interface, while the lack of porosity in the 45° hybrid disk tensile specimens may be a result of more optimal processing parameters, leading to a slightly stronger interface. These results are promising; by optimizing process parameters using FAST, it is possible to strengthen the bond between the two dissimilar superalloys. However, a material of higher strength than Inconel 718 may be needed to further optimize the process parameters.

7.4 Scaled-up Manufacturing of Hybrid Disks

To determine the scalability of the hybrid disk manufacturing process, a larger-scale (200 mm diameter) hybrid disk with a sintered CM247LC powder rim and a solid Inconel 718 core was produced using FAST, with a similar die assembly and joining process as the subsize 70-mm-diameter disks. The disk had a 0° interface between the rim and core materials, and the two materials were joined at 1275°C at a pressure of 45 MPa for 30 minutes. The resulting disk, ground down on both sides, is seen in Figure 7.11. At one face of the disk, some portions of the material interface showed a lack of bonding, though no major defects were seen on the other side of the disk. The same defects were also present in some of the 0° subscale hybrid disks of 70 mm diameter. It can be concluded that scaling up manufacturing of hybrid disks using FAST is possible, but optimization of processing parameters is needed to improve bonding between the rim and core materials.

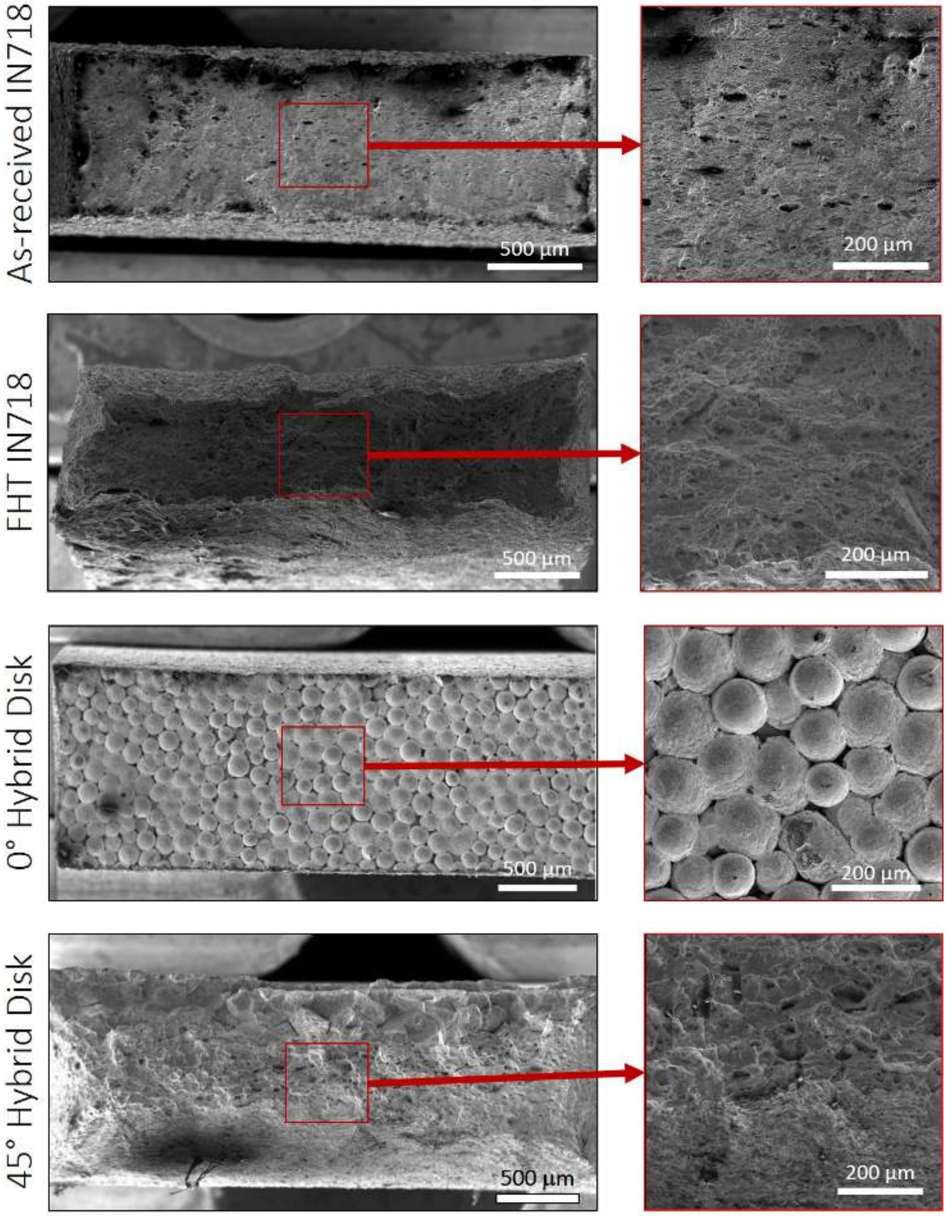

Figure 7.8. SEM images of fracture surfaces of forged Inconel 718 material (as-received and FAST-heat-treated) and hybrid disks (0° and 45° interface).

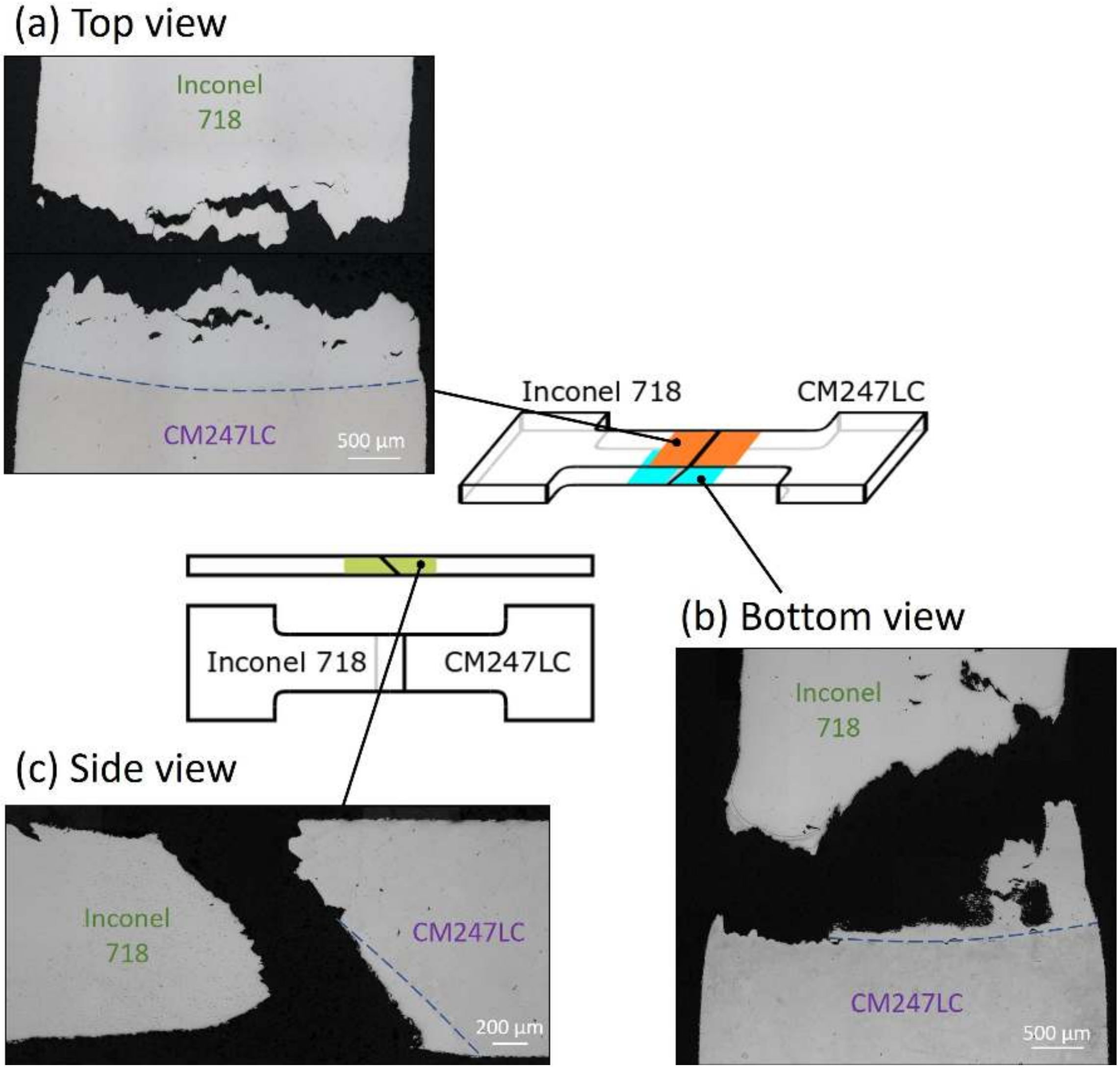

Figure 7.9. Optical micrographs of broken tensile samples, cut from a hybrid disk with a 45° interface. Three separate tensile samples were polished to illustrate three different cross-sections.

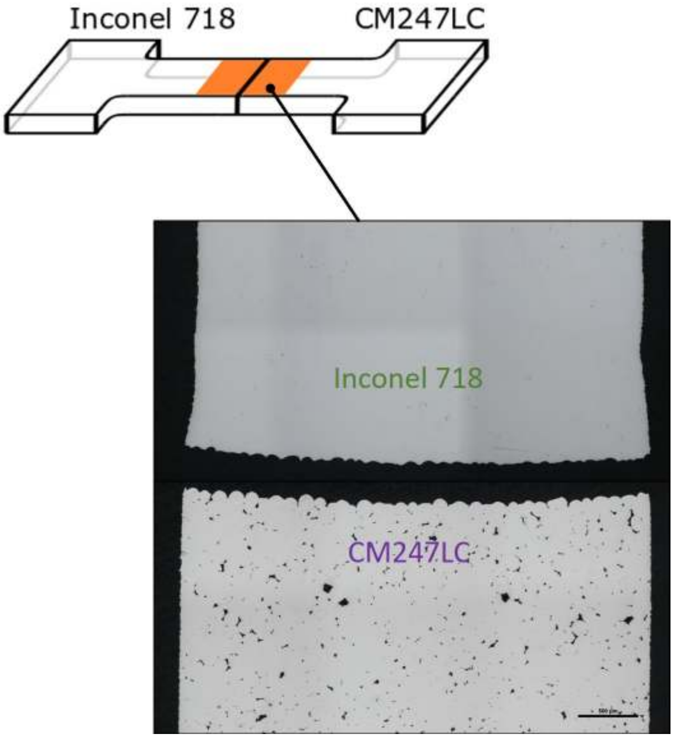

Figure 7.10. Optical micrographs of a broken tensile specimen, cut from a hybrid disk with a 0° interface.

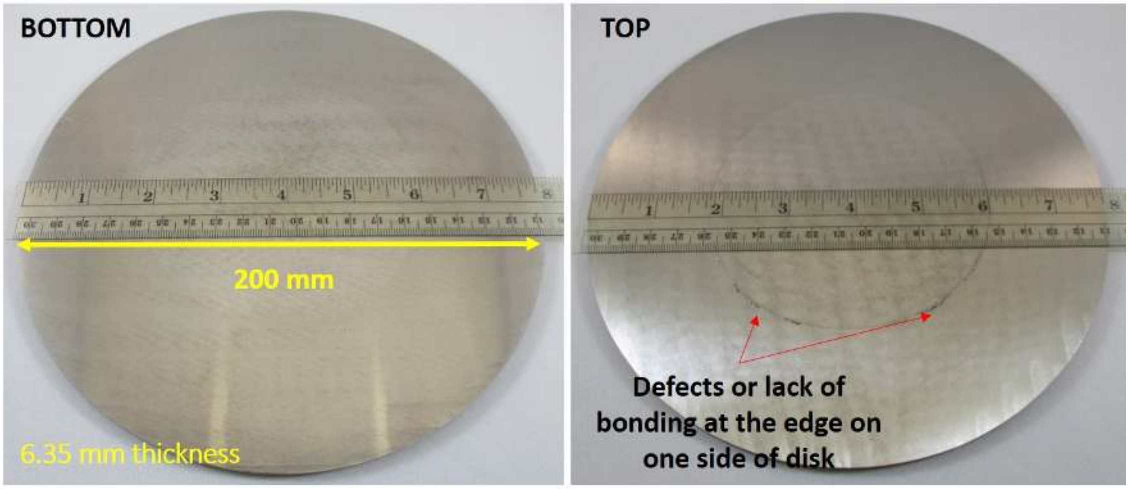

Figure 7.11. Hybrid disk of 200 mm, joined at 1275°C for 30 minutes.

Chapter 8
Summary and Future Work

8.1 Summary and Conclusions

In this thesis, the effect of FAST on sintering and joining Ni-based superalloys was studied via microstructural and mechanical characterization. CM247LC powder with varying amounts of HfC additions were sintered to high relative density (>99%), and hybrid disks with a powder-sintered CM247LC rim and a solid Inconel 718 core were produced.

When studying the effect of FAST processing parameters on the properties of sintered CM247LC powder, an increase in sintering temperature decreased material porosity while increasing grain size. Increased sintering temperature led to a migration of porosity towards the rim of the disks, and a two-step sintering process resulted in nominal density (100%) for disks of 80 mm diameter. During the second part of the hold step, the increase in temperature reduced porosity and increased grain size while the decrease in pressure minimized material flashing.

Hafnium carbide additions to the CM247LC powder before sintering did not significantly improve room-temperature mechanical properties. The HfC additions remained at the grain boundaries and were not diffused into the CM247LC grains, as shown by the short interface distance between the HfC and the CM247LC domains (<30 nm). The HfC additions also did not improve thermal properties; the addition of 1 vol% of HfC to the CM247LC powder before sintering improved the melting temperature by 13°C, but greater additions decreased the melting temperature (5°C with 3 vol% HfC and 126°C with 5 vol% HfC). Further DSC measurements are needed to verify these temperature measurements. Although the addition of HfC did not improve mechanical or thermal properties, the addition of HfC reduced porosity. One possible reason for the reduction in porosity is the greater surface area due to the finer HfC particles, allowing the HfC to fill in the gaps between the CM247LC particles. A second hypothesis is that the HfC slowed the diffusion of the CM247LC powder at the powder surfaces in a grain-growth-inhibiting effect, allowing porosity to migrate out of the material without trapping large pores within the material. Because HfC additions did not improve room-temperature mechanical properties, HfC was not included during the manufacturing of hybrid disks.

Hybrid disks were manufactured using FAST with pure CM247LC powder as the rim material and a solid forged Inconel 718 plate as the core material, resulting in hardness and elastic modulus values comparable to that of the parent materials, with bonding strength similar to that of the weaker Inconel 718 reference plate. The two different bonding angles between the powder-sintered rim and the solid core led to a disparity in the fracture location during room-temperature tensile testing; hybrid disks with a 45° bonding angle resulted in fracture near the interface, mainly within the weaker Inconel 718 material, while disks with a 0° angle resulted in fracture at the interface. Because fracture occurred at or near the interface for both joining angles, the interface bonding needs improvement. Processing parameters also need to be optimized to reduce porosity in the powder-sintered rim. The joining of the 45° hybrid disk resulted in better bonding and less porosity, possibly because the 45° angle allowed for more direct pressure to consolidate the two materials during the joining process.

In conclusion, this thesis studied the FAST capability of joining two dissimilar Ni-based superalloy materials in hybrid disks via solid state joining. Hybrid disks were formed with a solid Inconel 718 core and a powder-sintered CM247LC rim without a heat affected zone, and the bonding strength between the two materials was similar to that of the weaker Inconel 718 material. No previous method successfully formed hybrid Ni-based superalloy disks without high residual stresses and localized melting at the interface. More research is needed to optimize processing parameters for improved interface bonding and decreased porosity in the hybrid disks.

8.2 Future Work

To improve the interface properties of FAST-joined hybrid disks and to further understand the effects of FAST processing on their component mechanical properties, future work includes optimization of processing parameters, scaled-up manufacturing of hybrid Ni-superalloy components, joining of both polycrystalline and single-crystal Ni-superalloy materials, and high-temperature mechanical testing of the scaled-up components.

The objective of processing parameter optimization is to manufacture hybrid disks with zero porosity within the powder-sintered rim, no interface defects, and a bond strength equivalent to that of the weaker parent material. Because the tensile strength of the material interface in the subscale hybrid disks was similar to that of the weaker Inconel 718 material in this thesis, optimization of the joining process may require a higher-strength core material. Possible changes to processing parameters include longer sintering times, higher sintering temperatures, and changes in die and disk geometries. Increasing sintering pressure is not preferred, as scaled-up manufacturing of hybrid disks would require larger pressing forces, so the maximum pressing force of the FAST machine would limit the maximum diameter of the hybrid disks. Instead, longer sintering times and higher sintering temperatures may improve interface contact and also lead to greater diffusion between powder particles. A greater disk thickness may also improve the interface, as discrepancies in powder thickness throughout the rim would be less significant, resulting in a more evenly distributed pressure throughout the rim during sintering. The joining angle of the disk can also be modified; a 45° interface resulted in a stronger bond than the 0° interface, so a 45° interface may be more effective during larger-scale manufacturing of hybrid disks. Different joining angles may also be studied. To mitigate the weakening effect of FAST on the solid core material, post-joining heat treatments may also be explored.

Because turbine blades are composed of single-crystal Ni-based superalloys, optimization of processing parameters may also be performed to join polycrystalline materials to single crystal materials as well as single crystal materials to single crystal materials. The ability to join single crystal materials in the hybrid disk would improve the potential strength and temperature capabilities of the hybrid disk rim. Single crystal materials are are formed through a directional solidification process, so it would not be possible sinter superalloy powder to form a single crystal component using FAST. Therefore, solid directionally-solidified single crystal material would need to be used. The surface finish of the single crystal material may play a large role in the bonding characteristics of hybrid materials, so joining of single crystal to polycrystalline materials and single crystal to single crystal materials may result in difficulties in minimizing defects at the interface. The uniform crystalline orientation of single crystal materials may also result in more complex interface formation.

After optimization of processing parameters, scaled-up manufacturing of hybrid Ni-based superalloy components is needed to determine scalability of the FAST process. A preliminary study showed that scaling up the manufacturing of hybrid disks using FAST is possible, but optimization of processing parameters is required to improve interface properties between the rim and core materials of the scaled-up hybrid disks. Further scaling studies are needed to produce disk geometries compatible with current turbine engines; current turbine disks are several centimeters in thickness.

Finally, high temperature mechanical testing on the scaled-up hybrid components needs to be performed, including high-temperature tensile testing and bend testing. Understanding the high temperature properties of FAST-joined Ni-based superalloy disks is necessary to determine the capabilities of FAST-joined hybrid turbine disks under operating conditions.

Appendix A
Elastic Modulus and Hardness

A.1 Introduction

Elastic modulus is generally an intrinsic material property related to atomic bonding while hardness is an engineering property dependent on the material heat treatments. Because hardness changes with heat treatment while elastic modulus does not, the theoretical relationship between the two properties is not well understood. The two properties do not necessary correlate, but generally, a higher hardness leads to a higher elastic modulus.

A.2 Study of Relationship using Vicker's Indentation

One study by Bao, Wang, and Zhou investigated the relationship between elastic modulus and hardness of Ti_3SiC_2, using the mechanics of the Vicker's indentation process to determine a theoretical relationship [57]. The result was the following relationship:

$$E_r = D\sqrt{HR_s}, \tag{A.1}$$

where E_r is the reduced modulus (based on the elasticity of the material and the indenter), D is a constant based on indenter geometry, H is the hardness, and R_s is the recovery resistance, a material property.

If the indenter geometry is kept constant and if recovery resistance is assumed

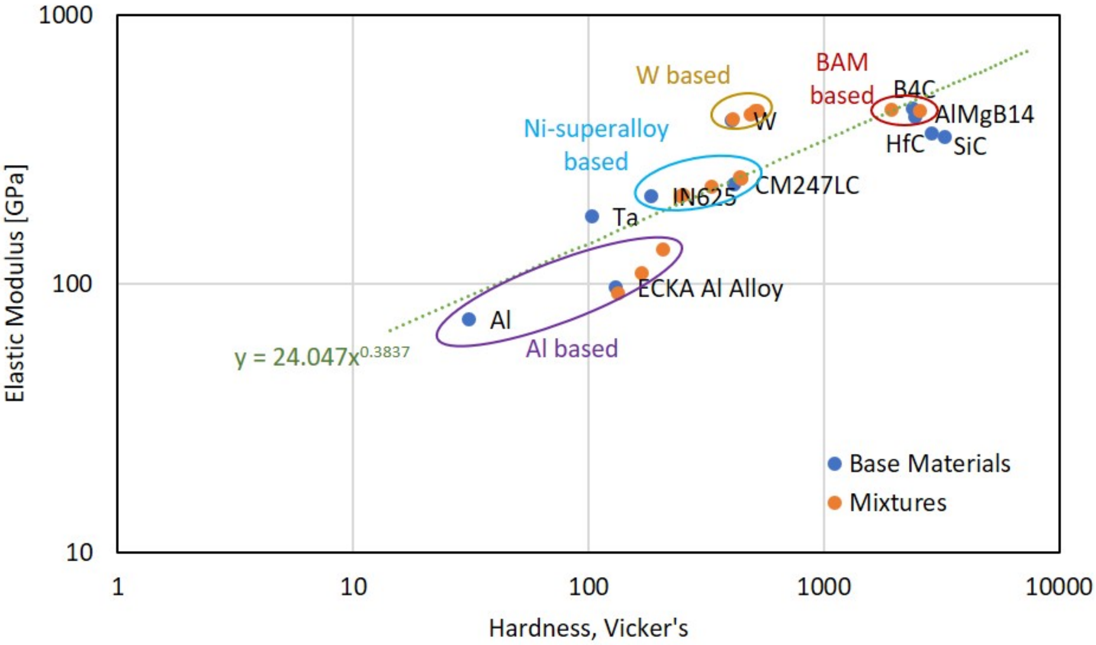

Figure A.1. Elastic Modulus vs. Vicker's Hardness of various materials sintered using FAST, as measured at Penn State Applied Research Laboratory.

to be a function of the heat treatment, materials that undergo the same FAST heat treatment process may therefore have the following relationship between elastic modulus and hardness:

$$E_r \propto H^{1/2}. \tag{A.2}$$

A wide variety of materials have been sintered using the same FAST machine and setup as in the current study, so the materials have therefore gone through similar heat treatments. A plot of the relationship between the two materials is shown in Figure A.1.

As expected, elastic modulus has a positive correlation with hardness. The line of best fit suggests that elastic modulus is proportional to the Vicker's hardness to the power of 0.4, which is close to the power of 0.5 predicted by Bao et al.

More research is needed to better understand the correlation between elastic modulus and hardness.

Appendix B
Silicon Carbide Nanoparticle Additions to Inconel 625

In a preliminary study, various amounts of silicon carbide (SiC) were added to Inconel 625 powder-sintered disks, and mechanical properties of the sintered materials were compared to a forged reference sample.

B.1 Introduction

To determine whether Ni-based superalloy powder can be sintered using field assisted sintering technology (FAST) to high density and with mechanical properties comparable to conventionally-produced materials, the Ni-based superalloy Inconel 625 was sintered at a range of processing parameters. Because previous studies have shown that carbide additions inhibited grain growth and improved mechanical properties in tungsten alloys, as described in Section 2.3, small amounts (0-5 vol.%) of SiC powder were mixed with the Inconel 625 powder before sintering to determine whether the mechanical properties of the sintered material could be improved through carbide additions. The microstructure and mechanical properties of the sintered materials were compared to that of a forged Inconel 625 plate.

B.2 Materials and Sintering Process

Inconel 625 is a nickel-based superalloy with a composition as listed in Table B.1, with a melting temperature between 1290 and 1350°C. SiC is a carbide with a

Table B.1. Composition of Inconel 625

Element	Min %	Max %
Chromium	20.00	23.0
Nickel	58.00	Balance
Molybdenum	8.00	10.00
Cobalt	-	1.00
Columbium + Tantalum	3.15	4.15
Aluminum	-	0.40
Titanium	-	0.40
Carbon	-	0.10
Iron	-	5.00
Manganese	-	0.50
Silicon	-	0.50
Phosphorus	-	0.015
Sulphur	-	0.015

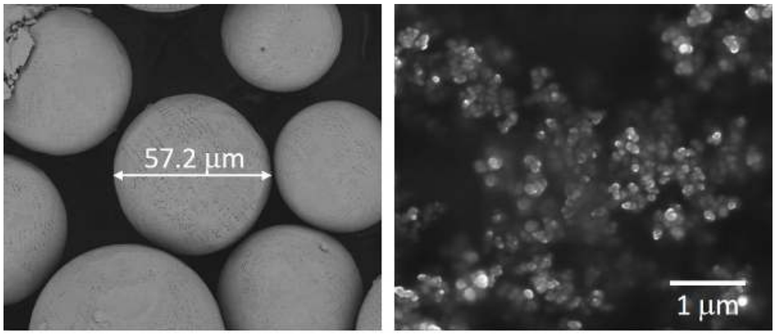

Figure B.1. SEM micrographs of Inconel 625 powder (left) and silicon carbide powder (right).

melting temperature of 2730°C.

The Inconel 625 powder used in this study had a particle size between 44 and 105 µm while the SiC powder had a particle size between 80 and 100 nm, as shown in Figure B.1. Various amounts of SiC powder (0, 1.5, 2.5, and 5 vol.%) were mixed with the Inconel 625 powder using a Resodyn acoustic mixture before sintering. The SiC nanoparticles adhered to the Inconel 625 powder surfaces after mixing, resulting in an approximately even distribution of the SiC particles on the Inconel 625 powder, as seen in Figure B.2.

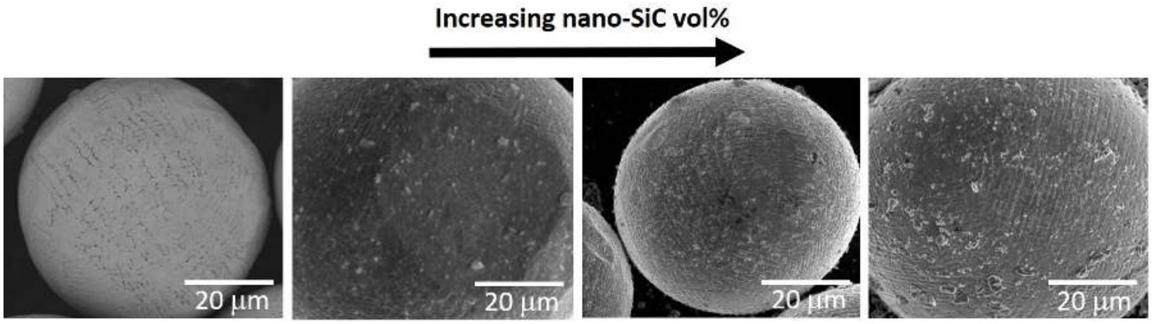

Inconel 625

Inconel 625
+ 1.5 vol% SiC

Inconel 625
+ 2.5 vol% SiC

Inconel 625
+ 5 vol% SiC

Figure B.2. SEM micrographs of Inconel 625 silicon carbide powder mixtures before sintering.

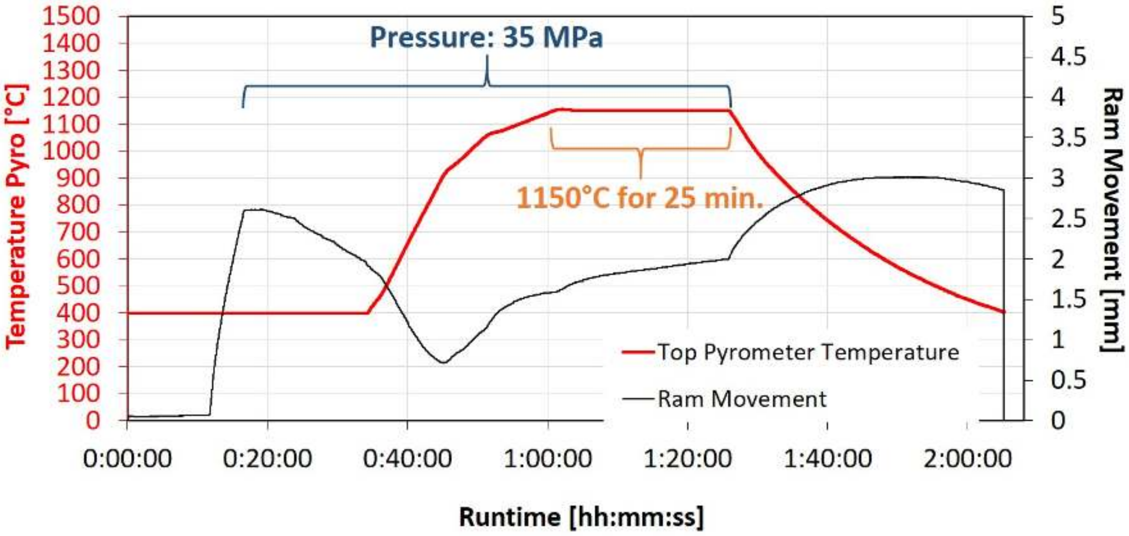

Figure B.3. Temperature and ram movement during the sintering of pure SiC powder.

The powder mixtures were sintered at 1150°C for 25 minutes, resulting in square plates of 101 mm width and 3 mm thickness. The sintering process is similar to that of the sintering process described in Section 4.2.1, with a sample plot of temperature and ram movement (relative distance between top and bottom punches) shown in Figure B.3. The resulting sintered plates and their relative densities are shown in Figure B.4.

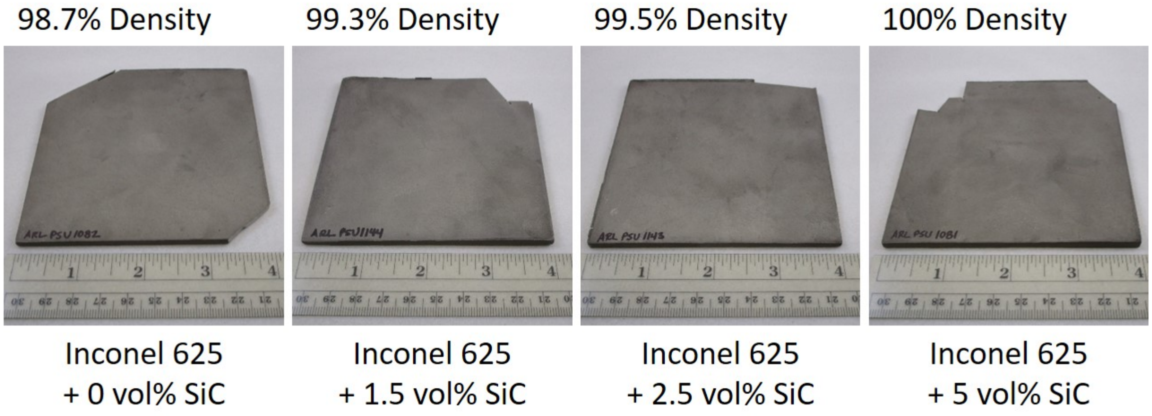
98.7% Density
99.3% Density
99.5% Density
100% Density

Inconel 625 + 0 vol% SiC
Inconel 625 + 1.5 vol% SiC
Inconel 625 + 2.5 vol% SiC
Inconel 625 + 5 vol% SiC

Figure B.4. Powder-sintered Inconel 625 plates with SiC additions.

B.3 Resulting Microstructure

As seen in the cross-sectional microstructure of the sintered materials shown in Figure B.5, the SiC remained the boundaries of the Inconel 625 particles during the sintering process. As a result, spherical grains corresponding to the spherical Inconel 625 particles are surrounded by smaller SiC particles.

A closer look at the grain boundaries as seen in Figure B.6 shows that increased SiC particle additions result in a new dendrite-like phase formation at the grain boundaries. The width of the new phase increases with increased SiC additions. The FAST process itself also resulted in new phase formation, as confirmed with the x-ray diffraction spectrum (see Figure B.7).

Another effect of the SiC additions is an increase in the relative densities of the sintered material. Because the SiC nanoparticles coated the Inconel 625 particles before sintering, the improved density may be due to increased contact area between Inconel 625 particles, leading to increased diffusion and therefore decreased porosity. The new phase formation at the grain boundaries also may have increased diffusion and interaction between Inconel 625 particles.

The new phase formation at the grain boundaries is seen in the trasmission electron micrograph of a grain boundary in Figure B.8. Using a combination of transmission electron microscopy and electron dispersive x-ray spectroscopy, the elemental composition of each phase can be determined. At the grain boundary, a phase rich in silicon and molybdenum was observed. Inconel 625 is approximately

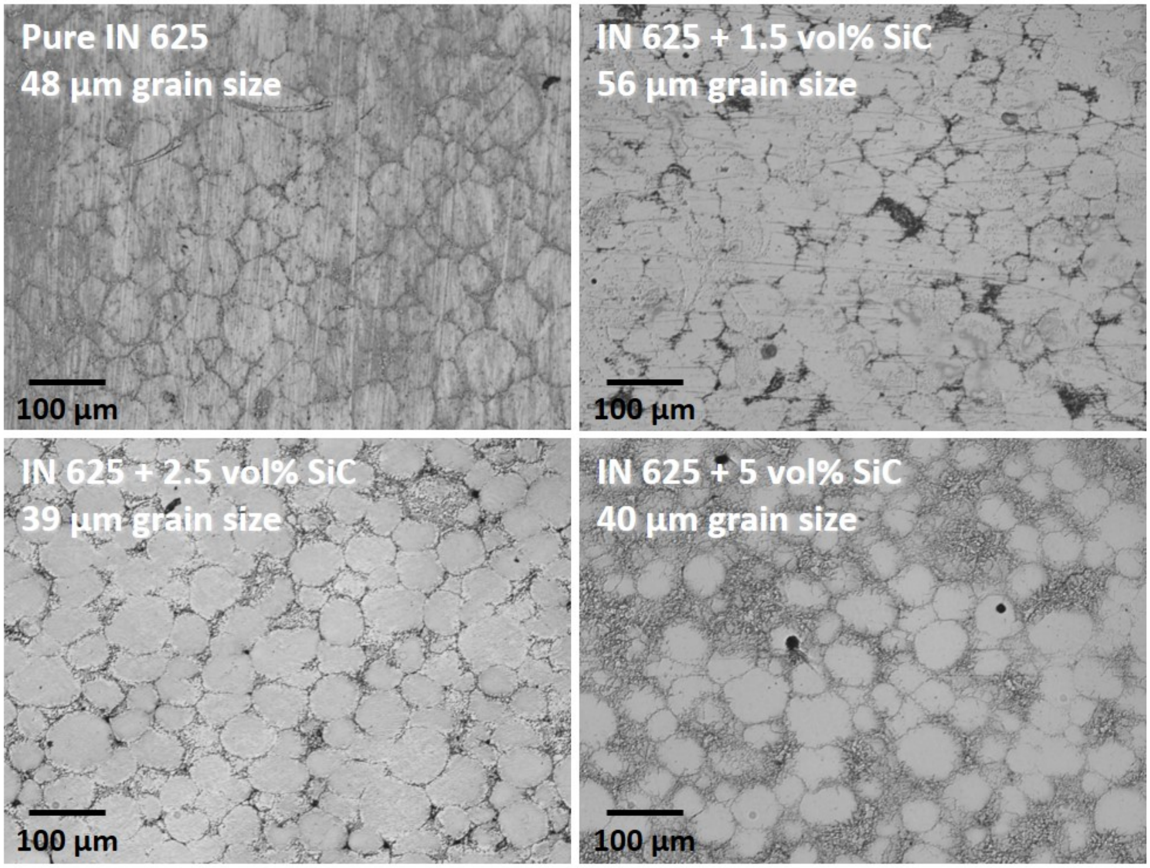

Figure B.5. Optical micrographs of sintered Inconel 625 plates with SiC additions showing grain size.

made of 9 wt.% molybdenum, so this result indicates that the silicon carbide particles diffused into the Inconel 625 particles to form a new phase.

B.4 Resulting Mechanical Properties

Vicker's hardness and elastic modulus measurements were taken to determine the effect of the new phase formations on the mechanical properties of the sintered materials. Elastic modulus was estimated using ultrasonic sound velocity as described in Section 4.3.2.

The expected hardness and elastic modulus values according to the rule of mixtures were determined using known hardness and elastic modulus values of sintered SiC and of hafnium carbide. The upper and lower bounds of the expected

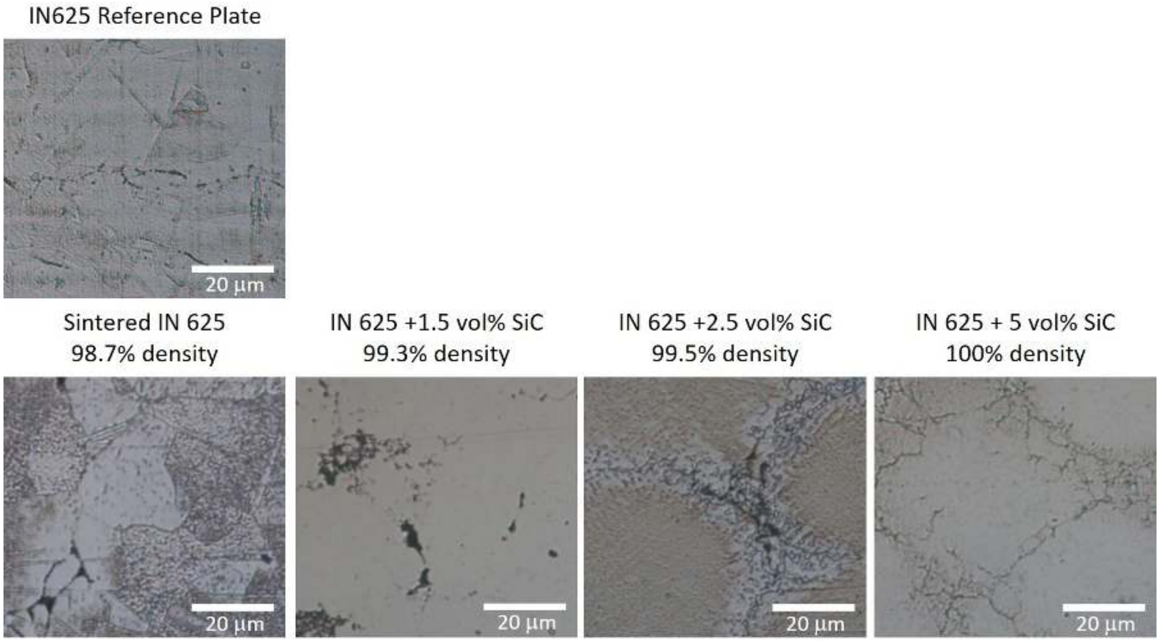
IN625 Reference Plate

Sintered IN 625 98.7% density

IN 625 +1.5 vol% SiC 99.3% density

IN 625 +2.5 vol% SiC 99.5% density

IN 625 + 5 vol% SiC 100% density

Figure B.6. Optical micrographs of sintered Inconel 625 plates with SiC additions.

values are as follows:

$$x_{upper} = V_{SiC} x_{SiC} + (1 - V_{SiC}) x_{IN625}, \tag{B.1}$$

$$x_{lower} = \left(\frac{V_{SiC}}{x_{SiC}} + \frac{1 - V_{SiC}}{x_{IN625}}\right)^{-1}, \tag{B.2}$$

where x is the hardness or elastic modulus value and V_{SiC} is the volume fraction of silicon carbide.

The measured hardness and elastic modulus values compared to the expected values are plotted in Figures B.9 and B.10. The hardness and elastic modulus of pure SiC are taken to be 2800 HV and 436 GPa, respectively.

As expected, the hardness increased with the volume fraction of SiC due to the high hardness of SiC. With 1.5 vol.% of SiC additions or greater, the hardness was comparable to or higher than that of the reference forged Inconel 625 plate. The elastic modulus also increased with the volume fraction of SiC due to the high elastic modulus of SiC. The measured elastic modulus values are higher than the estimated values, possibly because the new phase formation at the grain boundaries may have decreased the ductility of the material. The higher elastic modulus values

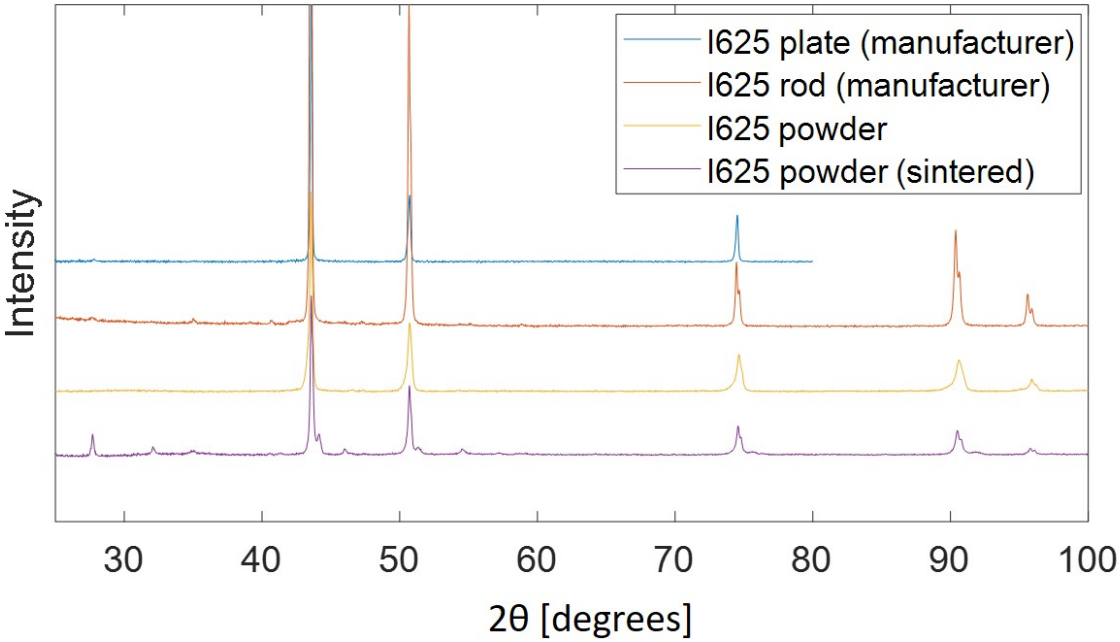

Figure B.7. X-ray diffraction spectrums of forged, powder, and sintered Inconel 625.

may also be due to the small grain sizes of the FAST-sintered material. The elastic modulus values at the center and the corners of the sintered plates were comparable, showing that the sintered material was mostly homogeneous.

B.5 Summary and Discussion

Inconel 625 powder was sintered using FAST to achieve high density and homogeneity, with and without SiC additions. The FAST process resulted in minimal grain growth, and SiC additions remained near the grain boundaries and led to new phase formations at the grain boundaries. The modification of microstructure due to the addition of SiC led to hardness values comparable with that of a reference forged plate while measured elastic modulus values exceeded that of the reference plate.

FAST is able to sinter bulk samples nickel-based superalloy powder to high density, and the formation of new phases at the grain boundaries due to SiC additions did not adversely affect the mechanical properties of the sintered material.

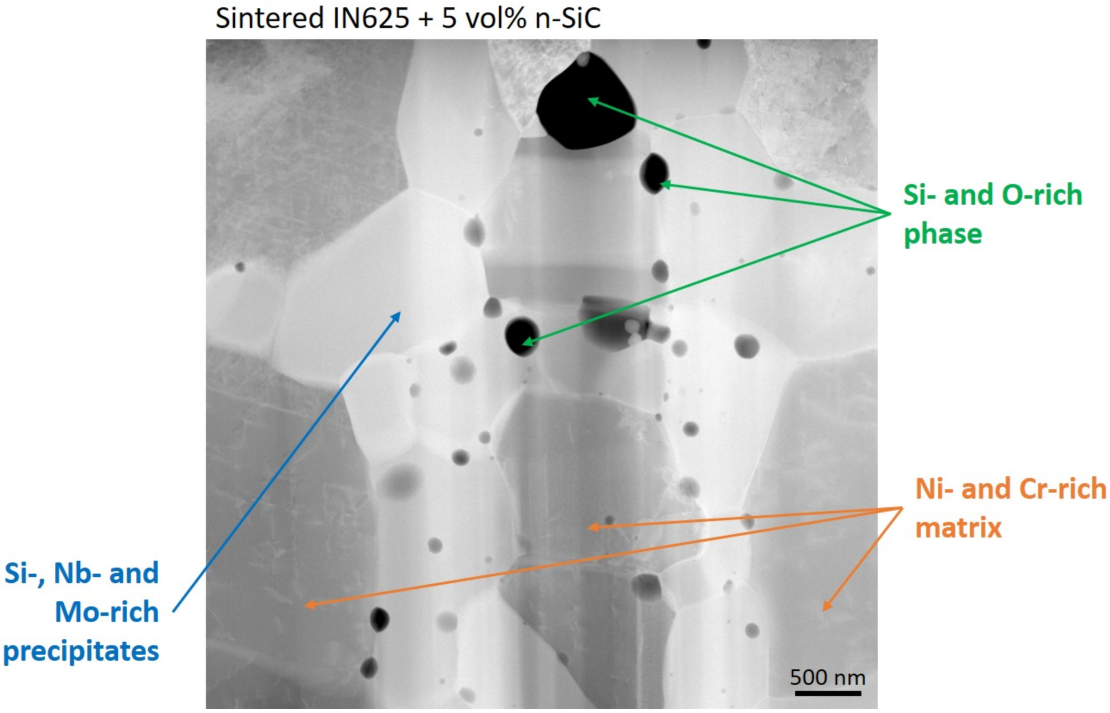

Figure B.8. Scanning transmission electron micograph of grain boundary of sintered Inconel 625 with 5 vol.% SiC additions.

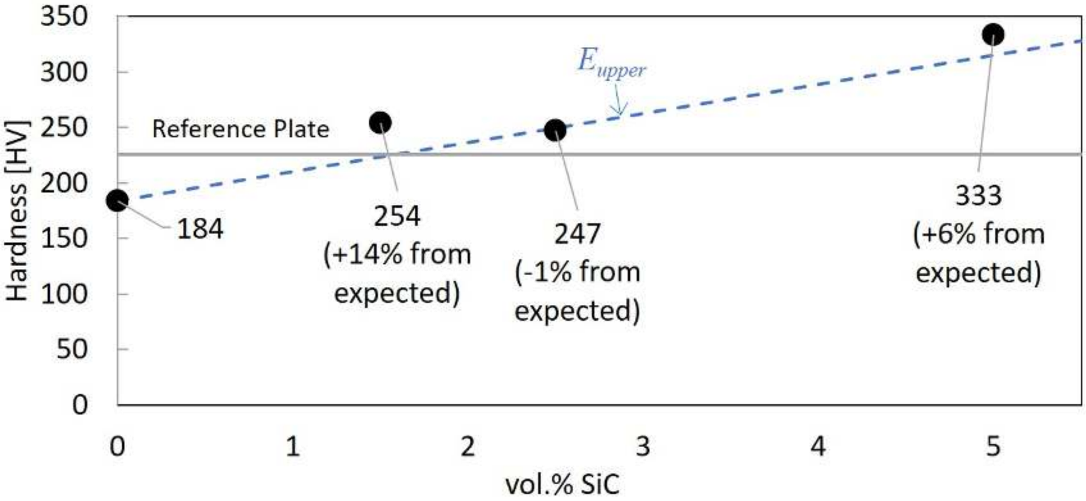

Figure B.9. Vicker's hardness of Inconel 625 with various amounts of SiC additions.

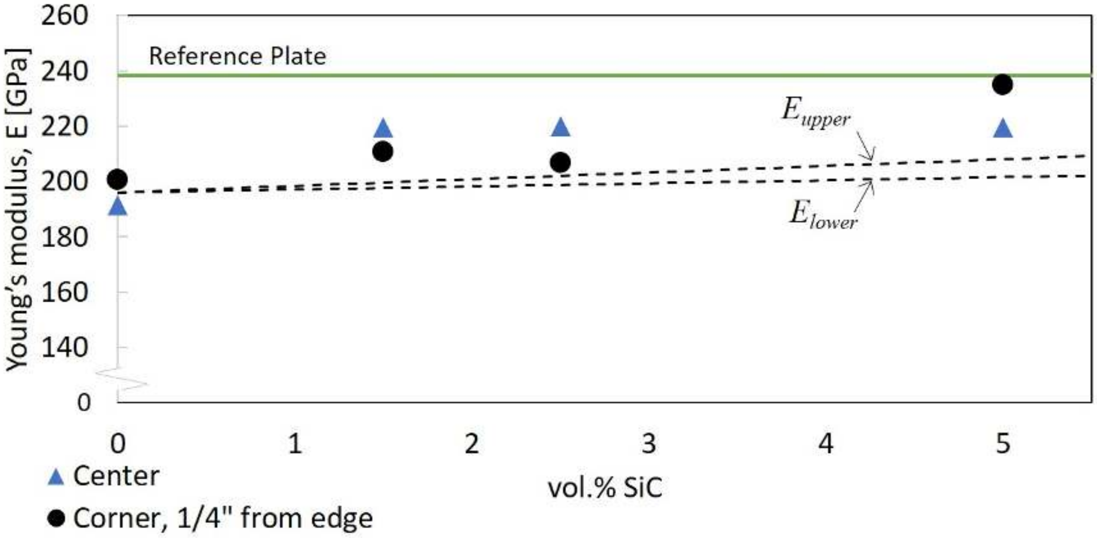

Figure B.10. Elastic modulus of Inconel 625 with various amounts of SiC additions.

Bibliography

[1] Rolls Royce (1996) "Rolls Royce - The Jet Engine.pdf," in *The Jet Engine*, pp. 1–45.

[2] Langmaak, S., S. Wiseall, C. Bru, R. Adkins, J. Scanlan, and A. Sóbester (2013) "An activity-based-parametric hybrid cost model to estimate the unit cost of a novel gas turbine component," *International Journal of Production Economics*, **142**(1), pp. 74–88.

[3] (1992) "CM 247 LC (Directionally Solidified Nickel-Base Turbine Blade Alloy)," *Alloy Digest*.

[4] Reed, R. C. (2006) *The Superalloys Fundamentals and Applications*, `arXiv:1011.1669v3`.

[5] Furrer, D. and H. Fecht (1999) "Ni-based superalloys for turbine discs," *Jom*, **51**(1), pp. 14–17.
URL `http://link.springer.com/10.1007/s11837-999-0005-y`

[6] Cantor, B., H. Assender, and P. Grant (2001) "Aerospace Materials," *Series in Materials Science and Engineering*, p. 556.

[7] Guillon, O., J. Gonzalez-Julian, B. Dargatz, T. Kessel, G. Schierning, J. Räthel, and M. Herrmann (2014) "Field-assisted sintering technology/spark plasma sintering: Mechanisms, materials, and technology developments," *Advanced Engineering Materials*, **16**(7), pp. 830–849.

[8] Seth, B. B., G. P. Wagner, and G. W. Swartzbeck (2002), "Repair and fabrication of combustion turbine components by spark plasma sintering," `arXiv:1208.5721`.

[9] Gu, Y., H. Harada, C. Cui, D. Ping, A. Sato, and J. Fujioka (2006) "New Ni-Co-base disk superalloys with higher strength and creep resistance," *Scripta Materialia*, **55**(9), pp. 815–818.

[10] Pollock, T. M. and S. Tin (2006) "Nickel-Based Superalloys for Advanced Turbine Engines: Chemistry, Microstructure and Properties," *Journal of*

Propulsion and Power, **22**(2), pp. 361–374.
URL `http://arc.aiaa.org/doi/10.2514/1.18239`

[11] Gabb, T. P., R. a. MacKay, S. L. Draper, C. K. Sudbrack, and M. V. Nathal (2013) "The Mechanical Properties of Candidate Superalloys for a Hybrid Turbine Disk," (July), pp. 1–72.

[12] Chang, D., D. Krueger, and R. Sprague (1984) "Superalloy Powder Processing, Properties, and Turbine Disk Applications," *Superalloys 1984 (Fifth International Symposium)*, pp. 245–273.
URL `http://www.tms.org/Superalloys/10.7449/1984/Superalloys{\_}1984{\_}245{\_}273.pdf`

[13] Martin, D. C. (1973) "Using Solid-State Joining in Gas Turbine Engines," (72-GT-74).

[14] Lippold, J. C. (2014) *Welding Metallurgy and Weldability*, `arXiv:1011.1669v3`.

[15] Mathey, G. (1994) *Method of making superalloy turbine disks having graded coarse and fine grains, Tech. rep.*

[16] Gayda, J., T. P. Gabb, and P. T. Kantzos (2004) "The effect of dual microstructure heat treatment on an advanced nickel-base disk alloy," *Superalloys 2004*, pp. 323–329.

[17] Gabb, T. P., P. T. Kantzos, J. Telesman, J. Gayda, C. K. Sudbrack, and B. Palsa (2011) "Fatigue resistance of the grain size transition zone in a dual microstructure superalloy disk," *International Journal of Fatigue*, **33**(3), pp. 414–426.
URL `http://dx.doi.org/10.1016/j.ijfatigue.2010.09.022`

[18] Mourer, D. and J. Williams (2004) "Dual Heat Treat Process Development for Advanced Disk Applications," *Superalloys 2004 (Tenth International Symposium)*, (4), pp. 401–407.
URL `http://www.tms.org/Superalloys/10.7449/2004/Superalloys{\_}2004{\_}401{\_}407.pdf`

[19] Lemsky, J. and J. Gayda (2005) "Assessment of NASA Dual Microstructure Heat Treatment Method Utilizing Ladis SuperCooler(trademark) Cooling Technology," (February).
URL `http://hdl.handle.net/2060/20050161950`

[20] Ning, Y., Z. Yao, H. Guo, and M. W. Fu (2013) "Structural-gradient-materials produced by gradient temperature heat treatment for dual-property turbine disc," *Journal of Alloys and Compounds*, **557**, pp. 27–33.

[21] Taboada Michel, H., L. Sasaki, G. Effgen Santos, J. Cormier, C. Dumont, P. Villechaise, P. Bocher, D. Texier, E. Georges, F. Bridier, F. Hamon, and A. Devaux (2016) "Mechanical Properties of Cast & Wrought Hybrid Disks," *Superalloys 2016*, (September), pp. 539–548.

[22] Gayda, J., T. Gabb, and P. Kantzo (2003) "Heat treatment devices and method of operation thereof to produce dual microstructure superalloy disks," **2**(12).

[23] Walker, B. (1985), "Process for fabricating multi-alloy components," .

[24] Ewing, B. A. and L. C. Lindgren (1982), "Stress resistant hybrid radial turbine wheel," .

[25] Vairis, a. and M. Frost (1998) "High frequency linear friction welding of a titanium alloy," *Mechanical Engineering University of Bristol*, **217**(1), pp. 117–131.
URL `http://linkinghub.elsevier.com/retrieve/pii/S0043164898001458{\%}5Cnhttp://www.scopus.com/inward/record.url?eid=2-s2.0-0032047197{\&}partnerID=tZOtx3y1`

[26] Senkov, O. N., D. W. Mahaffey, and S. L. Semiatin (2014) "Inertia Friction Welding of the Dissimilar Superalloys Mar-M247 and LSHR," *Metallurgical and Materials Transactions A: Physical Metallurgy and Materials Science*.

[27] Tiley, J. S., D. W. Mahaffey, T. Alam, T. Rojhirunsakool, O. Senkov, T. Parthasarthy, and R. Banerjee (2016) "Strengthening mechanisms in an inertia friction welded nickel-base superalloy," *Materials Science and Engineering A*, **662**, pp. 26–35.
URL `http://dx.doi.org/10.1016/j.msea.2016.03.030`

[28] Mahaffey, D. W., O. N. Senkov, R. Shivpuri, and S. L. Semiatin (2016) "Effect of Process Variables on the Inertia Friction Welding of Superalloys LSHR and Mar-M247," *Metallurgical and Materials Transactions A: Physical Metallurgy and Materials Science*, **47**(8), pp. 3981–4000.

[29] Senkov, O. N., D. W. Mahaffey, and S. L. Semiatin (2016) "Effect of Preheating on the Inertia Friction Welding of the Dissimilar Superalloys Mar-M247 and LSHR," *Metallurgical and Materials Transactions A: Physical Metallurgy and Materials Science*, **47**(12), pp. 6121–6137.

[30] Huang, Z. W., H. Y. Li, M. Preuss, M. Karadge, P. Bowen, S. Bray, and G. Baxter (2007) "Inertia friction welding dissimilar nickel-based superalloys alloy 720Li to IN718," *Metallurgical and Materials Transactions A: Physical Metallurgy and Materials Science*, **38 A**(7), pp. 1608–1620.

[31] Chanthapan, S., A. Rape, S. Gephart, A. K. Kulkarni, and J. Singh (2011) "Industrial scale field assisted sintering an emerging disruptive manufacturing technology: Applications," *Advanced Materials and Processes*, **169**(8), pp. 25–28.

[32] Omori, M. (2000) "Sintering, consolidation, reaction and crystal growth by the spark plasma system (SPS)," *Materials Science and Engineering: A*, **287**(2), pp. 183–188.
URL `http://linkinghub.elsevier.com/retrieve/pii/S0921509300007735`

[33] El-Atwani, O., D. V. Quach, M. Efe, P. R. Cantwell, B. Heim, B. Schultz, E. A. Stach, J. R. Groza, and J. P. Allain (2011) "Multimodal grain size distribution and high hardness in fine grained tungsten fabricated by spark plasma sintering," *Materials Science and Engineering A*, **528**(18), pp. 5670–5677.

[34] Tokita, M., E. Bldg, K. Sc, and P. Ksp (2011) "Mechanism of Spark Plasma Sintering," *Ceramics*, **044903**(Mmc), pp. 605–608.
URL `http://linkinghub.elsevier.com/retrieve/pii/S0272884212007146`

[35] Song, X., X. Liu, and J. Zhang (2006) "Neck formation and self-adjusting mechanism of neck growth of conducting powders in spark plasma sintering," *Journal of the American Ceramic Society*, **89**(2), pp. 494–500.

[36] Belmonte, M., J. González-Julián, P. Miranzo, and M. I. Osendi (2010) "Spark plasma sintering: A powerful tool to develop new silicon nitride-based materials," *Journal of the European Ceramic Society*, **30**(14), pp. 2937–2946.
URL `http://dx.doi.org/10.1016/j.jeurceramsoc.2010.01.025`

[37] Chanthapan, S., A. Rape, S. Gephart, A. K. Kulkarni, and J. Singh (2011) "Industrial Scale Field Assisted Sintering: an Emerging Disruptive Manufacturing Technology : Applications," (August).

[38] Pasebani, S., A. K. Dutt, J. Burns, I. Charit, and R. S. Mishra (2015) "Oxide dispersion strengthened nickel based alloys via spark plasma sintering," *Materials Science and Engineering A*, **630**, pp. 155–169.
URL `http://dx.doi.org/10.1016/j.msea.2015.01.066`

[39] Fang, Z. Z., X. Wang, T. Ryu, K. S. Hwang, and H. Y. Sohn (2009) "Synthesis, sintering, and mechanical properties of nanocrystalline cemented tungsten carbide - A review," *International Journal of Refractory Metals and*

Hard Materials, **27**(2), pp. 288–299.
URL `http://dx.doi.org/10.1016/j.ijrmhm.2008.07.011`

[40] Huang, S. G., R. L. Liu, L. Li, O. Van der Biest, and J. Vleugels (2008) "NbC as grain growth inhibitor and carbide in WC-Co hardmetals," *International Journal of Refractory Metals and Hard Materials*, **26**(5), pp. 389–395.

[41] Sun, L., C. Jia, R. Cao, and C. Lin (2008) "Effects of Cr3C2 additions on the densification, grain growth and properties of ultrafine WC-11Co composites by spark plasma sintering," *International Journal of Refractory Metals and Hard Materials*, **26**(4), pp. 357–361.

[42] Sun, L., T. Yang, C. Jia, and J. Xiong (2011) "VC, Cr3C2 doped ultrafine WC-Co cemented carbides prepared by spark plasma sintering," *International Journal of Refractory Metals and Hard Materials*, **29**(2), pp. 147–152.
URL `http://dx.doi.org/10.1016/j.ijrmhm.2010.09.004`

[43] Poetschke, J., V. Richter, and R. Holke (2012) "Influence and effectivity of VC and Cr3C2 grain growth inhibitors on sintering of binderless tungsten carbide," *International Journal of Refractory Metals and Hard Materials*, **31**, pp. 218–223.
URL `http://linkinghub.elsevier.com/retrieve/pii/S0263436811002010`

[44] Wittmann, B., W. D. Schubert, and B. Lux (2002) "WC grain growth and grain growth inhibition in nickel and iron binder hardmetals," *International Journal of Refractory Metals and Hard Materials*, **20**(1), pp. 51–60.

[45] Morton, C., D. Wills, and K. Stjernberg (2005) "The temperature ranges for maximum effectiveness of grain growth inhibitors in WC–Co alloys," *International Journal of Refractory Metals and Hard Materials*, **23**(4), pp. 287 – 293, science of hard materials-8. Part I. Selected papers from the 8th International Conference on the Science of Hard Materials.
URL `http://www.sciencedirect.com/science/article/pii/S0263436805000752`

[46] Amouyal, Y., Z. Mao, and D. N. Seidman (2009) "Phase partitioning and site-preference of hafnium in the γ'(L 1 2)/ γ (fcc) system in Ni-based superalloys: An atom-probe tomographic and first-principles study," *Applied Physics Letters*, **95**(16), p. 161909.

[47] Kotval, P. S., J. D. Venables, and R. W. Calder (1972) "The role of hafnium in modifying the microstructure of cast nickel-base superalloys," *Metallurgical Transactions*, **3**(2), pp. 457–462.

[48] Duhl, D. and C. Sullivan (1971) “Some effects of hafnium additions on the mechanical properties of a columnar-grained nickel-base superalloy,” *JOM*, **23**(7), pp. 38–40.

[49] Harris, K., G. Erickson, and R. Schwer (1984) “MAR M 247 Derivations—CM 247 LC DS Alloy, CMSX® Single Crystal Alloys, Properties and Performance,” in *5th Int. Symp*, pp. 221–230.

[50] E494-05, A. (1995), “Standard practice for measuring ultrasonic velocity in materials,” .

[51] Frage, N., S. Kalabukhov, N. Sverdlov, V. Ezersky, and M. P. Dariel (2010) “Densification of transparent yttrium aluminum garnet (YAG) by SPS processing,” *Journal of the European Ceramic Society*, **30**(16), pp. 3331 – 3337.
URL `http://www.sciencedirect.com/science/article/pii/S0955221910003808`

[52] NAUGHTON-DUSZOVA, A. and E. BĄCZEK (2018) “Selected properties of ZrB2 composites obtained by SPS method for parts of electro-erosion shaping machines,” .

[53] Guo, S., Y. Kagawa, T. Nishimura, and H. Tanaka (2008) “Elastic properties of spark plasma sintered (SPSed) ZrB2–ZrC–SiC composites,” *Ceramics International*, **34**(8), pp. 1811 – 1817.
URL `http://www.sciencedirect.com/science/article/pii/S0272884207001745`

[54] Frage, N., S. Cohen, S. Meir, S. Kalabukhov, and M. P. Dariel (2007) “Spark plasma sintering (SPS) of transparent magnesium-aluminate spinel,” *Journal of Materials Science*, **42**(9), pp. 3273–3275.

[55] Yeheskel, O., R. Chaim, Z. Shen, and M. Nygren (2005) “Elastic moduli of grain boundaries in nanocrystalline MgO ceramics,” *Journal of materials research*, **20**(3), pp. 719–725.

[56] Sundararaman, M., P. Mukhopadhyay, and S. Banerjee (1988) “Precipitation of the δ-Ni3Nb phase in two nickel base superalloys,” *Metallurgical Transactions A*, **19**(3), pp. 453–465.
URL `https://doi.org/10.1007/BF02649259`

[57] Bao, Y. W., W. Wang, and Y. C. Zhou (2004) “Investigation of the relationship between elastic modulus and hardness based on depth-sensing indentation measurements,” *Acta Materialia*, **52**(18), pp. 5397–5404.